

# **Mode-locking, dynamic and nonlinear optical properties of MOVPE-grown InAs/InP quantum-dot and quantum-dash lasers**

vorgelegt von  
M. Sc. Tagir Sadeev  
geb. in Kasan

von der Fakultät II - Mathematik und Naturwissenschaften  
der Technischen Universität Berlin  
zur Erlangung des akademischen Grades  
Doktor der Ingenieurwissenschaften  
Dr.-Ing.

genehmigte Dissertation

Promotionsausschuss:

Vorsitzender: Prof. Dr. Andreas Knorr

Gutachter: Prof. Dr. Dieter Bimberg

Gutachter: Prof. Dr. Abderrahim Ramdane

Tag der wissenschaftlichen Aussprache: 24 November 2016

Berlin 2016



## List of publications

### Reviewed papers:

1. T. Sadeev, D. Arsenijević, D. Franke, J. Kreissl, H. Künzel, and D. Bimberg, “1.55- $\mu\text{m}$  mode-locked quantum-dot lasers with 300 MHz frequency tuning range,” *Appl. Phys. Lett.*, vol. 106(3), 031114 (2015).
2. T. Sadeev, H. Huang, K. Schires, F. Grillot, and D. Bimberg, “Highly efficient non-degenerate four-wave mixing under dual-mode injection in InP / InAs quantum-dash and quantum-dot lasers at 1.55  $\mu\text{m}$ ,” *Appl. Phys. Lett.* 107(19), 191111 (2015).
3. T. Sadeev, D. Arsenijević and D. Bimberg, “Comparison of dynamic properties of InP/InAs quantum-dot and quantum-dash lasers,” *Appl. Phys. Lett.* 109(16), 161104 (2016).
4. H. Huang, D. Arsenijević, K. Schires, T. Sadeev, D. Erasme, D. Bimberg, and F. Grillot, “Efficiency of four-wave mixing in injection-locked InAs/GaAs quantum-dot lasers,” *AIP Adv.*, vol. 6, no. 12, p. 125105, Dec. 2016.

### Conference contributions:

5. E. Rouvalis, D. Arsenijević, M. Spiegelberg, T. Sadeev, R. Ziegler, A. G. Steffan, and D. Bimberg, „40 GHz Quantum Quantum-Dot Mode-Locked Laser Packaged Module operating at 1310 nm,“ Asian Commun. Photonics Conf. 2014, pp. 40–42, 2014.
6. T. Sadeev, H. Huang, K. Schires, F. Grillot, and D. Bimberg, “Non-linear and dynamic properties of MOVPE- grown InAs / InP quantum-dot and quantum-dash Fabry-Perot lasers,” 2015 IEEE Photonics Conf., vol. 4, pp. 607–608, 2015.
7. H. Huang, K. Schires, R. Raghunathan, D. Erasme, D. Arsenijević, T. Sadeev, and D. Bimberg, “Highly Efficient Wavelength Conversion in InAs / GaAs Quantum Dot Lasers,” 2015 IEEE Photonics Conf., vol. 2, pp. 543–544, 2015.
8. F. Grillot, H. Huang, K. Schires, T. Sadeev, D. Arsenijević, and Dieter Bimberg, „Optical Nonlinearities in Injection-Locked Nanostructure Light-based Emitters,“ Photonics Europe, April 3-7, Brussels, Belgium, 2016
9. H. Huang, K. Schires, T. Sadeev, D. Arsenijević, Dieter Bimberg, and F. Grillot, „InAs/GaAs excited state quantum-dot transmitters operating under long-delayed optical feedback,“ Photonics Europe, April 3-7, Brussels, Belgium, 2016.
10. T. Sadeev, D. Arsenijević, and D. Bimberg, “1.55- $\mu\text{m}$  directly modulated InAs/InP quantum-dot and quantum-dash lasers,” 2016 IEEE Photonics Conf. Accepted.



# Contents

1. Introduction.....	1
2. Epitaxial growth and device fabrication .....	7
3. QDot and QDash laser based optical pulse emitters .....	10
3.1 Two-section passively mode-locked lasers.....	10
3.1.1 QDot passively mode-locked lasers .....	11
3.1.2 QDash passively mode-locked lasers.....	20
3.1.3 Measurement of optical pulses.....	25
3.1.4 Hybrid mode-locking .....	28
3.1.5 Discussion .....	30
3.2 Mode-locking in single-section devices.....	31
3.2.1 QDot single-section mode-locked lasers.....	31
3.2.2 QDash single-section mode-locked lasers.....	34
3.2.3 Discussion .....	37
3.3 Frequency resolved optical gating techniques based investigations of InP/InAs nanostructure mode-locked lasers.....	38
3.4 Gain switching of InP/InAs nanostructure based laser .....	40
3.5 Conclusion .....	42
4. Four-wave mixing in quantum-dot/quantum dash Fabry-Perot lasers.....	44
4.1 Introduction.....	44
4.2 Four-wave mixing in semiconductor lasers and optical amplifiers: theoretical background.....	44
4.3 Optical injection-locking.....	48
4.4 Experimental set-up .....	49
4.5 Experimental investigation .....	50
4.5.1 InP/InAs quantum-dot and quantum dash lasers.....	50
4.5.2 Discussion .....	53
4.5.3 InAs/GaAs quantum-dot lasers .....	56
4.6 Conclusion .....	57
5. Directly modulated InP/InAs nanostructure lasers for data transmission.....	59
5.1 Small-signal modulation .....	60
5.1.1 Quantum-dot lasers small-signal analysis.....	64
5.1.2 Quantum-dash lasers small-signal analysis.....	67
5.1.3 Discussion. ....	70
5.2 Large-signal digital modulation .....	71
5.3 Conclusion .....	74

6. Summary ..... 76  
List of Acronyms ..... 78  
Bibliography..... 81  
Acknowledgement ..... 95

## 1. Introduction

Over several decades the network traffic has been growing exponentially and according to the Cisco report the Global Internet traffic increased fivefold from 2010 to 2015. White paper issued in June claims that, in 2016 IP traffic will grow at a compound annual growth rate of 22% from 2015-2020 and by 2020 global fixed broadband speeds will reach 47.4 Mb/s, up from 24.7 Mb/s in 2015. Such growth rate, driven by the Internet of Things, streaming high-definition video and virtual reality sessions will require cost-effective solutions for high-speed broadband data transmission systems. Those solutions are based on fiber optic networks offering high capacity, scalability and large bandwidth. In the Figure 1-1 the increase of fiber optic network capacity over years is shown, where each leap is preceded by the invention of new technology. Yet, the world has never had enough bandwidth, keeping strong the interest of developers and researches in the key components of an optical network – the semiconductor laser.

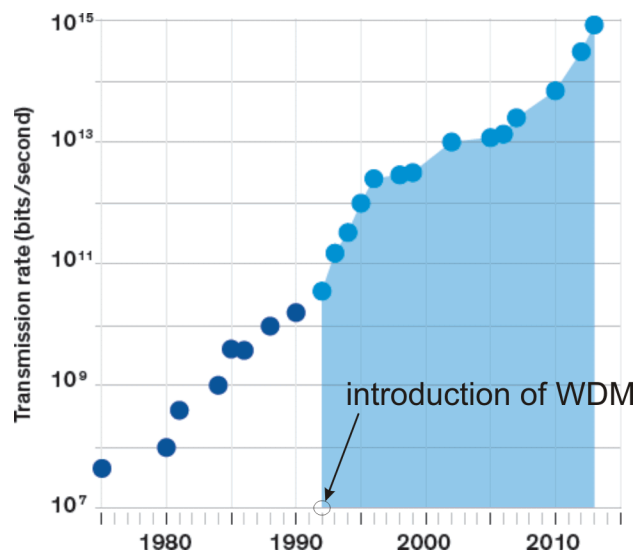


Figure 1-1 Fiber optic capacity (reproduced from [1])

The whole set of semiconductor lasers in fiber based optical communications can be divided in two large groups: lasers for long and short haul transport. The first group lasers are subject to single- and multi-level amplitude and phase modulation formats requiring coherent detection schemes. High spectral efficiency and wavelength tunability are the absolute „must-have“ for such devices in the nearest future. In 2013 800 Gb/s channel along 400-km was installed (between London and Ipswich), in 2014 1 Tb/s transmission was demonstrated. The future systems will employ 12 Tb/s channels bringing the optical fiber capacity to the Shannon limit [1]. The second group devices are usually employed in local area networks (LAN), access

networks, data centers. Here low-cost intensity modulation and direct detection schemes are used and the energy efficiency of the laser is certainly the advantage, although more expensive and sophisticated solutions based on quadrature amplitude modulation are also an option. One of the universal approaches to increase the bandwidth is to employ a wavelength-division multiplexing (WDM). WDM allows a simultaneous transmission on independent wavelengths (optical carriers) either in the same or in different transparency windows of a standard optical fiber. WDM technology is widely used nowadays on every level of the network interaction (residential networks, access networks, metropolitan area networks). The drawbacks of WDM are low spectral efficiency, high cost of components (especially in so-called all-optical interconnections) and complicated network routing/wavelength assignment due to increased number of carriers. In optical time-division multiplexing (OTDM) different optical pulse trains, emitted by the same laser, are separately modulated by electrical data signal. Then, these modulated pulse streams are multiplexed in the single high bit-rate pulse stream.

OTDM stream can be modulated by on-off keying, differential-phase-shift (DPSK) and quadrature keying (DQPSK) as well as m-ary PSK and m-ary quadrature-amplitude modulation. However, practically hybrid of OTDM and WDM technologies are implemented, e.g. in GPON (Gigabit Passive Optical Network), where different wavelengths are used for up- (1310 nm) and downstream (1490 nm) and for TV-signal transmission (1550 nm). The downstream is a broadcast signal and upstream is OTDM-signal, as all end-user devices use the same wavelength at certain time interval, set by TDM-protocol. Nevertheless, for all mentioned concepts (WDM, OTDM, hybrid WDM+OTDM) of state-of-the-art optical networks and future optical networks the availability of low-cost laser sources becomes extremely crucial.

Certainly, the complex task of increasing the absolute bandwidth is very diversified and may have several solutions. For example, in WDM network architecture, the bandwidth of each directly modulated laser can be pushed further, this would need the development of a laser with extremely low chirp, noise and high-speed turn-on/off dynamics. Secondly, the laser array employed in WDM may in future be replaced by a single laser source, which emits a spectral comb. Nowadays the most cost-effective and promising candidate for a source of the spectral comb is a semiconductor mode-locked laser (MLL). Another way to increase the bandwidth of optical network is the further development of external modulators, which includes the reduction of chirp, size, and power consumption. Some of these issues can be solved by the PIC (photonic integrated circuit) concept. This approach consists in the integration of several active and passive

photonic devices into single chip. PIC concept is very promising in terms of optical losses reduction, energy consumption, miniaturization and the state-of-the-art characteristics of end-product [2]–[4]. Recently 112 GB/s transmission with double side electroabsorption modulated distributed feedback laser was presented [5]. Yet, the challenges related to crosstalk between integrated devices and the fabrication complexity should be solved. On the other hand, the bit-rate of a component with limited bandwidth can still be increased without employing sophisticated PIC-technology. The concept of high-order modulation helps to reduce the number of wavelengths and optical fiber in comparison with simplest non-return-to-zero (NRZ) format thus increasing the capacity of the whole optical inter connect. The use of high-order modulation simplifies the requirements for the laser but increases the complexity of the electronic components. Thus, we will need a solution, which provides the right balance between performance, cost and power. We therefore believe that directly modulated and mode-locked lasers are good compromise due to low costs, low power consumption and high output power, however the chirp can be the limiting factor for high-speed operation. Significant improvements of laser performance, like lower chirp and threshold current density or larger  $T_0$ , have been achieved in the last decades, thanks to implementing zero-dimensional structures – quantum dots (QDots) in active GaAs- and InP-based layers [6]–[8]. This generation of semiconductor devices has evolved nearly three decades ago following even former theoretical research on the active medium with 0-dimensional nanostructures called quantum dots [9]. Quantum dot is a nanometer-scale structure with the size equal or smaller than de Broglie wavelength and may consist of the large number of semiconductor atoms. This results in three dimensional quantum confinement and therefore density of states function becomes delta-like in contrast to the step-like function of quantum-well material or parabolic for bulk-type material (see Figure 1-2). Present QDot GaAs-based devices benefit from the large local carrier confinement and record material gain [10]–[12] resulting from the delta-function like density of states (DOS). Such devices demonstrate temperature insensitive low threshold current density and reduced chirp making them very attractive for optical communication [13], [14]. Most of the initial breakthroughs were demonstrated for GaAs-based devices, finding applications in the O-band for local area networks. Work on InP-based nanodevices started much later and is much less detailed, although presently in long distance and medium range communication systems InP-lasers are deployed. Many InP material science groups initially did not obtain true QDot gain regions like in GaAs, but so-called quantum-dashes (QDashes), a kind of broken QWires [15], [16], showing a completely different density of states function shown in Figure 1-2 (c). It is not really clear until now, how the laser properties, in particular the dynamic and nonlinear ones,

between dash-based and dot-based differ. A number of theoretical publications compared the modulation dynamics of QDot and QDash lasers [17]–[19] and found differences, so far no experimental results however have been presented in order to support these investigations. Most of the results published on QDash lasers are based on MBE (Molecular Beam Epitaxy) growth [20]–[22], whereas most of the much fewer QDot laser results [23]–[25] are based on MOVPE growth, featuring excellent surface/interface morphology and thickness control, possibility for patterned growth, and multiple wafer scale-up. Today’s state-of-the-art MOVPE-grown InP-based InAs QDot lasers are capable of error-free 27.5 Gb/s transmission as published in [26], whereas the newest MBE-grown lasers seem also capable of  $\sim 25$  Gb/s data rates with the potential up to 34 Gb/s yet no bit-error rate measurements for these devices are available at this time [27].

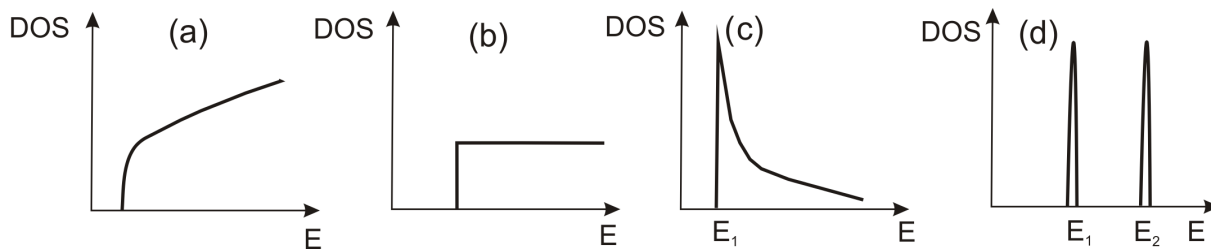


**Figure 1-2** Density of states function for (a) bulk, quantum well (b), quantum wire (c) and quantum dot (d)

This thesis investigates the optical properties of C-communication band (1550 nm) MOVPE-grown QDash and QDot active material based lasers, which are identical as heterostructures and as processed devices, except some details, which were varied during the growth of the active area, leading either to dots or to dashes. Particularly, we focus on mode-locking phenomena in single- and two-section QDash/QDot devices. We study the optical pulse emission characteristics under the passive and hybrid mode-locking. In the temporal domain autocorrelation and frequency-resolved optical gating measurements gave us insight into the pulse formation dynamics, whereas the optical domain reveals the generation of optical frequency comb. In collaboration with Télécom ParisTech, we demonstrate how the type of material system affects the intracavity non-degenerate four-wave mixing process under external injection. It is also the purpose of this thesis to compare dynamic properties (under small and large signal modulation) of QDash and QDot lasers. An approach to develop fast and energy efficient lasers sources for C-band optical communication can be based on our results achieved here.

The thesis is organized as follows. In Chapter 2, we will briefly describe the growth and fabrication process of the QDot and QDash lasers investigated in this thesis.

In Chapter 3, we will experimentally investigate QDot and QDash lasers as optical ps and sub-ps range pulse emitters. We will focus on passive mode-locking phenomena in QDot and QDash laser and its main characteristics: optical power and spectrum; pulse width and repetition frequency. Basic characteristics of passively mode-locked QDot and QDash lasers (PMLL) are described in the subchapters 3.1.1 and 3.1.2 respectively. The measurement of optical pulse width for QDot and QDash PMLL is presented in 3.1.3. Hybrid mode-locking regime will be experimentally investigated in section 3.1.4. Single-section mode-locked lasers constitute specific class of mode-locked lasers as optical pulse emitter and are yet to be described theoretically. We investigate the mode locking properties of single-section QDash and QDot lasers in section in 3.2. Subsequently, in section 3.3 we present the results of pulse shape measurements using frequency-resolved optical gating techniques. Then, in section 3.4 gain switched QDot laser optical pulse emission is demonstrated.

Chapter 4 will investigate external optical injection induced non-degenerate four-wave mixing (NDFWM) phenomenon in QDot and QDash lasers. Firstly, brief theoretical background of four-wave mixing and injection locking are introduced in section 4.2. In sections 4.3 and 4.4, we then describe the optical injection-locking mechanism and the experimental set-up. In section 4.5, NDFWM in 1.55- $\mu\text{m}$  QDot and QDash InP/InAs lasers will be investigated and compared. Further, we will discuss the factors affecting the efficiency of NDFWM and normalized  $\chi^{(3)}$  parameter in these lasers and determine the main aspects playing role in a large qualitative and quantitative difference of the NDFWM in InP/InAs QDot and QDash lasers. Then, we will also investigate NDFWM in 1.3- $\mu\text{m}$  QDot GaAs/InAs lasers. Subsequently, we will compare NDFWM characteristics of those devices. In the last section 4.6, a conclusion of the results will be given.

Chapter 5 present the experimental investigation of the dynamics of QDot and QDash lasers under small- and large-signal modulation. In section 5.1 we will at first present theoretical background on small-signal operation of semiconductor laser based on rate equations. In sections 5.1.1-5.1.2 we will present experimental results of short cavity QDot and QDash lasers small-signal measurements and will look at their characteristics. Subsequently, we will describe and explain the features of their small-signal operation. In section 5.2, we will investigate the large-signal modulation capabilities of QDot and QDash lasers. In the discussion section 5.3 we

will give a consistent comparison of quantum-dot and quantum-dash lasers dynamics based on  $D$ - and  $K$ -factor, relaxation resonance frequency and -3 dB bandwidth and give a conclusion of the results demonstrated in this chapter.

The summary of the results of this thesis and outlook will be presented in Chapter 6.

## 2. Epitaxial growth and device fabrication

In this chapter, we will introduce the quantum-dot and quantum-dash growth technology and main processing steps used for the fabrication of the samples used in the scope of this thesis. Briefly, the effect of the growth conditions on the shape of the nanostructures and their properties such as density and size will be presented. Most of the work presented in this chapter was conducted in Heinrich-Hertz Institute (Berlin).

The growth of self-organized quantum-dot (QDots) and quantum dashes (QDashes) on InP(100) substrate for 1.55- $\mu\text{m}$  applications has been successfully demonstrated using molecular- and chemical beam epitaxy (MBE, CBE) [28]–[30], metal-organic vapor phase epitaxy (MOVPE) [31], [32]. The self-formation of nanostructures (also referred as or Stranski-Krastanov (SK) growth mode) utilizes the mechanism of 3-D islands nucleation as critical thickness of deposited film produces strain due to the lattices mismatch between the substrate and deposited material. In the scope of this thesis, we investigate MOVPE-grown laser devices, whose epitaxial layer structure is shown in Figure 2-1. The structure comprises a 50 nm thick lower optical waveguide layer composed of quaternary  $\text{In}_{0.82}\text{Ga}_{0.18}\text{As}_{0.40}\text{P}_{0.60}$  (Q1.15) material, deposited onto 800 nm of n-InP layer. Between the waveguide layers an  $\text{In}_{0.78}\text{Ga}_{0.22}\text{As}_{0.47}\text{P}_{0.53}$  (Q1.20) matrix with incorporated InAs QDots/Dashes layers is placed. The 40 nm of spacer separates InAs layers, the thickness of the deposition is modified to compensate the predicted blue-shift of the emission due to consequential re-growth of the blocking and contact layers. 300 nm of upper p-doped cladding layer and electrical contact layer completes the structure.

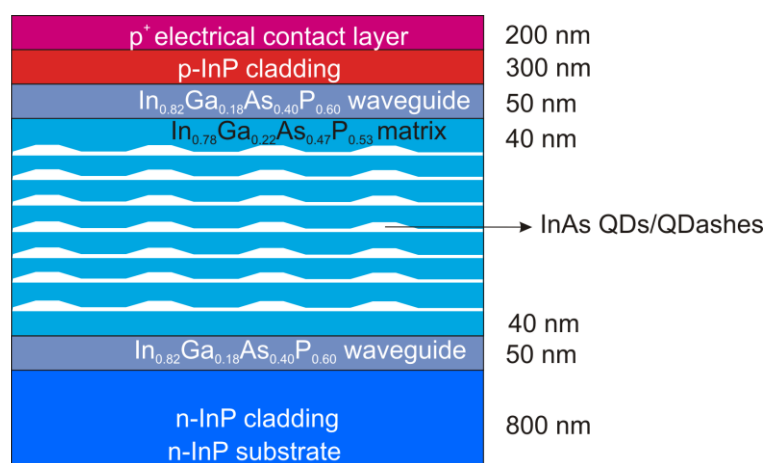


Figure 2-1 Epitaxial structure.

As further details on the material growth can be found in [24], [33] but we want to point that unlike any other well-known growth techniques as MBE or CBE, MOVPE used in the scope of this thesis, allows for formation of both QDots and QDashes depending basically on the temperature of the growing, indium flux rate and deposition time. Secondly, the highest temperature of the growing is limited by QDots clusterisation phenomena, whereas the lowest temperature is given by incomplete deposition [24]. The growth temperature was kept in 460-530°C range. Upon reduction of the growing temperature below 500°C the dot size decreases and the density increases, moreover, the inhomogeneous broadening also decreases. Indium flux rate and deposition time determine the amount of deposited InAs. Subsequently, nanostructure size and density is affected, e.g. doubling indium flux, at constant InAs thickness, leads to the factor of 1.5 increase of the nanostructures density. However, the increase of the growth rate or the decrease of the temperature lead to the formation of QDashes. Finally, the devices investigated in this thesis are QDot and QDash lasers, both grown at 530°C and 10 sccm and 100 sccm of the In-flux rate respectively. The density of the dots or dashes is  $\sim 2 \times 10^{10}/\text{cm}^2$  and  $\sim 5 \times 10^{10}/\text{cm}^2$  respectively, measured by AFM [33]. The QDot diameter equals to  $\sim 30$  nm and the height is about 9 nm. QDashes are  $\sim 60$  nm long, the width is  $\sim 15$  nm and the height is  $\sim 2$  nm. After the epitaxial growth, deep etching through the active region is performed in order to obtain narrow ridge structure ( $\sim 1-2 \mu\text{m}$ ) for single-mode emission in lateral direction. Afterwards, n- and p-InP blocking layers are regrown using mask assisted selective growing. Then, p-InP and p-InGaAs layers are grown, and TiPtAu contact compound completes the whole device structure shown in Figure 2-2.

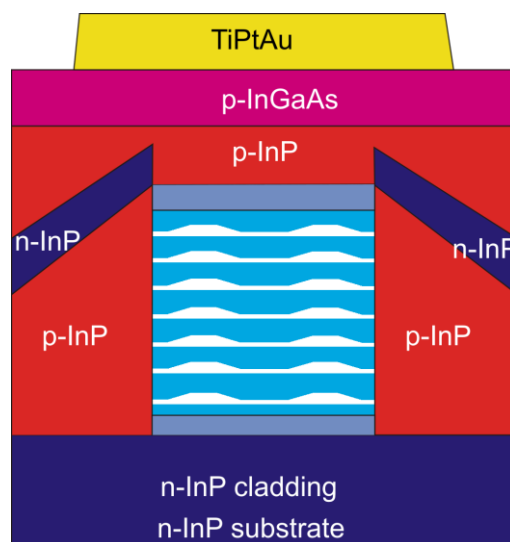


Figure 2-2 Out of scale sketch of buried heterostructure QDot/Dash laser (reproduced from [34]).

Figure 2-3 is a top view of the laser bar consisting of three devices. The yellow-colored area denotes the metallization of p- and n-contact pads as well as the narrow ridge. Finally, the laser bars are mounted after cleavage on the copper blocks by means of two-component epoxy compound for better thermo-electrical conductivity. All the measurements in this thesis are conducted with the copper block clamped on the copper-chuck. The copper-chuck is kept at a constant temperature of 20 °C by means of a Peltier cooler and the temperature controller.

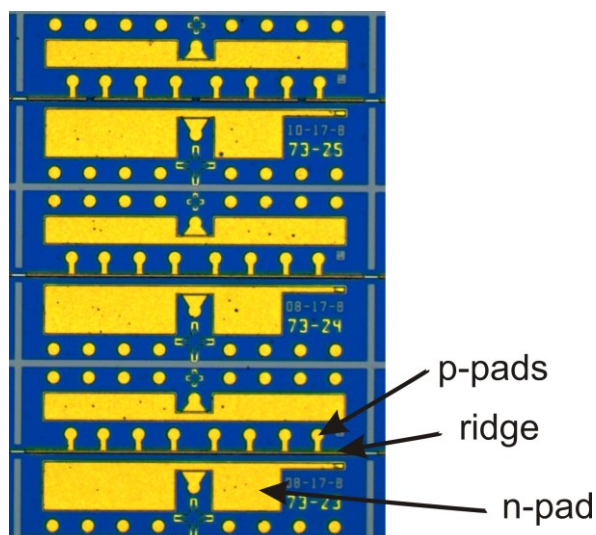


Figure 2-3 Laser bar with three laser devices.

### 3. QDot and QDash laser based optical pulse emitters

This chapter is dedicated to the experimental investigation of QDot and QDash lasers as optical ps and sub-ps range pulse emitters. Mode-locking (ML), gain switching (GS) and Q-switching (QS) are the mechanisms used to make the semiconductor device to operate in pulsed regime. In this chapter, we will focus on passive mode-locking phenomenon in QDot and QDash laser and its main characteristics: optical power, pulse width and repetition frequency. Basic characteristics of passively mode-locked QDot and QDash lasers (PMLL) are described in the subchapters 3.1.1 and 3.1.2 respectively. The measurement of optical pulse width for QDot and QDash PMLL is presented in 3.1.3. Single-section mode-locked lasers constitute specific class of mode-locked lasers as optical pulse emitter and are yet to be described theoretically. We investigate the mode-locking properties of single-section QDash and QDot lasers in section in 3.2. Subsequently, in section 3.3 we present the results of pulse shape measurements using frequency-resolved optical gating techniques. Then, in section 3.4 gain switched QDot laser optical pulse emission is demonstrated.

#### 3.1 Two-section passively mode-locked lasers

Passive mode-locked lasers (PMLL) are semiconductor devices, which emit ps and sub-ps optical pulses with the repetition rate up to several hundreds of GHz without any external microwave frequency generator. Thus, PMLL seems to be a cost effective solution for high rate ps and sub-ps optical pulse generator finding its applications in optical time-division multiplexing systems (OTDM), optical sampling and clock recovery. In optical domain, PMLL can serve as the optical pulse comb source with applications in wavelength-division multiplexing (WDM) and radio-over-fiber systems as well as arbitrary optical/microwave waveform generation.

PMLL consist of electrically isolated gain section (forward DC (direct current)-biased) and absorber section (reverse DC-biased) which are operated independently, but share the same optical medium. We also will call PMLL two-section laser later on.

### 3.1.1 QDot passively mode-locked lasers

Average optical power. An integrating sphere is used to measure average optical power of PMML as a function of gain section current and absorber section (also referred as reverse) voltage. The first measured PMML is QDot laser; its LIV-curves are shown in Figure 3-1, all being measured at room temperature and CW-regime. The total cavity length is 1.25 mm, and the absorber-to-gain section ratio is 1:5.6. LIV of the single-section device, which is a standard Fabry-Perot laser, driven only by an electrical pumping of the gain section, shown in the figure for reference. Single- and two-section devices are located on the same laser bar.

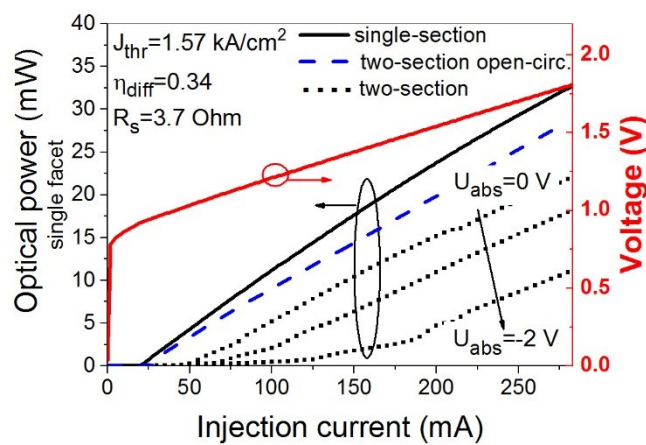
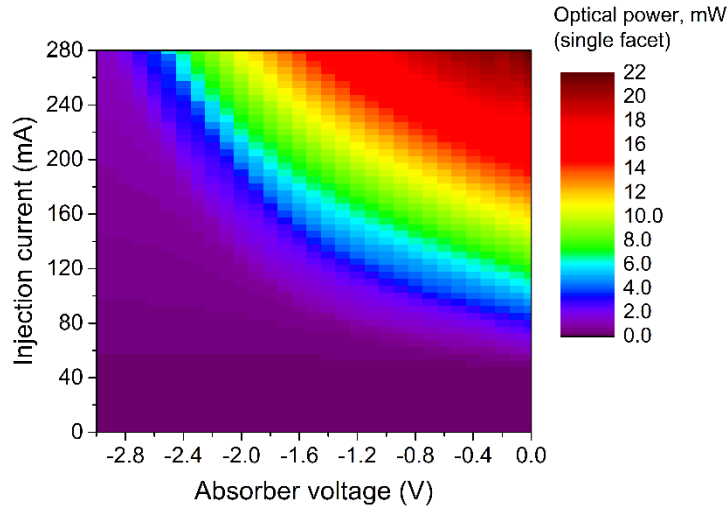


Figure 3-1 Light-current characteristics of QDot single-section and two-section devices

The threshold current density is  $1.52 \text{ kA/cm}^2$ , the differential quantum efficiency is 0.32, maximum output power is 34 mW, the series resistance is 3.7 Ohm and turn-on voltage is equal to 0.78 V for single-section devices. For two-section lasers an increased threshold current is observed for absorber section (AS) open-circuit and increasing reverse bias due to the increasing absorption, but it is obvious that longer gain section can still compensate absorber induced losses. More common way to exhibit two parameters dependent optical power with the reasonable resolution (0.1 V and 5 mA res.) is color-coded map (Figure 3-2). Maximum applied gain section current does not exceed 280 mA due to the saturation of the output optical power. Secondly, the photocurrent in short absorber section ( $\sim 190 \text{ }\mu\text{m}$ ) should be taken into account, because the latter is acting as the photodiode and experiences extremely large ( $\sim 1\text{-}3 \text{ kA/cm}^2$ ) photocurrent densities. The increase of the absorber reverse voltage consequently increases the number of trapped photons and the photocurrent increases as well. Therefore, on one hand the facet damage can occur due to the large gain section current and on the other hand, the absorber section burnout is possible due to the large photocurrent. Well-known optical power bistability

(or hysteresis) effect, manifesting itself when the direction of gain section current is changed [35], is not observed here. Maximum optical power is around 22 mW measured from GS facet.



**Figure 3-2 Two-section QDot laser optical power**

Repetition frequency. The pulse train repetition frequency (or mode-locking frequency (ML-frequency)) is given by a laser cavity length:

$$F = \frac{c}{2nL_{cavity}}, \quad (3.1)$$

where  $n$  is the refractive index and  $L_{cavity}$  is the length of the device cavity. The highest repetition frequency reported for MOVPE-grown two-section QDot material based lasers is 10 GHz, which corresponds to 4 mm cavity length [36]. Higher repetition rates up to 100-300 GHz are reported, but refer either to QDash based active material or to so-called single-section mode-locked lasers [37]–[39]. The repetition frequency can be further increased by shortening the cavity length, but this approach is firstly limited by increased threshold gain of short lasers, and secondly, results in blue shift of the emission spectra, which demands additional consideration and modelling during device design. Some additional measures in device design may be considered, allowing the increase of repetition frequency, e.g. incorporation of one or multiple absorber sections in so-called colliding pulse layout, where the cavity gets divided into several short gain-absorber sections thus achieving the multiplication of fundamental repetition frequency [40]. Affecting the refractive index would be another option for repetition frequency tuning, as it depends on the temperature and bias parameters of a device.

The usual way to measure the pulse train repetition frequency is to record the output signal of photodiode with an electrical spectrum analyzer (ESA), the optical input of the photodiode is in turn the laser's output signal. The repetition frequency can be also measured roughly with autocorrelation techniques, in this case pulse train instabilities (and thus significant measurement error) and long measurement time are the limiting factors.

QDot MLL repetition frequency is extracted from ESA trace and shown in Figure 3-3. Mode-locking frequency exhibits linear decrease with increased gain section current. The curve slopes are found to be absorber voltage dependent: larger the voltage, steeper the slope.

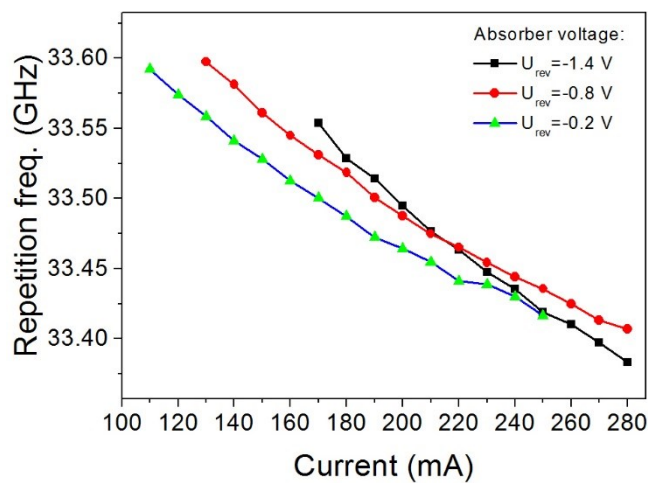


**Figure 3-3 QDot MLL repetition frequency vs. gain section current**

With increased current the device experiences cavity length expansion, leading to almost linear decrease of the repetition frequency. The decrease of the repetition frequency with reverse voltage at constant gain section current of 280 mA is shown in the Figure 3-4. This decrease is associated with the refractive index dispersion [41], the dispersion increases with a blue shift of the optical spectrum (Figure 3-4 (inset)) caused by increased reversed voltage.

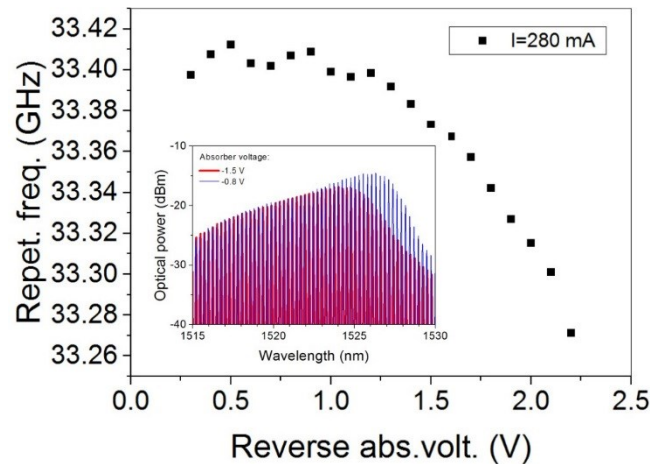


**Figure 3-4 QDot MLL repetition frequency vs reverse voltage (inset: blue shift of the optical spectrum)**

The radiofrequency (RF) spectra for each pair of  $U_{\text{abs}}/I_{\text{inj}}$  from -2.2 V to 0 V and from 90 mA to 280 mA, is recorded, resulting in a RF vs.  $U_{\text{abs}}/I_{\text{inj}}$  map (shown in Figure 3-5), considering only pure single RF-line generation, which is obligatory for stable mode-locking operation, i.e. RF signal-to-noise ratio (SNR) is larger than 30 dB in the whole range. In RF-domain, the region of mode-locking (ML) is limited by: a) Q-switching (Figure 3-6), characterized by the presence of low-frequency oscillations and their beating products as a result of the cavity loss modulation. The mismatch between the reverse bias dependent absorption spectrum (provided by absorber section) and the lasing spectra (provided by gain section) is found to be detrimental for ML regime; Q-switched ML regime neighbours with no-lasing condition at higher reverse voltages and lower gain section currents (laser is below threshold); b) CW (continuous wave)-lasing is the result of the absorber saturation due to high gain section current and large carrier relaxation time. The absorption becomes very weak or vanishes at low  $U_{\text{abs}}$  (0 V to -0.2 V) and high current ( $I_{\text{inj}} > 190$  mA). CW lasing neighbours an unstable regime, i.e. the regime when undesired RF-lines co-exist with fundamental ML-frequency in sub-GHz frequency range. From Figure 3-5 one can deduce that 300 MHz is the tuning range of repetition frequency under pure ML conditions in tested QDot MLLs.

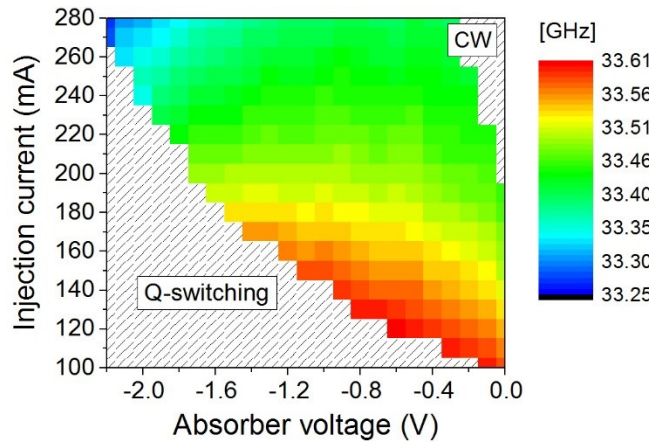


Figure 3-5 QDot MLL ML-frequency map

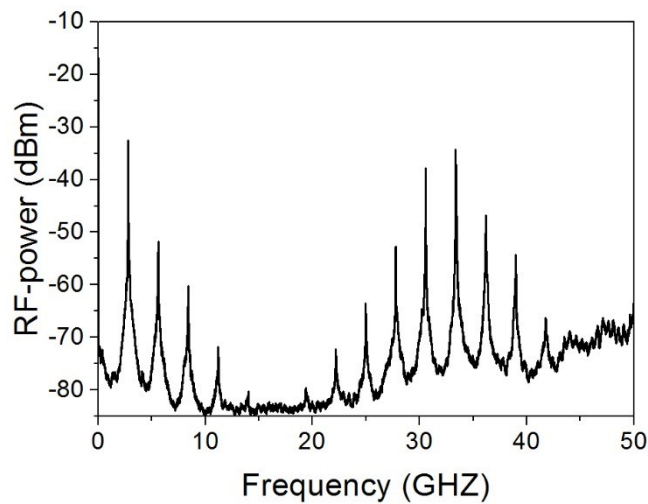


Figure 3-6 QDot-MLL Q-switched ML-regime

The same scanning procedure is applied to obtain the RF-peak power map (Figure 3-7). The power of the fundamental ML-frequency is  $> -32$  dBm almost in the whole region of mode-locking. At the border with Q-switched ML regime, it accordingly decreases as parasitic RF-lines and noise level rise up.

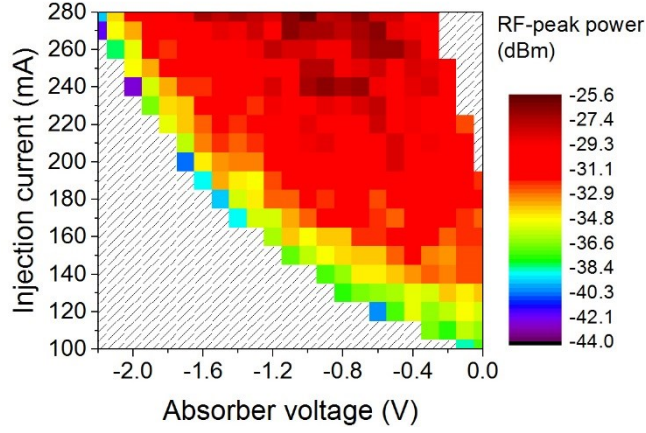
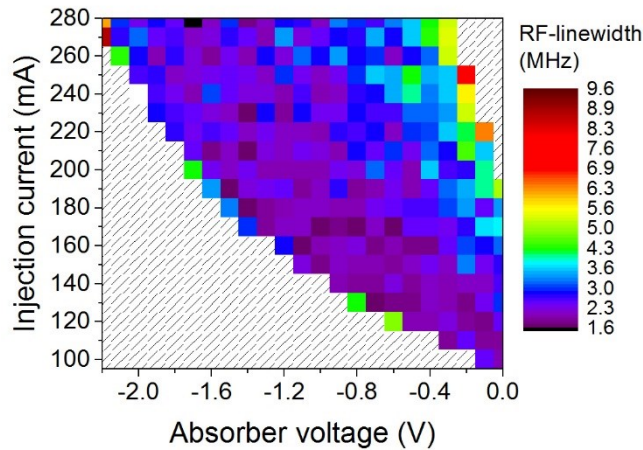


Figure 3-7 QDot MLL RF-peak power scan

RF linewidth can also be extracted from ESA traces when measured with sufficient spectral resolution. RF linewidth serves as a noise parameter of the optical pulse train and related to MLL intensity phase noise. Narrower RF linewidth corresponds to lower intensity phase noise, which means lower phase noise of an optical mode. In the absence of intensity phase noise RF line shape is represented by Dirac function, otherwise it undergoes Lorentzian broadening [42]. According to the method described in [43] FWHM  $\Delta f_{RF}$  of an RF line fitted with Lorentzian function provides the direct measurement of pulse-to-pulse rms jitter, which is important parameter for optical communication systems and optical signal processing:

$$\sigma_t^{pp} = T_r \sqrt{\frac{\Delta f_{RF} N T_r}{2\pi}}, \quad (3.2)$$

where  $T_r$  is the period of the pulse train,  $\Delta f_{RF}$  the full-width at half-maximum of the Lorentzian,  $N$  the number of periods between two compared pulses. Several techniques can be exploited to reduce the RF linewidth, e.g. external optical feedback, optical self-seeding and hybrid mode-locking based solutions [44]–[46]. Figure 3-8 shows RF linewidth of the QDot MLL as a function of bias parameters. The mapping shows that RF linewidth is 2-3 MHz in the whole region of mode-locking; the minimum RF linewidth was about 1 MHz. This is approx. one order of magnitude higher in comparison to bulk or quantum-well MLL [47]–[49]. Such a discrepancy can be attributed to higher background spontaneous emission and higher losses within the cavity. Higher spontaneous emission may have its origin in incomplete population inversion within the QDot gain material [50].



**Figure 3-8 QDot MLL RF linewidth scan**

Optical spectrum. The peak emission of QDot MLL is around 1525 nm at room temperature. The spectrum for three operating points (gain section current fixed, reverse voltage varied) are shown in Figure 3-9. Plots show power degradation at increased reverse voltages (due to enhanced absorption) and the blue shift, which is found to be linear vs applied reverse voltage with the rate of 3.3 nm/V (see the inset). Experimental investigations made on GaAs/InAs QDot MLL show that the reason for this shift is the voltage dependent absorption spectra [51] and increased threshold gain which is obtained from higher energy level transitions. Absorption efficiency undergoes red shift, consequently blue part of the lasing spectra experiences lower induced losses. The spectral FWHM increases with increasing reverse voltage and reaches a maximum value of  $\sim 8$  nm at  $I_{inj}=200$  mA and  $U_{abs}=-1.5$  V.

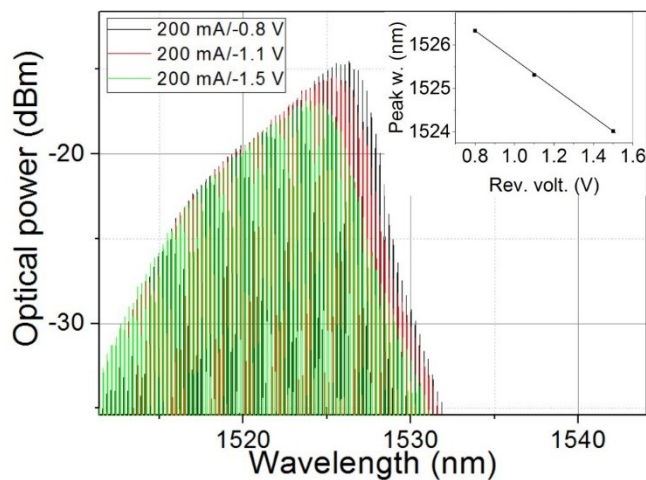


**Figure 3-9 Optical spectra of QDot MLL. Inset: peak wavelength vs reverse abs. Voltage**

This effect can be distinctly observed in Figure 3-10, where the comparison of optical spectra at different absorber voltages is given in linear scale. A pronounced tail in short wavelength region can be observed at higher absorber voltage, whereas at -0.8 V the blue slope of the spectrum is damped stronger.

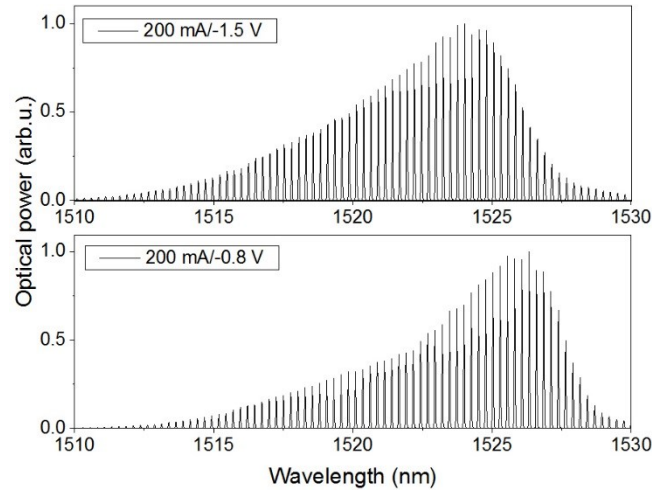


**Figure 3-10 Short wavelength tail at higher reverse voltage**

The optical spectra recorded at fixed absorber voltages and increased current demonstrates linear red shift with the rate of 0.04 nm/mA (Figure 3-11), being driven by heating of the device and subsequent band-gap shrinkage effect. QDot MLL optical spectra are neither symmetric nor hold a specific shape; moreover Figure 3-11 demonstrates distinct multimodal distribution as a result of inhomogeneous broadening. This type of broadening originates from several groups of quantum dots having different size or shape. Similar phenomenon is also observed in reference FP-lasers mentioned above.

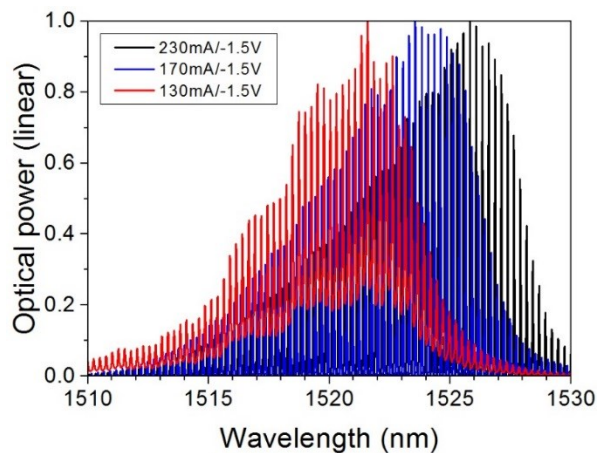


**Figure 3-11 Current dependent shift of QDot MLL optical spectra**

The spectra of the reference FP-lasers with the same cavity length as MLL processed from the same wafer are shown in Figure 3-12. It demonstrates inhomogeneously broadened spectra @  $4\times I_{thr}$  and  $6\times I_{thr}$  with distinct subgroups of the modes, which rise up with increased current due to band filling of QDot ensembles. The FWHM increases to a maximum value of  $\sim 6$  nm. Current dependent spectrum red shift is equal to  $0.07$  nm/mA, that is somewhat higher in comparison to MLLs spectrum red shift mentioned above.

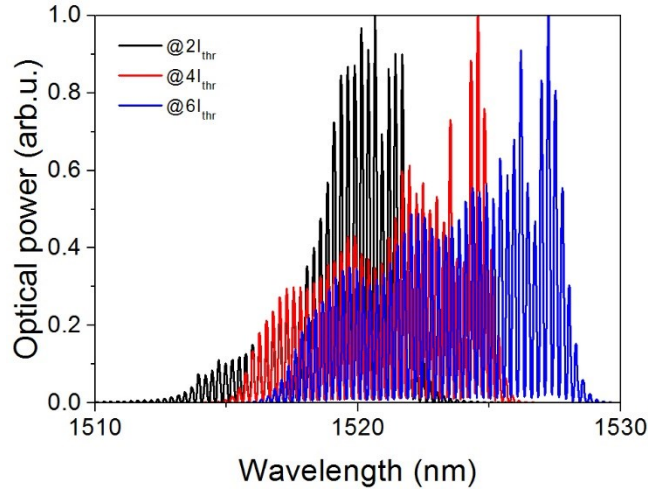


Figure 3-12 Lasing spectra of FP-laser for three different current

Further, the shift of the emission wavelength as a function of the laser cavity length is studied. Figure 3-13 illustrates the red shift with increased length. This result is in agreement with previous experimental investigations made on quantum-dot material and theory: shorter resonator length increases threshold gain, which is obtained through higher energy transitions [52], [53].

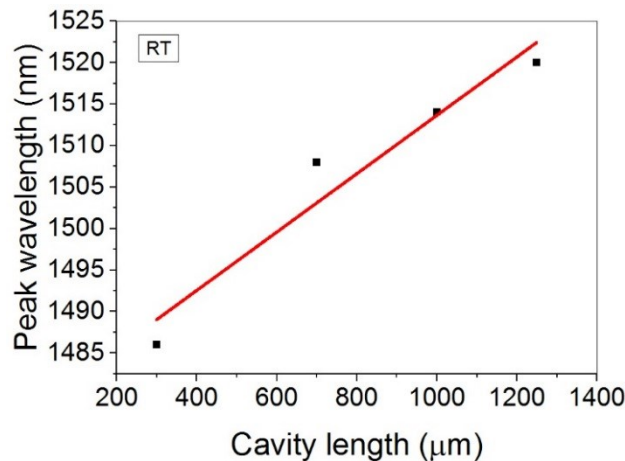


Figure 3-13 Effect of cavity length on the peak wavelength

### 3.1.2 QDash passively mode-locked lasers

The second measured PMLL is the QDash active material based two-section device with 1.5 mm long cavity length. The absorber-to-gain section ratio is equal to 1:7. Color-coded average optical power map is given in the Figure 3-14. Maximum emitted optical power is 26 mW, which is slightly higher than that of the QDot lasers due to the longer gain section length and larger GS to AS ratio. As can be seen, there are several average optical power bursts at  $U_{abs} \sim -0.6$  V, -1.9 V around the lasing threshold, which occur due to the saturation of the AS. The sudden changes in optical power at larger  $I_{inj}$  were observed in MOVPE grown QDot PMLL and addressed to the unstable dynamics of the optical field [23].

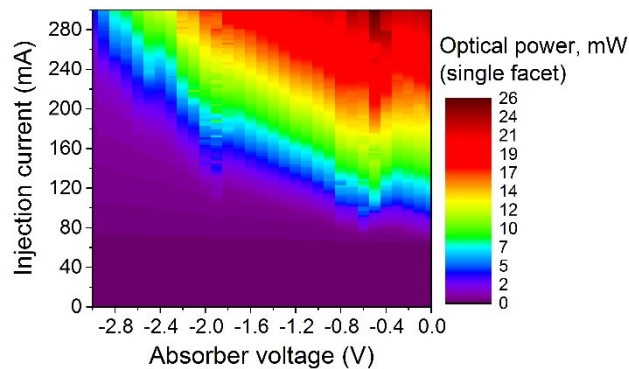


Figure 3-14 Two-section QDash laser optical power

The LIV-characteristics of the reference FP-laser from the same wafer with the same cavity length and QDash PMLL are illustrated in Figure 3-15. The threshold current density is  $1.49 \text{ kA/cm}^2$  for FP-laser, the differential quantum efficiency is 0.31, maximum output power is 34 mW, the series resistance is 5.8 Ohm and turn-on voltage is equal to 0.77 V. As in the case with QDot PMLL, hysteresis effect has not been observed here either.

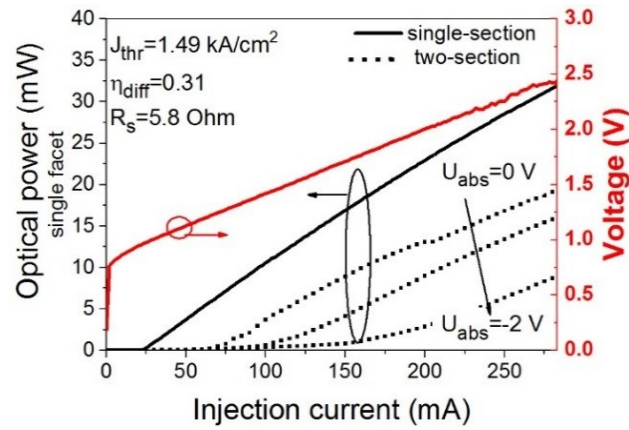


Figure 3-15 Light-current characteristics of QDash single- and two-section devices

Repetition frequency. The mode-locking frequency of QDash MLL is around 27.8 GHz, lower than that of QDot MLL due to the longer cavity length. The variation of the mode-locking frequency as a function of absorber bias at several gain section current values is shown in the Figure 3-16. Higher gain section current leads to the faster decrease of frequency due to enhanced heating effects.

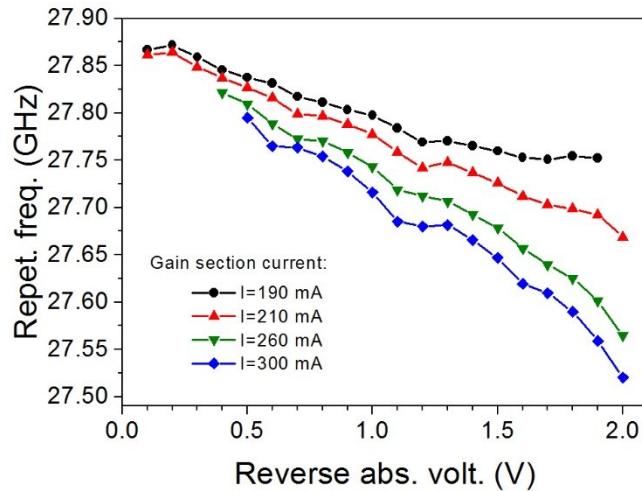


Figure 3-16 QDash MLL repetition frequency vs. reverse voltage

Similar behavior is observed when the repetition frequency is investigated as a function of gain section current (Figure 3-17). As in the case with QDot MLL, QDash MLLs demonstrate steeper decrease of mode-locking frequency at higher reverse voltage due to blue spectral shift and dispersion.

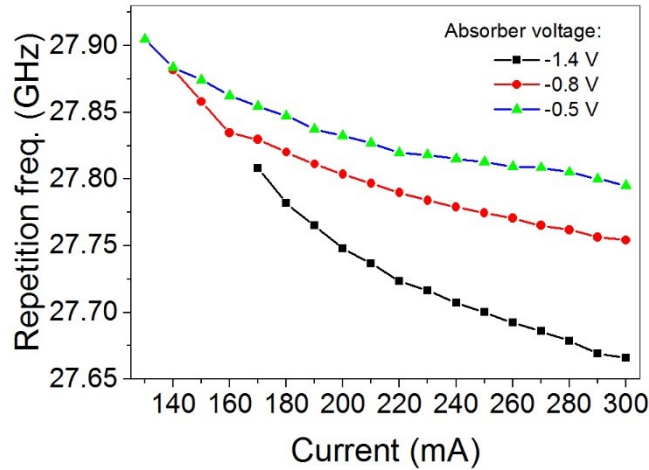


Figure 3-17 QDash MLL repetition frequency vs. gain section current

The repetition frequency vs  $U_{abs}/I_{inj}$  color-coded map is shown in the Figure 3-18. Although QDash laser ML-frequency behavior looks similar to QDot MLLs (see Figure 3-5), one can observe that the area of maximum frequency of QDash devices is forced to the region of low absorber voltage and low gain section current, unlike the QDot MLL, where the maximum frequency is spread more uniformly at the lower border of the map. The ML-region is found to be broader for QDash MLL due to larger gain-to-absorber section ratio.

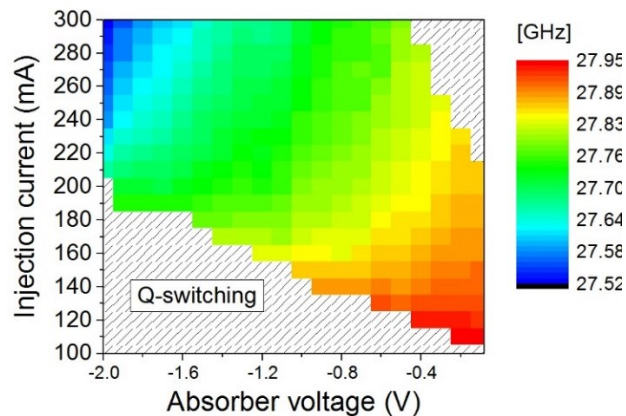
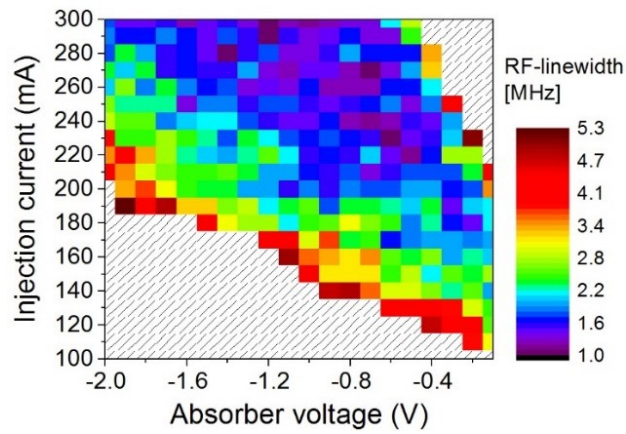


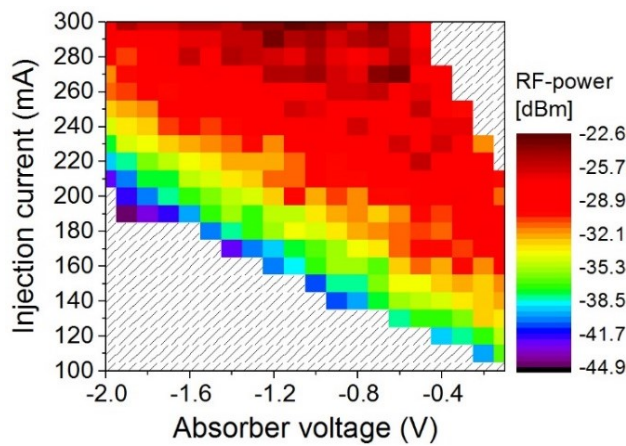
Figure 3-18 QDash MLL ML-frequency map

Systematic investigation of RF linewidth as a function of gain section current and absorber voltage were carried out. Figure 3-19 is a color-coded map showing a RF linewidth  $<5.3$  MHz in the whole stable ML region, the broadest linewidth is measured at the border of stable mode-locking. The lowest measured value of RF linewidth is  $\sim 0.96$  MHz. Despite longer gain section of QDash MLL, we did not observe an improvement of RF linewidth in comparison with QDot MLLs.



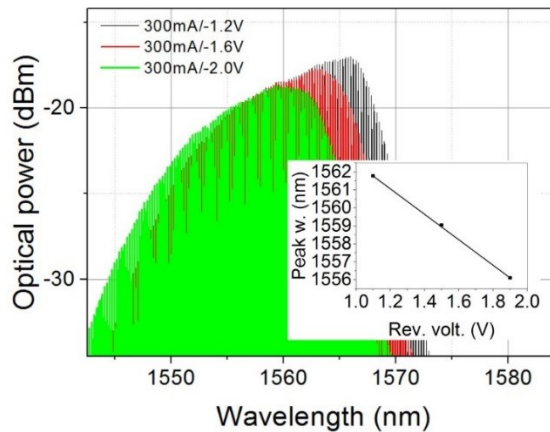
**Figure 3-19 QDash MLL: RF linewidth map**

Figure 3-20 illustrates the scan of RF peak power. The broad red colored area shows RF power values  $> -30$  dBm. In general, RF power degrades with decreased gain section current, whereas variation of the absorber voltage may lead to both enhancement and decrease of RF power.



**Figure 3-20 QDash MLL RF-peak power map**

Optical spectrum. The lasing spectrum of QDash MLLs is shown in Figure 3-21 at injection current of 300 mA and varied absorber voltage. Increased reverse absorber voltage leads to the blue shift of the emission wavelength. We address this to the increased absorption losses, which require the additional gain available from higher energy transitions. The slope of the spectral shift is  $\sim 7$  nm/V as shown in the inset, which is two times larger due to stronger absorption in comparison with QDot MLL. QDash MLLs demonstrate inhomogeneously broadened spectrum and the maximum spectral FWHM is  $\sim 12$  nm, that is larger than those measured for QDot MLLs.



**Figure 3-21 Optical spectra of QDash MLL. Inset: peak wavelength vs reverse abs. voltage**

The spectra of the reference QDash FP-lasers with the same cavity length as MLL processed from the same wafer are shown in Figure 3-22. As in the case with QDot FP-lasers, we observe inhomogeneously broadened spectra consisting from mode subgroups stemming from QDash ensembles with specific size and shape. Current induced spectral red shift of reference QDash FP-laser is only 0.03 nm/mA, which is more than two times smaller in comparison with QDot FP-lasers. This is quite unexpected, because longer cavity lasers demonstrate worse wavelength stability as shown e.g. in [15], [54]. The improved wavelength stability is addressed to higher order transitions, which balance the effect of bandgap shrinkage [52].

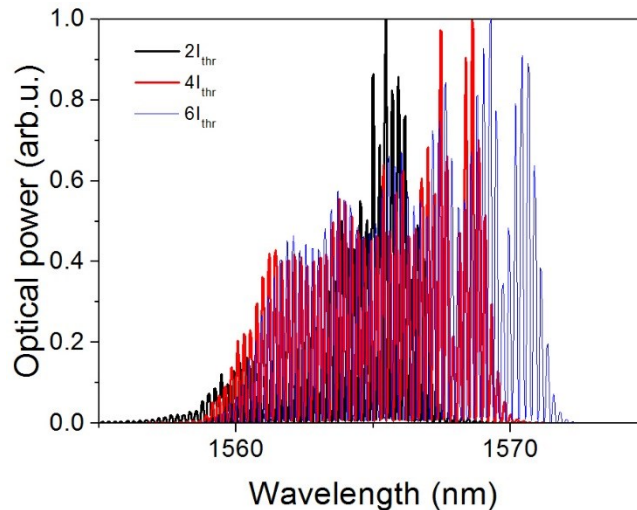
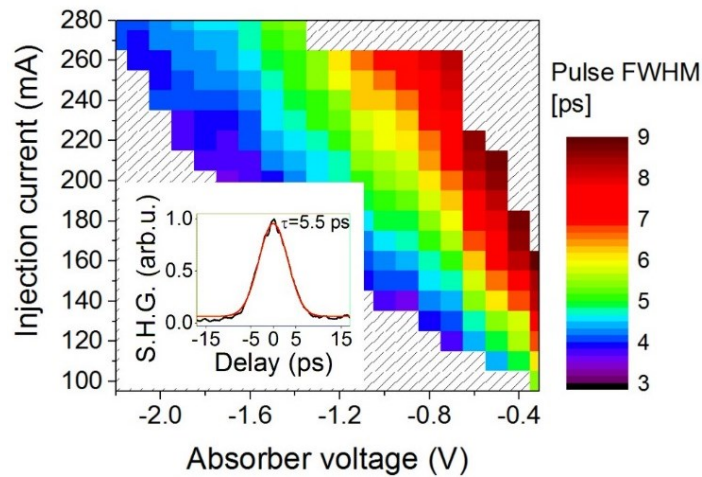


Figure 3-22 Lasing spectra of QDash FP-laser for three different current

### 3.1.3 Measurement of optical pulses

Several techniques are available for pulse width measurement. The most common are autocorrelator, streak camera and sampling oscilloscope with photodetector. The duration of the measured pulse imposes strict limitation on their characteristics. QDot and QDash MLLs emit sub-picosecond pulses, whereas the combination of fastest photodetector and oscilloscope are capable of measuring 10 ps pulses; streak camera based approach needs fast continuously tunable triggering, which is not available in case of ps and sub-ps pulse sequences. Intensity autocorrelation (AC) measurements through second harmonic generation (SHG) meet the requirements of high bandwidth and sensitivity. In this subsection, we provide the results on AC based pulse width measurement.

Color-coded pulse FWHM map measured for QDot MLL after deconvolution assuming Gaussian pulse shape is shown in Figure 3-23. Some data points are excluded from the plot corresponding to  $I=270-280$  mA at  $U_{\text{abs}}=-3 - -0.7$  V, since AC traces show CW operation under these operating conditions. This happens when pulse width is large enough and overlaps with the neighbor pulse, so that autocorrelator cannot resolve two separate pulses. As shown in Figure 3-23 the increase of absorber voltage inhibits this effect.



**Figure 3-23 Pulse FWHM color map of QDot MLL, in the inset AC-trace at  $I_{inj} = 200$  mA,  $U_{abs} = -1.0$  V**

We point to the minimum measured pulse FWHM of 3.7 ps, being the shortest pulse width ever measured ex-facet in QDot PMLL. The FWHM increases with increased current at fixed  $U_{abs}$ , because at higher current the absorber bleaches faster as pulses carry more power, also gain is enhanced leading to the broadening of the net gain window. On the other hand, at higher  $-U_{abs}$  and constant  $I_{inj}$ , pulses get shorter due to reduced absorber recovery time as carriers experience a faster escape from the QDs to the barrier [55], [56]. Unfortunately, benchmarking with other MOVPE-grown InP/InAs QDot PMLL is hardly possible: only Tahvili et al. demonstrated several tens of ps broad pulse emission ex-facet at 10 GHz repetition rate [36] at 12<sup>o</sup>C. To our knowledge, we present the only known MOVPE-grown QDot MLL operating at room temperature.

Similar pulse FWHM dynamics is observed in QDash PMLL with the smallest width of 4.7 ps ex-facet Figure 3-24. As can be seen in comparison with Figure 3-23, reduced absorber-to-gain length ratio in QDash MLL tends to increase minimum pulse FWHM. Several research groups presented ex-facet pulse emission from QDash PMLL: Sooudi et al. [57] and Rosales et al. [58] demonstrated 3.3 ps (Sech-fitted, 20.7 GHz repetition rate) and 2.5 ps (Gaussian fit, 48 GHz repetition rate) pulse width from Gas MBE-grown laser samples respectively.

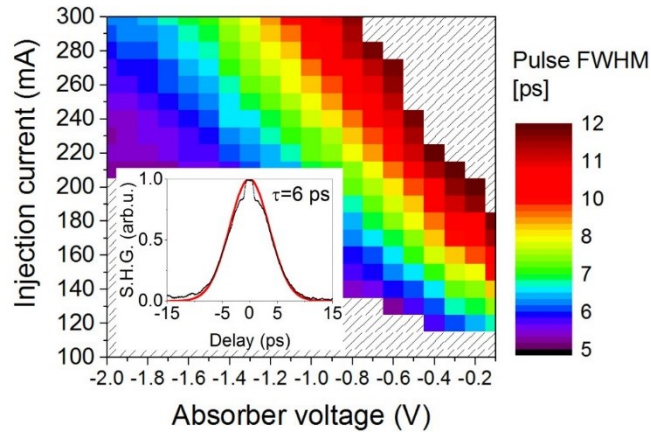


**Figure 3-24** Pulse FWHM color map of QDash MLL, in the inset AC-trace at  $I_{inj} = 200$  mA,  $U_{abs} = -1.2$  V

There is a spike on the top of the AC-traces both for QDot and for QDash MLL, as can be observed in the insets of Figure 3-23 and Figure 3-24. It may arise from significant level of spontaneous emission, or slow operation of the absorber can be a reason. Faster saturation of the absorber can be achieved by applying higher reverse bias, however the gain should be enlarged at the same time (which is also beneficial for the suppression of ASE (amplified spontaneous emission)-noise) for stable ML operation.

Time-bandwidth product (TBP) is further estimated for both QDot and QDash PMLL. TBP is defined as the product of temporal pulse width and its spectral width. Implying Gaussian pulse and spectral shape, the minimum achievable TBP is equal to 0.44; such pulses are called Fourier transform limited. However real pulses show TBP larger than this ideal value, this may result from non-linear pulse chirp, intracavity dispersion and non-Gaussian pulse shape. In Ref. [57], [58] authors report on TBP values of 9.48 and  $>1.5$  respectively measured for QDash PMLL, transform limited pulses are reported for GaAs-based QDot PMLLs [59] as well as InP-based quantum-well devices [60]. Figure 3-25(a) is calculated TBP at fixed reverse absorber voltage (1.5 V for QDot and 1.1 V for QDash). At low gain current QDash PMLL shows almost two times higher TBP value. We note here that at increased gain current pulse width increases almost linearly both for QDash and for QDot devices, but two times faster for QDash lasers. QDot spectral FWHM follows decrease tendency with increased current (probably due to complicated absorption dynamics), along with slower pulse width increase rate, this leads to flat TBP curve. On the contrary, spectral FWHM of QDash PMLL grows with current, thus broadening spectrum and fast increase of pulse result in large qualitative and quantitative difference between investigated TBP of QDot and QDash PMLLs. QDash lasers reach TBP values larger than 14,

whereas for measured QDot devices  $TBP < 4$ . As plotted in Figure 3-25(b) at fixed gain current (200 mA) and varying reverse voltage QDash lasers still demonstrate non-uniform TBP behavior (mostly due to the spectral FWHM behavior which does not follow a clear tendency) with decrease trend, in contrast to QDot counterparts (spectral FWHM grows linearly with increased reverse voltage) with small changes of TBP value which is still smaller than 4.

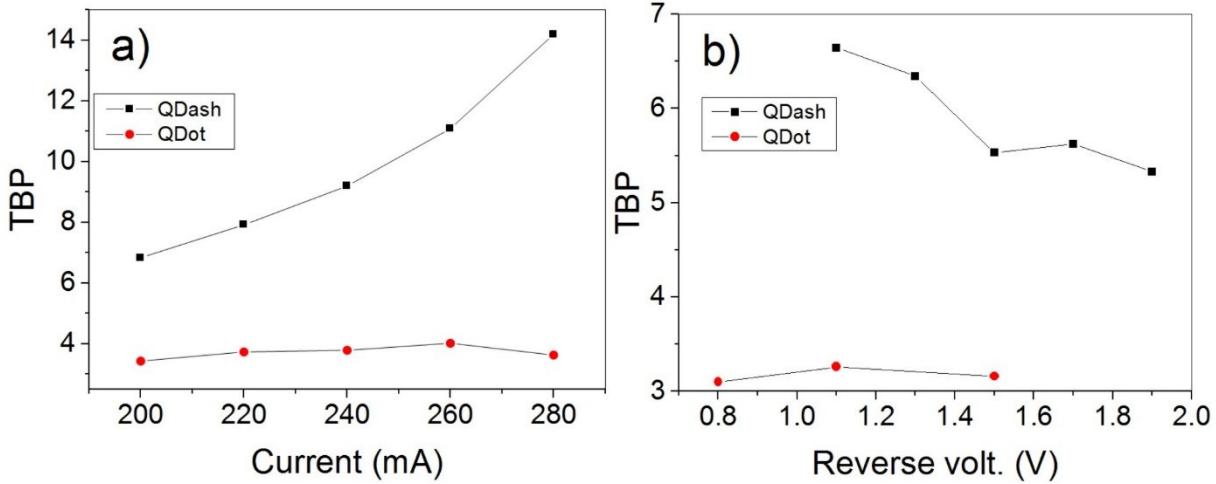
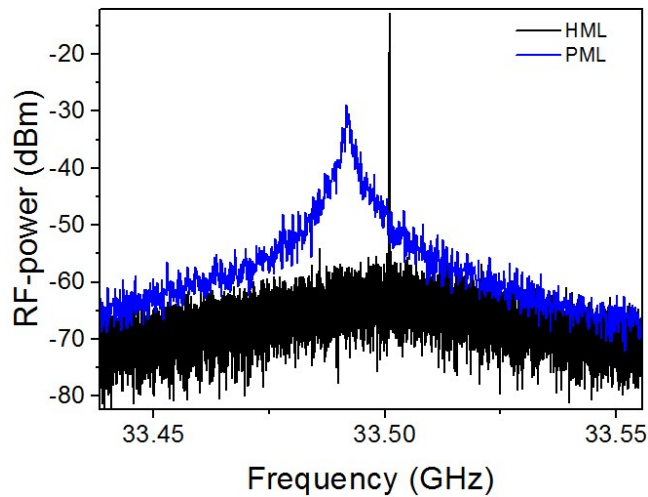


Figure 3-25 TBP of QDot and QDash PMLL as a function of varying: a) current; b) reverse absorber voltage

### 3.1.4 Hybrid mode-locking

The hybrid mode-locking (HML) implies a high frequency modulation of the reverse biased absorber section. The frequency of the external signal should match the inherent repetition frequency of the MLL with some bandwidth tolerance, which called the MLL locking range and depends on the strength of applied RF-signal. Therefore, hybrid mode-locking may be used e.g. to overcome the cleaving inaccuracies or serve as a clock/synchronization source. Another important HML feature is the jitter reduction. In Figure 3-26 we present the RF spectra of the same QDot MLL biased at -1.1 V and 200 mA in HML ( $f_{\text{ext}}=33.501$  GHz,  $P_{\text{ext}}=-15$  dBm) and PML (passive mode-locking) regime. Obviously the RF linewidth gets significantly narrower in Hz-range (below 10 kHz resolution BW (bandwidth) limited), indicating the reduction of the jitter, furthermore the noise level drops down and the carrier power enhances thus carrier-to-noise ratio improves underlining the overall improvement of ML performance.



**Figure 3-26 RF spectrum for hybrid (HML) and passive (PML) mode-locked laser. The device is biased at -1.1 V and 200 mA**

The locking range. As mentioned above, the locking range is the frequency range of the external signal, when the MLL is still able to follow the external signal. The width of the locking range as a function of modulation power for different reverse voltages with fixed gain section current is shown in Figure 3-27(a). The locking range increases with larger RF-power and decreases with increased reverse voltage, with the maximum width of 76 MHz at -10 dBm modulation power.

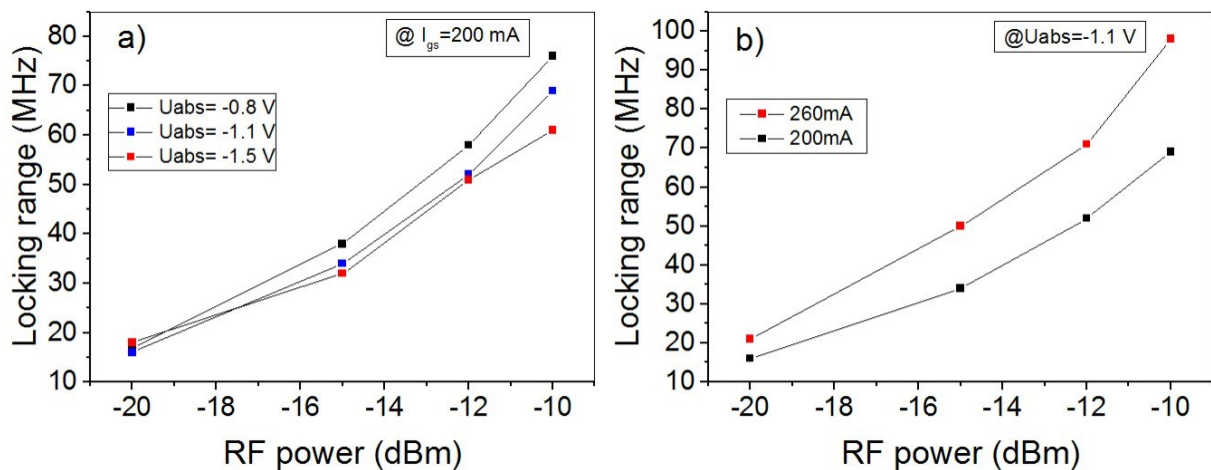


**Figure 3-27 QDot HML frequency locking range vs applied RF-power. (a) Three lines denote different absorber voltages at constant gain section current of 200 mA; two lines denote different gain section currents at constant absorber voltage of -1.1 V**

Later on, we fixed the absorber voltage at -1.1 V and measured the locking range versus RF power at 260 and 200 mA of gain section current (shown in Figure 3-27(b)). We observe a larger locking range for larger gain section current. The locking range of almost 100 MHz has been

achieved at  $I_{gs}=260$  mA and -10 dBm modulation power. The experimental results are in a good agreement with the results of the modelling based on the delay differential equations [61] and experimental results therein, though showing narrower locking range <15 MHz. The boundaries of the locking range at fixed gain section current and varied absorber voltage are presented in Figure 3-28. The QDot MLL repetition rate follows the external signal frequency inside the area created by the points of the same color corresponding to a specific bias condition. The locking region is asymmetrical with respect to the detuning frequency as was reported before in [45], [61] due to nonlinear dependence of the MLL repetition frequency on the pulse amplitude [61], the detailed explanation of this phenomenon falls outside the scope of this work and can be found in [62].

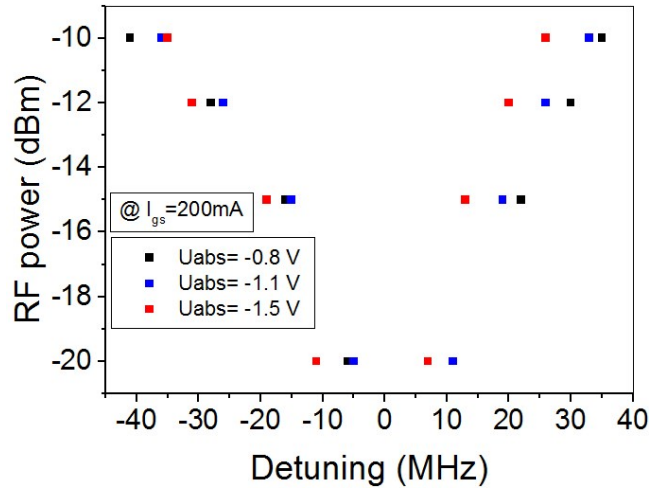


Figure 3-28 The boundaries of the locking range at fixed gain section current and varied absorber voltage

### 3.1.5 Discussion

The results presented above show similar pulse width vs operating parameters dynamics irrespective of active zone material type. Optical spectra of investigated QDot and QDash devices demonstrate pure ground state emission. We have observed ex-facet picosecond range pulse emission from both QDot and QDash PMLL, however time-bandwidth product is found to be smaller for QDot PMLL. We report on a weak coherence artefact in the autocorrelation traces of QDot and QDash PMLLs, which could be addressed to background spontaneous emission. The hybrid mode-locking was investigated experimentally on QDot MLL, showing asymmetrical locking area. RF linewidth reduced to several KHz, which implies a significant reduction of the jitter.

### 3.2 Mode-locking in single-section devices

Fabry-Perot (FP) semiconductor lasers can also exhibit a mode locking, such devices are also called single-section mode-locked laser (SSMLL) and the phenomenon is referred as „self pulsations“. Mode locking was demonstrated in FP lasers based on Qwell [47], [63], bulk [64], QDash [58] and QDot [36], [38], [65] active material. Hence, mode locking phenomena in FP-lasers does not depend on the dimensionality of the gain material. However, inhomogeneously broadened QDot and QDash gain spectrum is favorable for ps and sub-ps pulse emission, which will be shown in this section.

The origin of self pulsations is not clear yet but several limited theoretical models address it either to the intracavity four-wave mixing process (FWM) [42], random population of quantum dot groups where some of them act as absorption centers [66] or coupling between spatial modes [67]. Indeed, the beating at intermodal frequency may originate from carrier density pulsation, which involves the carrier transition and relaxation between reservoir and lasing states in the picosecond range time scales. This type of nonlinear interaction is strong but suffers from the slow dynamics, which implies its limited bandwidth. On the other hand, spectral hole burning and carrier heating process prevail at sub picosecond range and responsible for locking of modes from farther part of the spectrum, however, the efficiency of this interaction is low due to the dephased interplay between them [68].

In contrast to two-section MLLs, such pulse characteristics as repetition frequency, RF-linewidth, pulse width can be controlled only by gain variation of device, thus being less flexible in comparison to two-section MLL, but the absence of the passive section would result in higher optical output power and lower background spontaneous emission level. Similar to two-section MLL, the repetition rate of optical pulse train emitted by SSMLL is given by the cavity length.

#### 3.2.1 QDot single-section mode-locked lasers

As was mentioned in prior subchapters SSMLL are located on the same laser bars with PMLL and were addressed as reference lasers. Light-current characteristics and optical emission spectrum are shown in Figure 3-1 (solid line) and Figure 3-12 respectively. ML properties of QDot SSMLL are first investigated by recording RF and optical spectra. The color-coded map of QDot SSMLL RF and optical spectrum are shown in Figure 3-29 and Figure 3-30 respectively. Unlike PMLL, the repetition frequency of QDot SSMLL follows increase trend explained by

material dispersion. Thermal expansion manifests itself after 250 mA as ML frequency undergoes reduction. The RF behavior is free from instant and sharp frequency hopping, reported e.g. in [69], where author addresses this effect to the distinct supermode competition. This effect is masked here, as can be observed from spectrum plot in Figure 3-30. Expected red shift of the emission spectrum with increasing current is observed, and the optical distribution is found to be uniform with no regions with abrupt spectrum kinks. Nevertheless, step-like behavior of the „blue“ spectrum boarder at  $\sim 125$ ,  $\sim 165$ -170 mA in Figure 3-30 correlates with increased RF-linewidth and trend sign change (at  $\sim 250$  mA) in Figure 3-29, this effect can be addressed to the supermode competition mentioned above. Interestingly, the band filling effect manifesting itself in the blue shift of short wavelength spectral region and occurs at currents  $< 160$  mA (Figure 3-30). At larger current, this effect is completely suppressed apparently due to the carrier escape process and band-gap shrinkage.

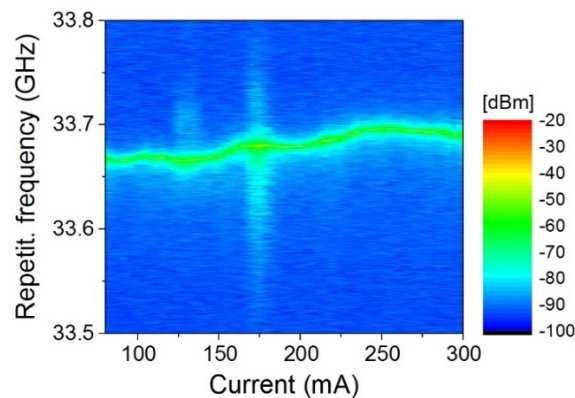


Figure 3-29 QDot SSMLL RF spectrum color coded map

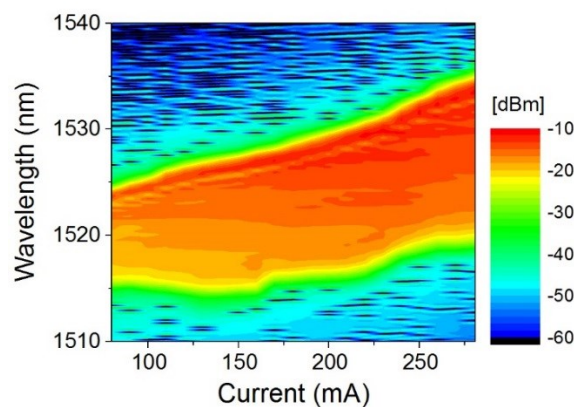


Figure 3-30 QDot SSMLL optical spectrum color coded map

Co-existence of supermode ensembles can be extracted from RF linewidth behavior. Figure 3-31 illustrates RF-linewidth evolution, which is further considered jointly with Figure 3-29 and Figure 3-30. Obviously, the instantaneous changes of RF-linewidth have a relationship with similar hopping effects observed for RF and optical spectrum: RF linewidth increases sharply near injection currents where step-like behavior of optical spectrum is observed. RF-linewidth increases when the supermodes with comparable optical gain are competing with each other to set the laser in ML condition, this process is accompanied by significant increase of RF linewidth, indicating more severe impact of spontaneous emission resulting in increased optical phase noise. Once one of the supermodes takes over, the laser follows the ML regime corresponding to this specific supermode. Then, this fact should be also observable in pulse width vs current dependence; this was indeed confirmed by means of intensity AC function measurement. Figure 3-32 shows the dependence of the pulse width on current, assuming deconvolution factor of 0.5 for Lorentzian pulses.

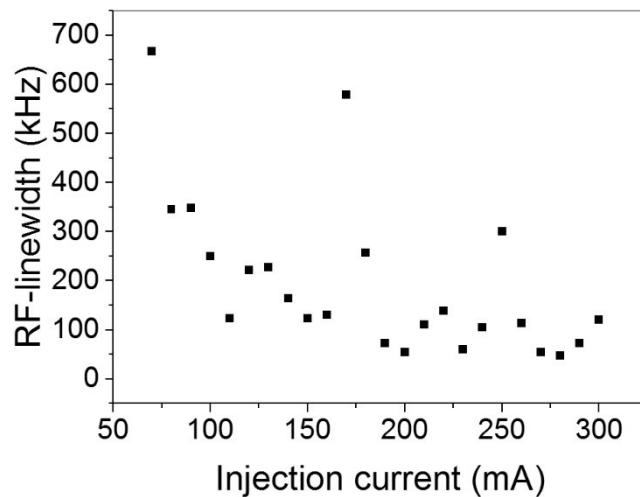


Figure 3-31 QDot SSMLL RF-linewidth

The period of the pulse train corresponds to the inverse of the ML frequency and the lowest pulse width is  $\sim 800$  fs resulting in a TBP of 0.68. A large discrepancy between this value and Fourier transform limit, which is 0.22 for Lorentzian profile pulses can be attributed to the residual and high order chirp and mismatch between real and assumed spectral profile. We observe that sign change of the trend in Figure 3-32 corresponds to instant bursts of RF-linewidth, which is in turn correlates with ML frequency and optical spectrum dynamics. Single-section mode locking phenomena still lacks comprehensive theoretical explanation, but intracavity four-wave mixing effect is most often referred as a responsible mechanism [42], [63],

[70]. At low current the pulses are broad, because along with lower optical FWHM, the efficiency of  $\chi^{(3)}$  is not enough to set up phase correlation between optical modes [71]. With increased current (80–280 mA), more optical modes are excited and intra-cavity nonlinearities are strong enough to lock their phases, leading to short pulse formation, thus a flat region of the characteristic in Figure 3-32 is built-up. At currents larger than 280 mA pulse FWHM increases again, which is probably due to the increased number of excited modes inducing unsynchronized phase interference, but in particular due to a larger  $\alpha$ -factor and hence increased chirp [72], [73].

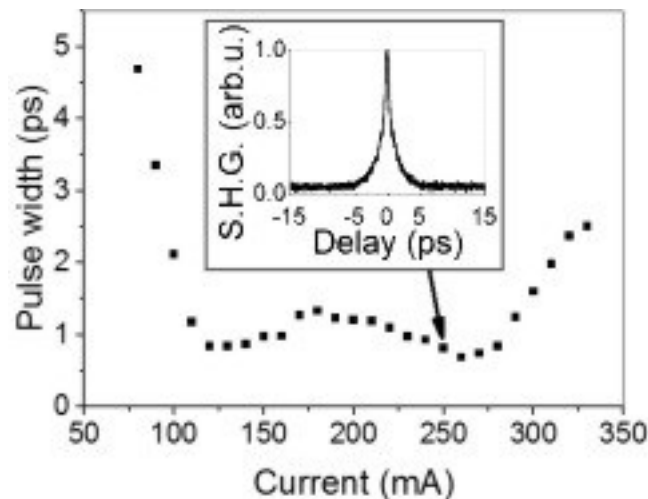
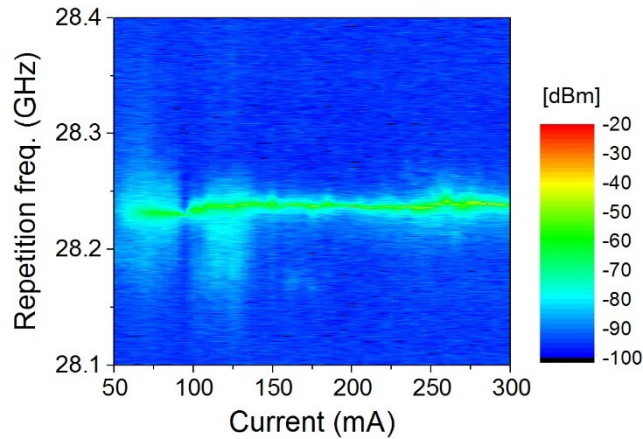


Figure 3-32 Pulse width with AC-trace (inset) after compression

### 3.2.2 QDash single-section mode-locked lasers

Systematic ML-frequency measurements as a function of current were conducted for QDash FP-laser, previously referred as the reference device, exactly as in the case with QDot lasers. Figure 3-33 QDash SSMLL RF spectrum is plotted with the same scale as Figure 3-29 for the purpose of better comparison and shows rather smooth and uniform distribution in contrast to QDot laser's ML frequency behavior. One can distinguish a noisy RF emission at 50–140 mA, but in general, the curve is constant. The further explanation of such a performance would need an ML analysis of optical/RF spectral and time domain characteristics.



**Figure 3-33 QDash SSMLL RF spectrum**

Optical spectrum of QDash SSMLL as a function of current is plotted in Figure 3-34. Optical spectrum of QDash SSMLL unlike QDot demonstrate no step-like effects. The broadening of the spectrum is due to the shift of „red“ (upper) and „blue“ (lower) spectral boundaries towards longer and shorter wavelengths respectively due to device heating and band filling effect. Lower boarder shifts noticeably slower considering less effective band filling of higher states. At the current of  $I > 250$  mA abrupt red shift of both red and blue spectral boundaries is attributed to bandgap shrinkage. One can see that, in this particular case no correlation between optical and ML frequency dynamics can be found in contrast to QDot SSMLL.

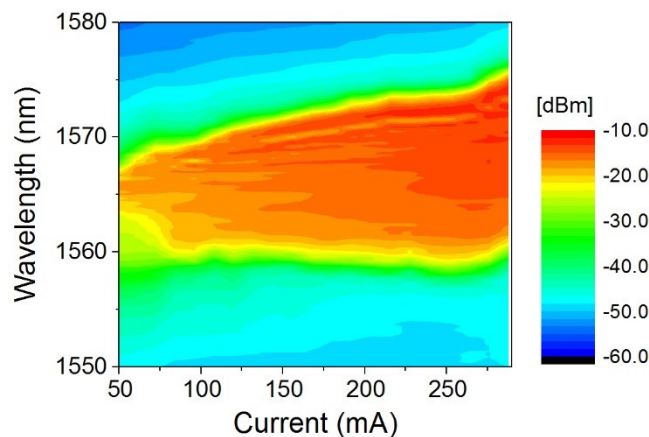


**Figure 3-34 QDash SSMLL optical spectrum**

The evolution of RF linewidth as a function of current is shown in Figure 3-35 QDash SSMLL RF-linewidth. General decrease trend is observed. RF-linewidth of several hundred up to  $10^3$  of kHz coincides perfectly with noisy RF emission at 50–140 mA (see Figure 3-33 QDash SSMLL

RF spectrum) as well as the pronounced dip at 95 mA corresponding to 70 kHz of the linewidth. RF linewidth in the order of 110 kHz and below is observed at  $I > 170$  mA.

Figure 3-36 illustrates autocorrelation measurement results where the pulse width generally increases with increased current. The linear region takes place at the current of  $\sim 150$ – $250$  mA, being in a good agreement with the uniform RF behavior (Figure 3-33) as well as RF linewidth curve shown in Figure 3-35. The minimum pulse width measured is  $\sim 550$  fs after compression, assuming Lorentzian pulses, this correspond to TBP value of 0.38. It can be noted that the pulse width curve irregularity at  $I > 250$  mA coincides with ML frequency oscillation and red shift of the optical spectrum. Apparently, no supermode switching takes place, as pulse width curve follows perfectly the previous trend, and RF frequency/linewidth reveal no severe instabilities or discontinuity. In general, QDash SSMLL performance characteristics imply that apparently supermode competition does not takes place in these of devices. Accordingly, single group of modes exists which governs ML dynamics and determines its characteristics.

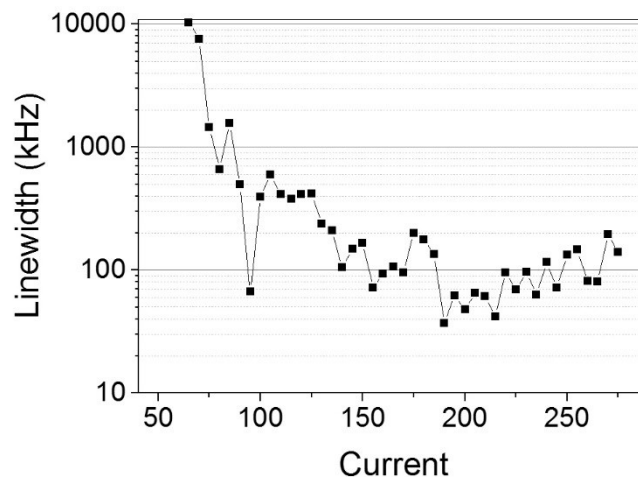


Figure 3-35 QDash SSMLL RF-linewidth

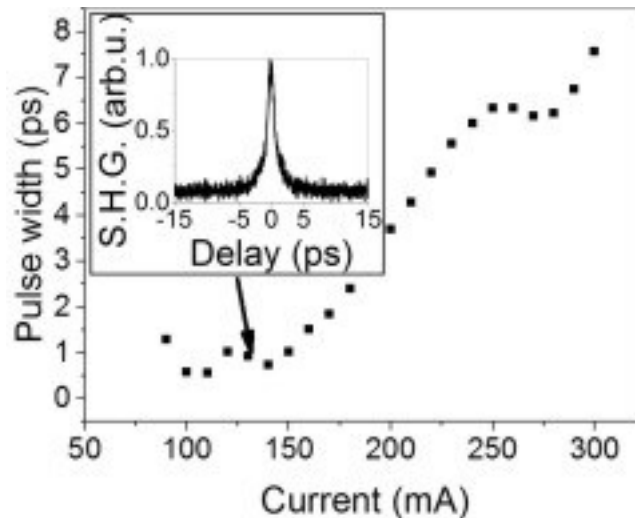


Figure 3-36 Pulse width with AC-trace (inset) after compression

### 3.2.3 Discussion

Although the comprehensive theoretical background of SSMLL phenomenon does not still exist, we are still able to discuss discovered performance properties of QDot and QDash SSMLL and make general conclusions with a certain degree of caution, about the impact of active material type on ML characteristics. Firstly, the value of RF linewidth (as a figure of merit for optical phase noise) is around 100 kHz in steady state regime for both type of devices. We do not observe any supermode competition in the optical spectrum of QDash SSMLL; this is supported by almost flat and constant dependence of ML frequency and linear behavior of pulse width characteristics in the large range of operating parameter. The optical spectrum of QDash SSMLL demonstrates gradual broadening with the increased current almost in the whole range of applied current due to gradual band filling effect. While for QDot SSMLL spectral broadening is observed only in the short range of applied current (probably due to carrier escape and gain saturation), followed by step-like behavior of „blue“ part of the spectrum towards longer wavelengths. Presumably, this phenomenon originates from supermodes competition. Our assumption relies on the RF linewidth curve, showing instant bursts at operating conditions where hops of optical spectrum appear. ML frequency as well as pulse width are also affected: both characteristics experience non-negligible slope sign change. Generally, ML frequency of QDot SSMLL is less stable in comparison to QDash SSMLL due to a chromatic dispersion of supermode.

### 3.3 Frequency resolved optical gating techniques based investigations of InP/InAs nanostructure mode-locked lasers

Second harmonic generation based autocorrelation (AC) techniques used in previous sub-chapters to define pulse width is well-known and extensively employed instrument. However, such pulse properties as shape and chirp cannot be extracted using AC. The ambiguity of the AC can be overcome by FROG (Frequency-Resolved Optical Gating) techniques where AC is spectrally resolved. SHG FROG measurement setup consists of a delay module, autocorrelation module, monochromator and CCD-camera [74]. The pulse shape and chirp are important both from application and fundamental point of view. In optical communication the pulse shape must be as simple as possible and it is important to avoid complicated pulse shape (intensity bursts, peak splitting) so that the photodetector does not get misled. To control pulse propagation in optical fiber pulse chirp should be considered. Generally, these properties are crucial for a laser design optimization. Besides that, pulse shape and chirp help to understand the fundamental light-matter interaction process and pulse generation mechanisms. In this section, we experimentally investigate shapes of QDot/QDash SSMLL emitted pulses.

In Figure 3-37(a) we show FROG spectrogram measured for the QDot SSMLL described in section 3.2.1 at 100 mA of injection current. The spectrogram shows some satellite sub-pulses formed by longer wavelength part of the optical spectra. The temporal FWHM of the reconstructed optical pulse (Figure 3-37(b)) is 0.98 ps with a retrieval error of 0.004.

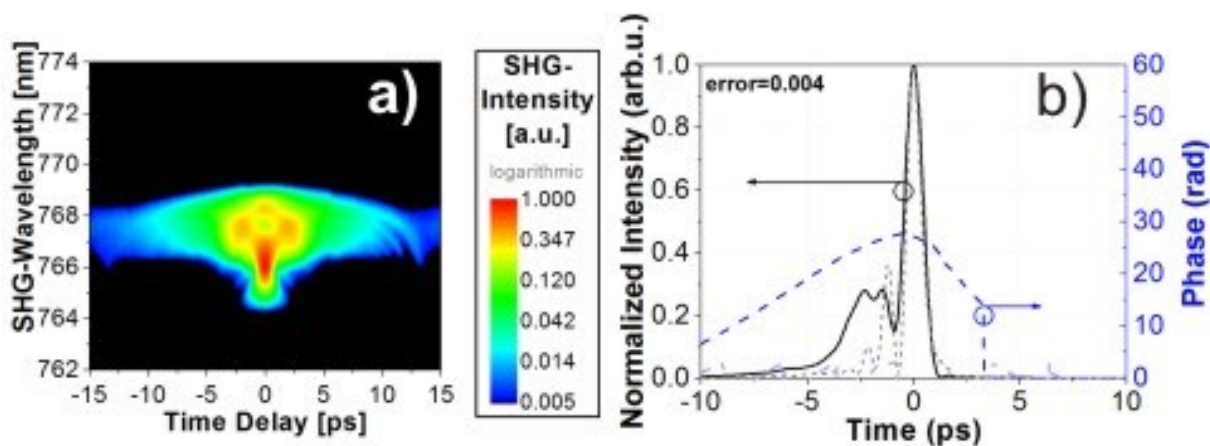


Figure 3-37 (a) FROG spectrogram; (b) reconstructed pulse and pulse phase measured for QDot SSMLL at 100 mA (solid line), dashed line represents the effect of linear chirp compensation on the pulse shape

Pulse reconstruction reveals complicated pulse shape: the leading edge consists of the overlapping sub-pulses and slowly rising plateau. The temporal phase has negative sign and not purely quadratic, this means that the chirp is positive but not completely linear. Therefore, SMF-28 in principle can be used to compensate the linear part of the chirp. The spectrogram corresponding to the injection current of 250 mA is shown in Figure 3-38(a). We observe the formation of the tiny sub-pulses. The increase of the injection current from 100 mA to 250 mA leads to a flip of the temporal phase's sign, as shown in Figure 3-38(b) so the dispersion of the SMF-28 is no longer suitable for the chirp compensation.

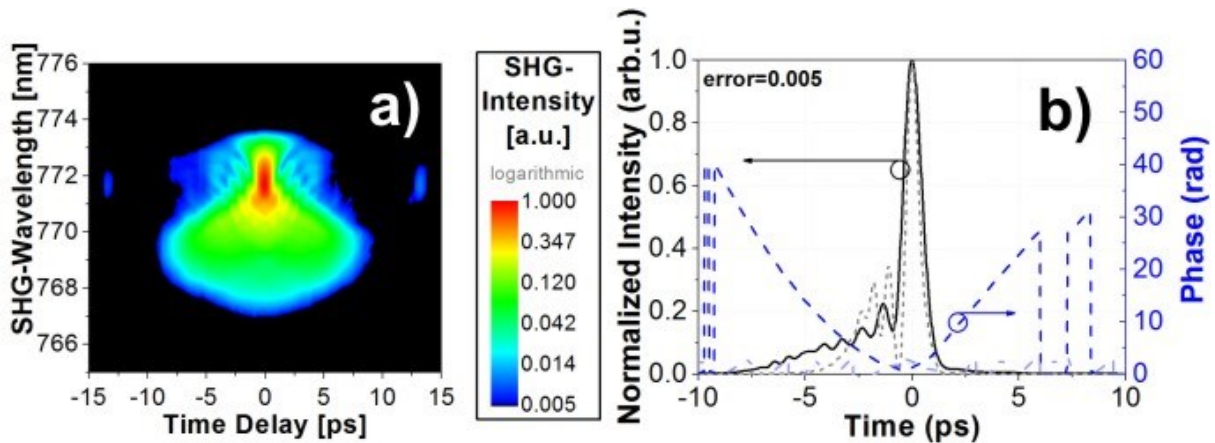


Figure 3-38 FROG spectrogram (a); (b) solid line – reconstructed pulse and pulse phase measured for QDot SSMLL at 250 mA, dashed line represents the negative effect of linear chirp compensation

The plot in Figure 3-38(b) shows pulse shape close to one measured at 100 mA with several oscillating sub-peaks on the leading edge and inclining plateau. The origin of the oscillations is still unknown due to the lack of theoretical fundamentals of single-section mode-locking phenomena, but could be addressed to uncompensated and higher order dispersion [75]. The pulse FWHM is 1.01 ps with a reconstruction error of 0.005.

QDash SSMLL, described in section 3.2.2, have also been characterized in terms of pulse shape and phase using FROG. We have not observed any difference in current dependent spectrogram, pulse shape and pulse chirp dynamics, the reconstruction error was  $\sim 0.005$  being similar with the error in the case of QDot SSMLL. We, therefore, believe that the type of nanostructure in the investigated devices does not affect the pulse shaping mechanism.

### 3.4 Gain switching of InP/InAs nanostructure based laser

Gain switching is optical pulse generation techniques based on direct driving of a laser with electrical pulses. During gain switching, periodical nanosecond range electrical pulse terminates after excitation of first relaxation oscillation (RO) peak, thus yielding higher peak optical power, which is the primary interest for applications. The trailing pulse limits achievable peak power and therefore must be suppressed. One of the trailing oscillations suppression method is the incorporation of a short absorber section and asymmetric waveguide [76], authors of ref. [77] suggest optical filtering. In our experiment we employ standard Fabry-Perot QDot laser, electrically pumped using pulse generator. Laser's intrinsic turn-on delay sets the minimum required length of the electrical pulse, and depends on current density. Hence, the repetition rate of an optical pulse train depends on the width of the first RO peak, which is inverse proportional to the frequency of RO and the laser's turn-on delay. The laser's turn-on delay is an inevitable phenomenon: the photon emission cannot start instantaneously with bias and depends on the carrier dynamics. Faster dynamics leads to a shorter turn-on delay. When the laser is biased from its initial off state, then the turn-on delay  $t_s$  is given by the carrier recombination time  $\tau_c$  and its threshold current  $I_{thr}$  [78]:

$$t_s = \tau_c \ln \frac{I_{bias}}{I_{bias} - I_{thr}} \quad (3.3)$$

Figure 3-39 shows laser (QDot active material, 770  $\mu\text{m}$  long cavity) turn-on process for several values of bias currents. The RO intensity curves in Figure 3-39 reveal strong optical intensity peak after turn-on delay (time axes are uncalibrated for the red curve corresponding to the shortest delay) and strongly damped RO peaks of higher order as was theoretically predicted (see Ref. [79]–[81]).

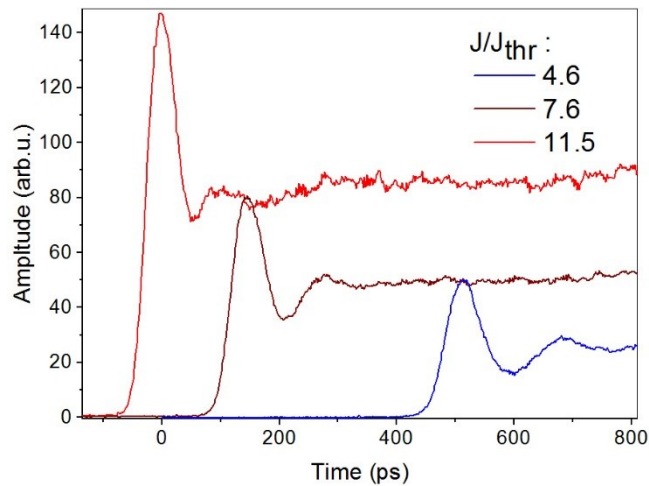


Figure 3-39 RO curves at different injection current density

Strong damping is fundamental feature of the lasers with decreased dimensionality of the gain material and stems from the ultrafast carrier scattering between lasing and reservoir states [80]. Increased nonlinear scattering rate leads to the reduction of the turn-on delay, stronger damping and the increase of RO frequency (accompanied by the shortening of first RO peak). In Figure 3-40 turn-on delay vs bias is plotted, carrier lifetime extracted from the linear fit function according to Eq. 3 amounts to 3.3 ns. The laser should be biased above the threshold to shorten the turn-on delay. The lasers with minimum turn-on delay are preferable in optical communications, but an intrinsic finite turn-on delay will always impose a limitation on applications with on/off keying modulation formats.

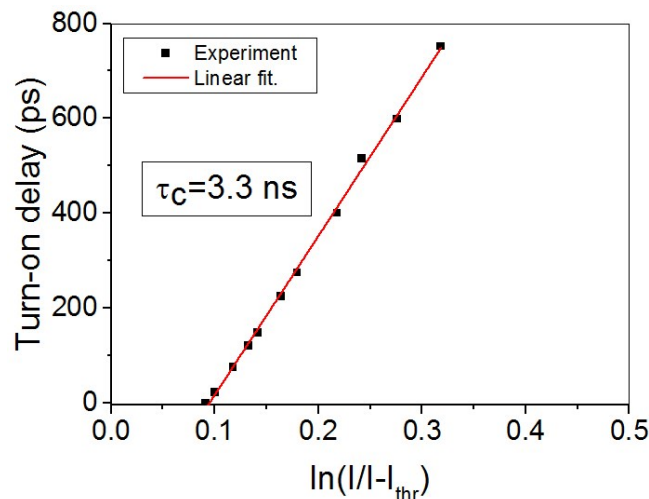


Figure 3-40 Turn-on delay vs natural logarithm of current to current minus threshold ratio

The correlation between RO frequency and peak width is shown in Figure 3-41 and the inset. RO frequency increases whereas peak FWHM decreases with increased current density.

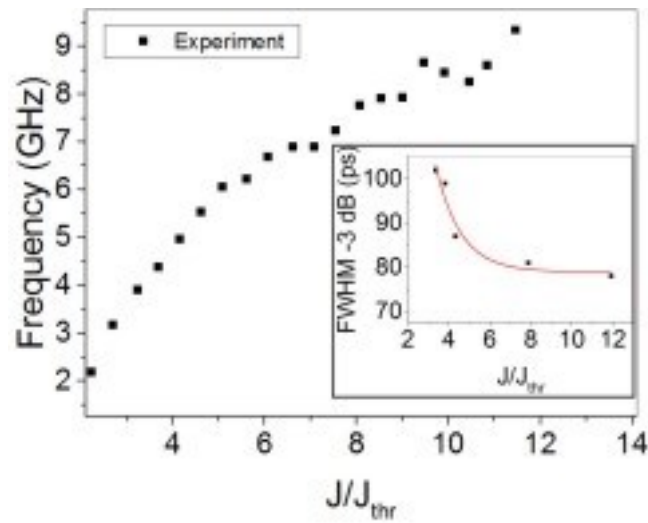


Figure 3-41 RO frequency (RO peak FWHM in the inset) vs normalized injection current density

The shortest measured gain-switched optical pulse is shown in Figure 3-42. The minimum pulse width achieved is 56 ps and the laser (QDot active material, 770  $\mu\text{m}$  long cavity) was driven at maximum output of 5 V and the electrical pulse duration of 430 ps.

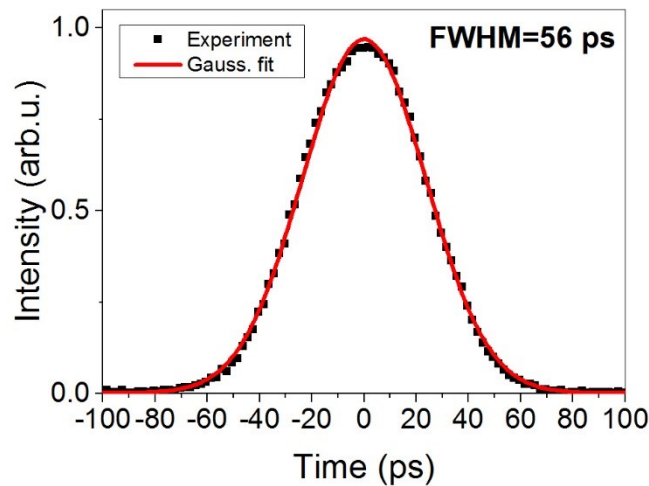


Figure 3-42 Intensity of the gain switched pulse

### 3.5 Conclusion

This chapter provides the first systematic investigation of mode-locking properties of passively mode-locked two-section lasers and single-section mode-locked based on MOVPE-grown QDot

and QDash active material. These lasers are grown using same growing as well as processing techniques, thus it is possible to draw some conclusions on the similarity or differences of their mode-locking properties.

For the first time to our knowledge, we demonstrate ps range ex-facet pulse emission from MOVPE-grown InP/InAs QDot PMLL at ~33 GHz repetition frequency. In general, investigated SSMLL devices demonstrate narrower RF linewidth in ML regime, thus underlining better optical phase noise properties in comparison to PMLL, which is a good in agreement with results of other groups. The ML frequency of QDot and QDash PMML can be tuned in a range of 300–400 MHz, whereas SSMLL allows a factor of 10 lower frequency tunability. Regarding pulse characteristics, we observe significantly lower time-bandwidth product for SSMLL devices and Lorentzian shaped pulse emission, nevertheless SSMLL do not exhibit ex-facet pulse emission and thus are subject to external compression. FROG-measurements reveal the presence of the non-linear chirp component and intensity oscillations on the leading edge of the optical pulses both in QDot and in QDash SSMLL. To summarize, QDot and QDash PMLL demonstrate close ML properties and dynamics, while some difference between ML dynamics is observed between their SSMLL counterparts mainly related to the artifacts of supermodes competition.

The mechanism of pulse generation in SSMLL is not well understood. Thus proper device engineering as a solution to obtain direct ex-facet (i.e. without compression techniques) fs-pulse emission is not yet available, constraining further system implementation of such lasers. QDot and QDash PMLL, however, demonstrate ex facet ps-pulse emission and repetition frequency up to several tens of GHz with better control of output pulse train characteristics at the cost of higher RF-linewidth (i.e. pulse train stability).

We have investigated experimentally the turn-on dynamics of quantum-dot laser. Strongly damped relaxation oscillations and reduced turn-on delay were demonstrated. This is the direct consequence of nonlinear current density dependent carrier scattering dynamics. The pulse generation through gain switching of quantum-dot lasers was studied experimentally resulting in symmetrical Gaussian shaped pulse emission with pulse FWHM of 56 ps. Generation of shorter pulses is also possible with electrical pulse generator with higher output power.

## 4. Four-wave mixing in quantum-dot/quantum dash Fabry-Perot lasers

### 4.1 Introduction

In this chapter, we present the results on external optical injection induced non-degenerate four-wave mixing (NDFWM) phenomenon in nanostructure lasers. Devices under test are Fabry-Perot lasers with quantum-dot (QDot) and quantum-dash (QDash) active medium. Firstly, brief theoretical background of four-wave mixing and injection locking are introduced. We then describe the experimental set-up. In section 4.5.1, 1.55- $\mu\text{m}$  QDot and QDash InP/InAs lasers will be investigated and compared. We will discuss the factors affecting the efficiency of NDFWM and normalized  $\chi^{(3)}$  parameter in these lasers in section 4.5.2. We will determine the main aspects playing role in a large qualitative and quantitative difference of the NDFWM generation in InP/InAs QDot and QDash lasers. Then, in section 4.5.3, we will investigate NDFWM in 1.3- $\mu\text{m}$  QDot GaAs/InAs lasers. Subsequently, we will compare NDFWM characteristics of those devices. In the last section 4.6, a conclusion of the results will be given.

### 4.2 Four-wave mixing in semiconductor lasers and optical amplifiers: theoretical background

Four-wave mixing (FWM) is a non-linear process, which involves the modulation of the refractive index of a medium. Bound electrons respond nonlinearly to an external optical field through high order susceptibility parameter  $\chi^{(2)}$ ,  $\chi^{(3)}$ , ... etc. Generally, the electrical field dependent polarization of material is given by [82]:

$$P(E) = E\chi(E) = \chi^{(1)}E + \chi^{(2)}E^2 + \chi^{(3)}E^3 + \dots \quad (4.1)$$

The  $\chi^{(2)}$  is responsible for second-order effects, e.g. Pockels effect and  $\chi^{(3)}$  for stimulated Brillouin and Raman scattering, and four-wave mixing.

Generally, the fundamental origin of non-linear phenomenon is described by Maxwell equations, wherefrom it can be deduced that:

$$D = E + 4\pi P; \quad (4.2)$$

$$P = \int_{-\infty}^t J(\zeta) d\zeta = P_L + P_{NL} \quad (4.3)$$

Where  $D$  – electric displacement field,  $E$  – electric field,  $P$  – electric dipole polarization,  $J$  – current density. The right term in (2) can be further expanded as follows [83]:

$$P_{NL} = P^{(2)} + P^{(3)} + \dots \quad (4.4)$$

$$P_{FWM}^{(3)} = \chi^{(3)}(\omega_{FWM}, \omega_1, \omega_2, \omega_3) : E(\omega_1)E(\omega_2)E(\omega_3) \quad (4.5)$$

Where  $\chi^{(3)}$  is third order nonlinear susceptibility and  $E_i$  are interacting electrical fields.

High nonlinear properties in the intrinsic amplifying media, low power operation, high energy efficiency and compactness of semiconductor devices excited a great interest as a media for four-wave mixing (FWM) signals generation. Modulation formats transparent wavelength conversion, optical fiber induced dispersion compensation, submillimeter wave generation and optical signal processing are promising applications of this phenomenon [84]–[86].

Non-linearity of semiconductor devices (DFB-, F-P lasers, SOAs) stems from the variation of carrier population (or local carrier density) and depend on their complex dynamics, especially in the case of decreased dimensionality nanostructures based active material where carrier reservoir supplies injected carrier in lasing states of the nanostructures and may act as a source of inertia and entropy effect [87]. The carrier dynamics is then associated with following independent non-linear processes present in the active medium of the semiconductor devices: a carrier density pulsation (CDP), carrier-heating effect (CH) and spectral hole burning (SHB). The beating between the pump and probe waves creates gain and refractive index grating. The reflection efficiency of the grating is firstly given by CDP. CDP dynamics is limited by carrier lifetime in the order of ps; this means that CDP can no longer support FWM at THz-range detuning. However, another non-linear mechanism is responsible for FWM interaction beyond CDP bandwidth and this one is SHB and CH effects. Those are ultrafast intraband effects with sub-picosecond scale characteristic time, making FWM feasible at the detuning frequencies beyond THz [88].

Several analytical models based on single-mode rate equations which consider free-carrier and photon density were proposed for semiconductor lasers and optical amplifiers [89]–[91], from [91] and [92] a simplified formula for FWM-product can be obtained:

$$E_{FWM} = E_p^2 E_q^* \sum_j \frac{\chi_j^{(3)}}{1 - i2\pi f \tau_j} \quad (4.6)$$

$$\chi^{(3)} = \sum_j \chi_j^{(3)} (1 - i2\pi f \tau_j)^{-1} \quad (4.7)$$

Where  $E_{FWM}$ ,  $E_p$  and  $E_q$  are amplitudes of the signal, pump and probe electrical fields,  $f$  – detuning frequency,  $\tau_j$  – relaxation process time constant,  $\chi_j^{(3)}$  – individual contributing non-linear process mentioned above: CDP, CH and SHB. These processes are characterized by different characteristic time  $\tau_j$ , which sets their individual bandwidth and respective frequency response  $|H(f)|$ . The absolute value of vector  $\chi^{(3)}$  depends on the phase relationships of  $\chi_j^{(3)}$  i.e. of corresponding additive CH, CDP or SHB. The phase relationships is given by the linewidth enhancement (or  $\alpha$ -) factor:

$$\chi^{(3)} = \chi_{CH}^{(3)} + \chi_{CDP}^{(3)} + \chi_{SHB}^{(3)} \quad (4.8)$$

Following Eq. 4.5, FWM is evaluated through so-called normalized conversion efficiency  $\eta$  [93]:

$$\eta(f) = \frac{P_{FWM}}{P_{pump}^2 P_{probe}} \sim |H(f)|^2, \quad (4.9)$$

Where  $P_{FWM}$  is the optical power of the probe conversion,  $P_{probe}$  - optical power of the probe wave and  $P_{pump}$  - optical power of the pump signal. On Figure 4-1 the exemplary of non-linear interaction between the pump and negatively detuned (detuning is determined in terms of optical frequency) probe waves is depicted. Consequently, two FWM products are generated: blue-shifted (up-converted) probe-conversion and red-shifted pump-conversion.

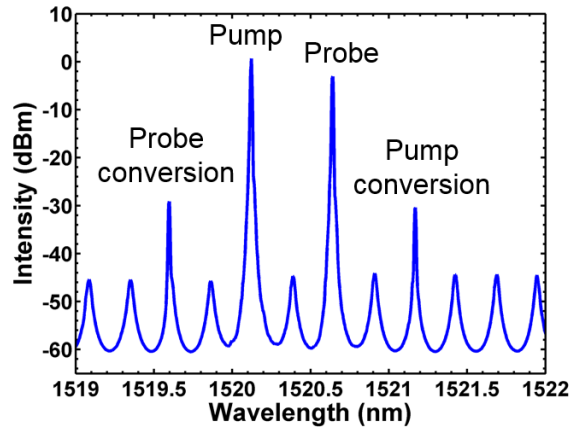


Figure 4-1 Four-wave mixing signal recorded with optical signal analyzer

Conventionally, FWM is obtained in semiconductor optical amplifiers (SOA) whose larger linear gain is an important advantage to generate high power beat-product with possibly weak pump and signal [68], [94], i.e. higher optical signal-to-noise ratio and larger conversion efficiency. However, SOA-approach has following disadvantages: high power consumption, decreased signal-to-noise ratio due to amplified spontaneous emission, low conversion efficiency, and narrow conversion range [95]. Another approach is realized in distributed feedback lasers (DFB), where lasing mode acts as pump [96], thus only one external laser is needed to generate FWM-signal, the enhancement of FWM is obtained by the cavity resonance. Fabry-Perot (F-P) lasers also are able to generate FWM according to several experimental investigation conducted back to early 90's of last century [89], [90], [97], [98]. The results show that FWM in Fabry-Perot (F-P) based method suffers from lower conversion efficiency and succeeded at relatively low frequency detuning of tens of GHz, comparing to SOA and DFB-based counterparts. Nevertheless, the era of nanostructures based light emitters (quantum-dot/quantum-dash lasers) has resumed the interest to this topic due to higher nonlinear gain, ultra-fast carrier dynamics, low ASE and broad gain spectrum of these sort devices [13]. These properties can be advantageous in obtaining larger third-order non-linear susceptibility and hence stable and beyond THz range FWM. Moreover, lower  $\alpha$ -factor inherent to QDot lasers results in constructive interference among contributing CH, CDP or SHB and higher symmetry of conversion, since latter suffers from lower conversion efficiency at negative detuning [92]. In order to improve the conversion efficiency without resorting to a DFB cavity, an optical injection-locking technique is employed to select a mode of the FP laser and use it as pump for the NDFWM. On the other hand, optical injection-locking may decrease the  $\alpha$ -factor, thus

enlarging the total  $\chi^{(3)}$  of the medium, reduce the linewidth, frequency chirp and relative intensity noise [99], [100]. QDash/QDot F-P lasers operating at 1550 nm are of a particular interest both for fundamental investigations of carrier dynamics, which defines the magnitude of intracavity nonlinear interaction, and for practical use as long-haul optical transmission occupy this wavelength region. To our knowledge, studies of FWM in QDash/QDot F-P lasers at 1550 nm lack experimental investigation, thus this chapter addresses this issue.

### 4.3 Optical injection-locking

For efficient FWM inside the laser cavity first optical injection locking of the test laser must be conserved. Optical injection locking (OIL) implies two lasers: the master lasers (MLas) serves as a source of the locking signal for the slave lasers (SL). Usually the slave laser is the laser under test. Often the master laser is a narrow linewidth single mode external-cavity laser with tunable wavelength and output power. In addition to these parameters of the MLas, the polarization also has a large impact on the properties of the injection locking. The output power of the MLas determines the injection ratio: the ratio of the MLas power to the power of the free-running SL (i.e. before optical injection), whereas the wavelengths of the MLas and SL define the detuning – the absolute wavelength offset, which can be positive as well as negative. The measurements in the scope of this chapter are conducted in the stable injection-locking regime, let us further define this term.

Generally speaking, the slave laser may exhibit a large variety of behavior being subjected to external injection: chaotic and bistable behavior, periodic oscillations, stable locking, etc. When the SL is stable locked, the spectrum of SL shrinks to DFB-like single mode emission, usually this is the case when the wavelength of MLas hits exactly the wavelength of one of the FP-modes of a free-running laser. Should slight variation of MLas wavelength may still be tolerable without the breakdown of the stable injection-locking regime, then this wavelength range defines the locking range. The locking range is often broader for larger injection ratio, this effect is illustrated below in Figure 4-2 in so-called bifurcation diagram [101].

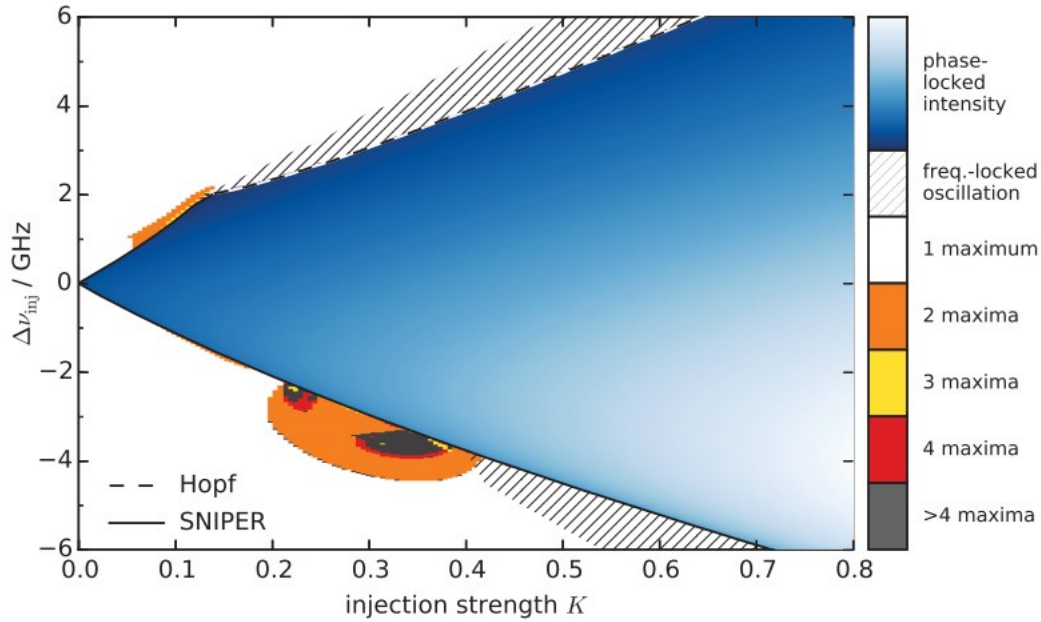


**Figure 4-2 Numerically simulated bifurcation diagram of the quantum-dot laser under OIL [101]**

The blue colored area denotes the area of phase-locked regime, whereas dashed line denotes frequency locking. In phase-locked regime, the phase response of the SL follows arcsine function dependency versus detuning. Other injection-locking scenarios shown in Figure 4-2 are out of the scope of current work.

Optically injected lasers are suitable for several applications, receiver architecture in coherent optical communication system [102]. The phase-locked regime can be used in different optical phase demodulation schemes as shown in [103], other possible applications have already been mentioned in sub-section 4.2.

#### 4.4 Experimental set-up

The experimental setup is illustrated in Figure 4-3 where MLas is used for the external optical injection locking of DUT (device under test) – QDot or QDash laser. Non-degenerate four-wave mixing (NDFWM) is achieved by the mixing between the injection locked emission of the DUT with the probe laser signal. We use the polarization controllers, because the injection locking as well as NDFWM are extremely sensitive to the polarization of the input laser beams.

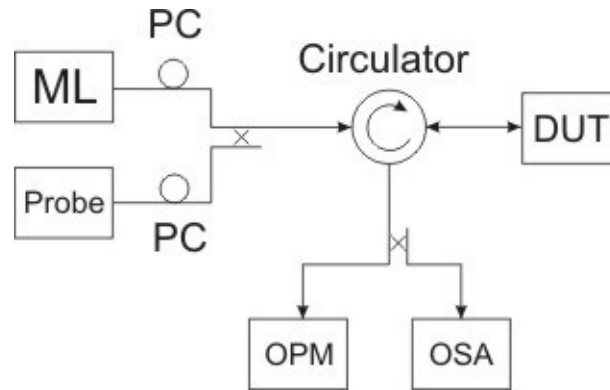


**Figure 4-3 Setup for FWM experiments. ML – master laser, Probe – probe laser, PC – polarisation controller, OPM –optical power meter, OSA – optical spectrum analyzer, DUT – device under test**

Depending on the two degrees of freedom of optical injection, the detuning between the master and slave and the master laser power, the slave F-P laser can either be unaffected by the injection, oscillating in a periodic or aperiodic fashion, or be injection-locked to the master and emit a single mode resonant to the injected signal. In this experiment, the slave lasers are injection-locked using a ratio between the optical power of the master and slave lasers of 1 dB and detunings such that the slave lasers operate well within the injection-locking range.

## 4.5 Experimental investigation

### 4.5.1 InP/InAs quantum-dot and quantum dash lasers

The laser structures investigated here are grown by MOVPE on n-type (001) InP substrate. The active layer consists of 7 stacked QDash (QDot) layers in an  $\text{In}_{0.78}\text{Ga}_{0.22}\text{As}_{0.47}\text{P}_{0.53}$  matrix, enclosed by an  $\text{In}_{0.82}\text{Ga}_{0.18}\text{As}_{0.40}\text{P}_{0.60}$  waveguide. Laterally, single-mode laser buried heterostructures are formed by deep etching through the active region and regrowth of p/n-blocking and contact layers. The temperature of growth and the indium flux rate decide the type of nanostructure (QDot or QDash) formed. Details of material growth, processing and results of material characterization can be found in previous chapter. We investigate here two groups of devices: QDash and QDot lasers with similar cavity lengths around  $750\ \mu\text{m}$  and longer devices with cavities of  $1490\ \mu\text{m}$  and  $1250\ \mu\text{m}$  for the QDash and QDot, respectively. The first group with shorter cavity is only used to compare the maximum achievable FWM efficiency for lasers with the same dimensions. The longer devices, offering a longer interaction length and hence higher FWM efficiency are the main devices studied in this thesis. The ridge width is  $\sim 1\ \mu\text{m}$ , and

no coating is applied to the facets of the devices. The laser bars are mounted on copper blocks for higher thermo-electrical conductivity and fixed on a plate with thermoelectric control. Light-current curves measured at room temperature are shown in Figure 4-4 for both the QDash and QDot devices, showing threshold currents of about 24 mA and 19 mA and slope efficiencies of 19% and 28%, respectively. The turn-on voltage is 0.8V for both devices; the series resistance  $R_s$ , measured at  $2.5I_{thr}$ , is  $5.1 \Omega$  and  $3.7 \Omega$  for the QDash and QDot lasers, respectively.

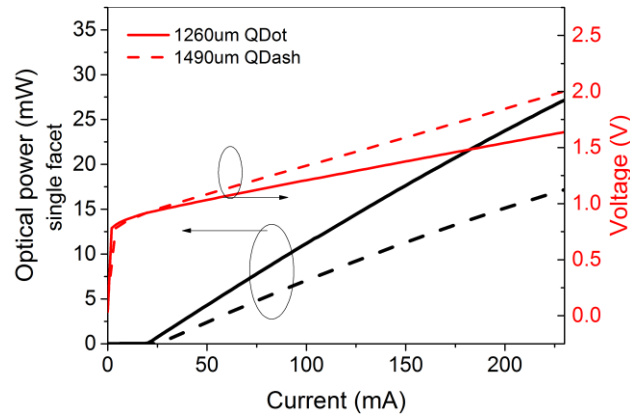


Figure 4-4 LIV-characteristics

Net gain spectra of the devices as a function of current are measured from the spontaneous emission spectra and presented in Figure 4-5. The asymmetry in the net gain profiles is most probably due to slightly lower population of higher energy levels (shorter wavelengths) as well as to the width of the inhomogeneously broadened spectrum, which is of about 40 nm at 23 and 20 mA, respectively, both for QDash and QDot lasers.

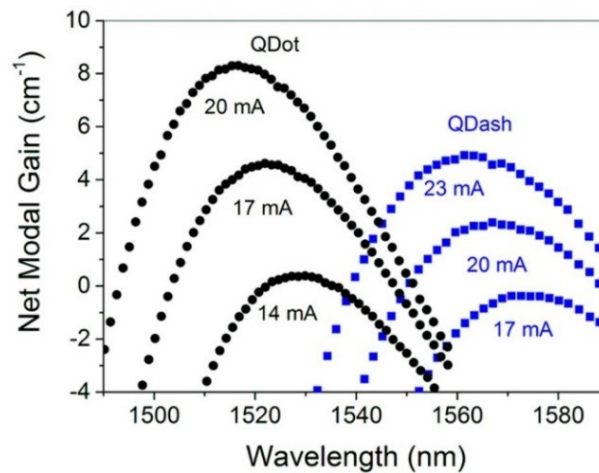
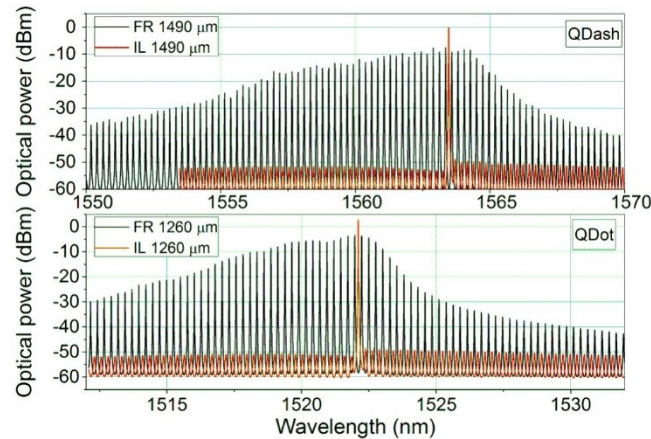


Figure 4-5 Net gain spectra of QDot and QDash lasers below threshold

As mentioned before, the most common way of investigating FWM in semiconductor lasers is based on a pump/probe configuration. In this work, the pump laser is used as a master laser to lock a longitudinal mode at the gain peak of the slave F-P laser. Spectra for both lasers under free running (FR) and injection-locked (IL) operations are shown in Figure 4-6. We note that both free running QDot and QDash lasers show inhomogeneously broadened spectra with FWHM (full-width at half maximum) of  $\sim 3.2$  nm.



**Figure 4-6 Optical spectra of QDash (above) and QDot laser (below) at  $2.5I_{thr}$ : FR-free running laser; IL-injection locked laser.**

The probe signal, with a power 3 dB below that of the free running laser, is then swept from shorter to longer wavelengths around the locked mode. Next Figure 4-7 shows optical spectra for a QDot laser under this dual-injection, with the probe laser tuned to longer wavelengths. The positively detuned FWM-signal is marked as “Probe conversion.”

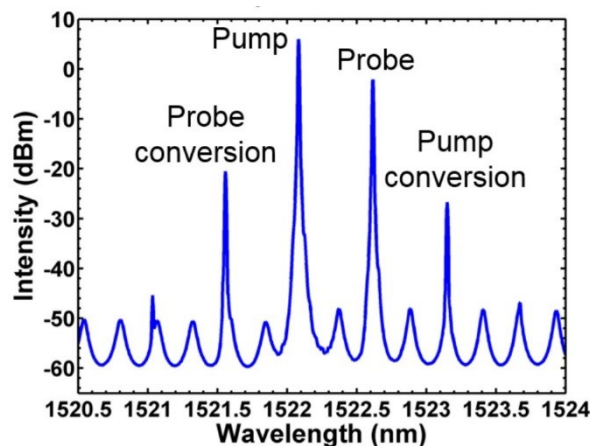


**Figure 4-7 Optical spectra of QDot laser under dual-mode injection at 50mA current**

The FWM conversion efficiency (CE) is defined as:

$$\eta = \frac{Power_{FWM}}{Power_{PROBE}}, \quad (4.9)$$

Where  $Power_{FWM}$  and  $Power_{PROBE}$  are the power in mW of probe conversion and probe signals respectively.

#### 4.5.2 Discussion

CE in logarithmic scale along with optical signal-to-noise ratio (OSNR) results are shown in Figure 4-8. A maximum CE of -10.7 dB is measured for the QDash laser, being 9 dB larger than the QDot. The QDash device also demonstrates a broader frequency detuning range from -1.2 to 2.7 THz. Owing to the optical injection, very large OSNRs of 37 dB at 27 GHz and 22 dB at 67 GHz detuning are measured for QDash and QDot lasers, respectively. Remarkably, it is very important to stress that these values are comparable with those measured for more complex DFB-laser structures [96], bulk and QDash/QDot SOA's [94], [104], and larger than values previously reported for InAs/InP QDot lasers [105], [106]. The larger CE is observed for both devices at positive detuning ( $\lambda_{pump} < \lambda_{probe}$ ), we attribute it to the asymmetric gain profiles (Figure 4-5) and the wavelength dependency of the alpha factor (Figure 4-9).

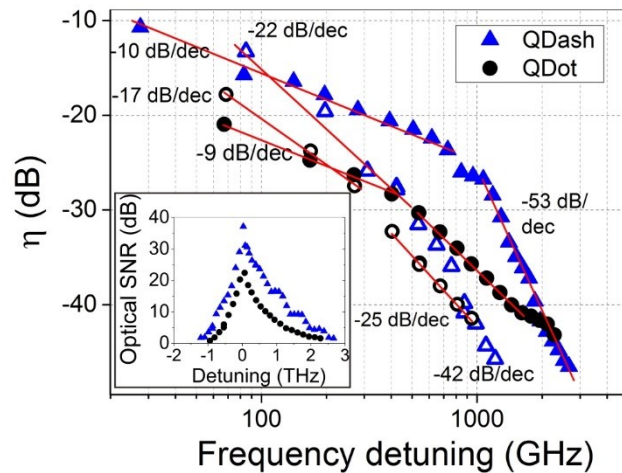


Figure 4-8 Conversion efficiency (solid/empty scatter–positive/negative detuning, respectively) and optical SNR (inset).

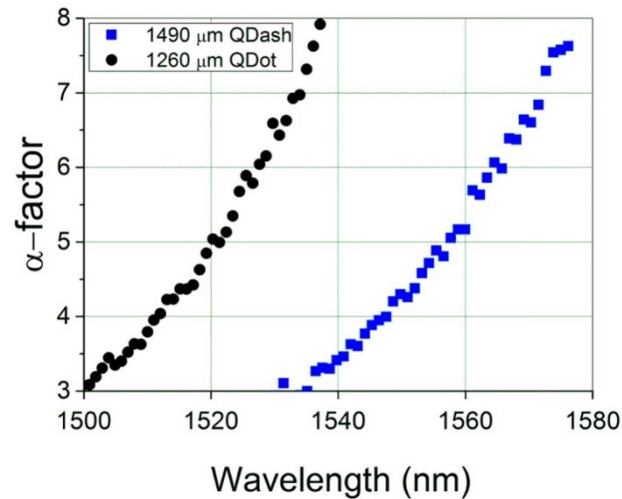


Figure 4-9 Dependency of the  $\alpha$ -factor on wavelength for QDot and QDash lasers.

For detunings above 400 GHz, the larger alpha factor measured for QDash lasers leads to a difference of  $\sim 10$  dB between “positive” and “negative” CE while the latter is reduced down to 5 dB for QDot lasers, owing to the reduced phase-amplitude coupling. The CE found for positively detuned QDash lasers resembles the results already published for QDash SOAs [107]. Two regions are distinguished: a first decrease in 10 dB/decade, followed by a faster decrease in 53 dB/decade. The first region has a picosecond characteristic time, controlled by an efficient interband carrier-density pulsation (CDP) process [88]. The rapid decrease with 53 dB/decade starting at 1 THz represents the joint, but de-phased effects of different dynamic processes: CDP, carrier heating and spectral hole burning [108] with a sub-picosecond characteristic time. Qualitatively, this behavior is also similar for QDot lasers, which show a lower conversion efficiency most likely due to the phonon bottleneck combined to the lower modulation amplitude of carrier population arising from a reduced number of active states. The former is known to restrain the coupling of carriers between spatially isolated quantum dots and the surrounding material with large energy spacing [19]. However, in case of QDashes, the carriers are captured from the bulk or QW (quantum well) surrounding areas into the numerous overlapping states with the same transition energies of the dash DOS function [19]. Two-photon absorption phenomenon (TPA) may also be decisive since the latter was proved to stimulate ultra-fast gain recovery in QDash SOAs at energies above and below the pump [109]. The flattening of the CE-curve observed for a positively detuned probe around 1 THz in the case of the QDash device may actually result from this phenomenon. Thus, the QDash DOS, which consists of many overlapping inhomogeneously broadened states with high energy tail, may favor additional gain at the FWM-signal wavelengths and leads to a larger FWM-conversion efficiency [110].

Although a higher FWM efficiency is naturally expected from a longer interaction length [94], it is important to stress that OSNR and CE of devices with cavity length of 750  $\mu\text{m}$  are, respectively, found to be 12 and 5.2 dB larger for QDash lasers compared to QDot.

The conversion efficiency for both QDash and QDot devices remains below -55 dBm and nearly equal for large positive  $f > 2$  THz and negative  $f > 1$  THz detuning (Figure 4-8). This indicates that pump-probe detuning exceeds the bandwidth where the conversion is both fast and effective. In this region, QDash lasers demonstrate a rapid decrease of 53 dB/decade, whereas QDot rolls off at 21 dB/decade. The low CE in this detuning region can be attributed to the smaller number of QDashes/QDots occupied by carrier, since the density of nanostructures in these wavelength regions of the gain spectra is lower. To this end, the abrupt gain spectra profile can explain the equalization of QDash and QDot CE at lower negative detuning. Finally, carrier dynamics in quantum dashes also may suffer from a phonon bottleneck when the energy spacing is large. The third-order optical susceptibility normalized to optical linear gain  $\chi^{(3)}/g_0$  is calculated using the formula from Ref. [111] and assuming an effective mode area of 1.3  $\mu\text{m}^2$ ,

$$\eta = \left| \frac{3k_0}{4n} \Gamma \chi^{(3)} \frac{\exp(\frac{\Gamma g L}{2}) - 1}{\Gamma g} \right|^2 \quad (10)$$

The resulting dependence of  $\chi^{(3)}/g_0$  on the detuning is shown in Figure 4-10. The value of  $\chi^{(3)}/g_0$  decreases from  $4 \times 10^{-19} \text{ m}^3/\text{V}^3$  down to  $6.0 \times 10^{-21} \text{ m}^3/\text{V}^3$  in the 0.027–2.66 THz detuning range for QDash lasers and from  $9.4 \times 10^{-20} \text{ m}^3/\text{V}^3$  to  $5.1 \times 10^{-21} \text{ m}^3/\text{V}^3$  in 0.068–2.270 THz range for QDot lasers.

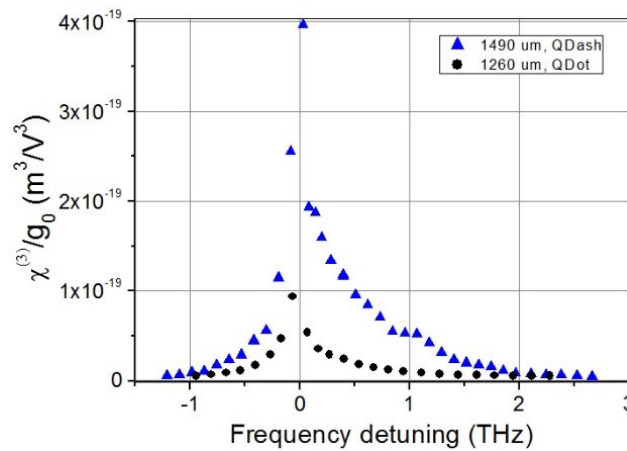


Figure 4-10 Evaluation of third-order normalized optical susceptibility

Remarkably, the  $\chi^{(3)}/g_0$  value for the QDash gain medium is larger than the one measured for DFB lasers [111] and references therein.

### 4.5.3 InAs/GaAs quantum-dot lasers

We now investigate 1.3  $\mu\text{m}$  GaAs/InAs QDot lasers, as a second part of our research on NDFWM in nanostructure lasers. The epi-structure of the lasers is as follows. MLL AlGaAs/GaAs separate confined hetero-structure includes 10 stacks of InGaAs/GaAs of QDot layers. Each QDot layer is overgrown with an InGaAs quantum well (dot-in-a-well structure), in order to shift the emission wavelength to 1.3  $\mu\text{m}$ . 2- $\mu\text{m}$ - and 4- $\mu\text{m}$ -wide ridge waveguides are defined by dry etching through the active region. The structure is isolated and planarized using benzocyclobutene. Then the electrical n- and p-top-side contacts are realized for needle-probe head contacting. Finally, the wafer is thinned. The cavity length of the lasers is 1.5 mm long, and the facets are left as cleaved. The static characteristics of 2- and 4- $\mu\text{m}$  ridge lasers is shown in the Figure 4-11(a). The lasers exhibit a threshold current of 29 and 36 mA; slope efficiency is 18% and 27% for 2- $\mu\text{m}$  and 4- $\mu\text{m}$  ridge devices respectively. The turn-on voltage is equal to 0.9 V for both devices. The net gain profile is plotted in Figure 4-11(b) at different bias current below threshold. One can clearly see that the symmetry in the gain spectrum is more pronounced in comparison to quantum-dot/dash investigated in the previous section. This may witness more uniform size distribution of MBE-grown QDot material.

NDFWM conversion efficiency are illustrated on Figure 4-11(c) and (d) for 2- $\mu\text{m}$  and 4- $\mu\text{m}$  ridge laser respectively. Negatively detuned wave is still subject to lower conversion for both lasers, as in the case with 1.55- $\mu\text{m}$  InP/InAs devices, yet the difference is considerably smaller due to a slight asymmetry in gain profile and low alpha-factor. The conversion efficiency curve undergoes two regimes for both GaAs-lasers: first, the slow initial decrease of -15/-16 (2- $\mu\text{m}$  ridge laser) and -12/-13 (4- $\mu\text{m}$  ridge laser) dB/decade with picosecond characteristic time representing deep and efficient CDP. Beginning from  $\sim 1$  THz conversion efficiency rolls off at -35/-38 and -29/-42 dB/decade for 2- $\mu\text{m}$  and 4- $\mu\text{m}$  ridge laser respectively, indicating dephased contribution of SHB and CH. GaAs-devices demonstrate moderate decrease in comparison to QDash devices with fastest decrease of -53 dB/decade. Such a difference may also originate from larger alpha-factor measured for QDash counterpart, representing stronger phase decorrelation between CDP, SHB and CH. 4- $\mu\text{m}$  ridge lasers demonstrates better NDFWM performance as compared to 2- $\mu\text{m}$  ridge devices, which is probably due to a broader interaction cross-section between mode area and active material, better symmetry of conversion lower

alpha-factor [112]. Further comparison of 1.55- $\mu\text{m}$  InP/InAs and 1.3- $\mu\text{m}$  GaAs/InAs lasers NDFWM properties will require sophisticated consideration of material composition, epitaxial growth parameters and the morphology of quantum-dot/dash since they affect the underlying energy structure. However this topic is outside of the scope of current investigation and can be used in future work.

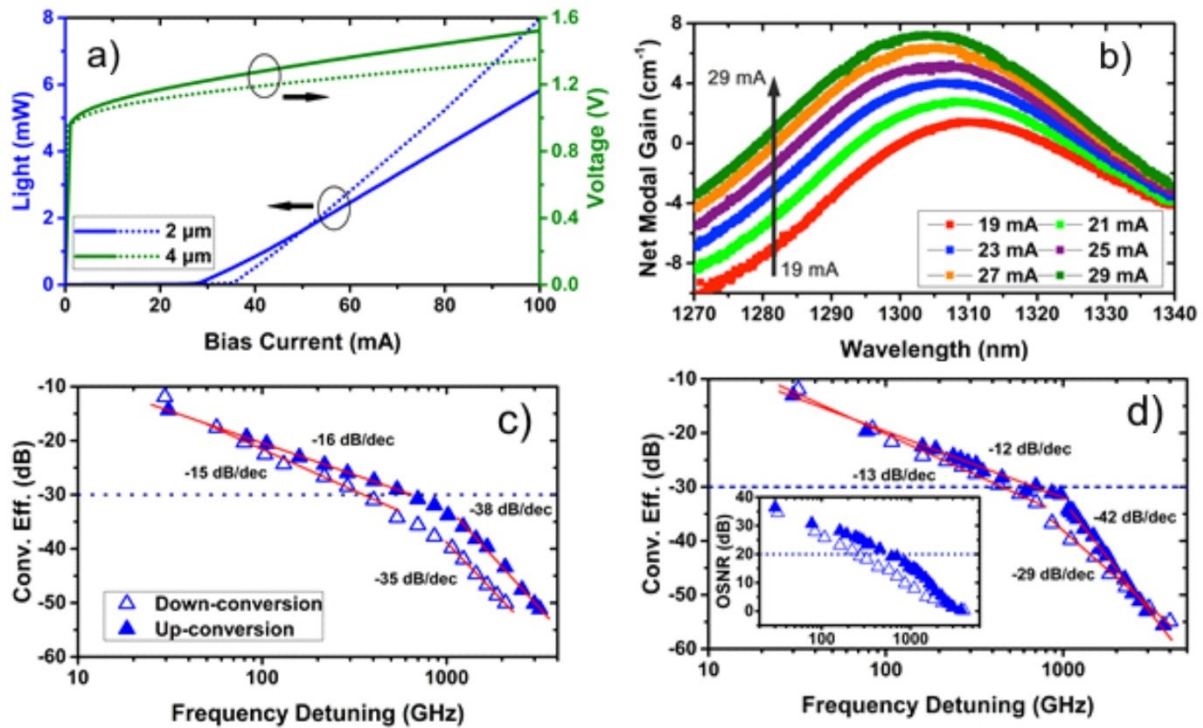


Figure 4-11 GaAs quantum-dot laser static characteristics (a); net gain spectrum at different current of 2- $\mu\text{m}$  ridge laser (b); conversion efficiency of 2- $\mu\text{m}$  ridge laser (c); conversion efficiency (inset: OSNR) of 4- $\mu\text{m}$  ridge laser (d) [112].

#### 4.6 Conclusion

We have observed a unique and large normalized conversion efficiency of -18.6 dB, OSNR of 37 dB, and a conversion achievable for frequency detunings up to 3 THz in MOVPE-grown 1490  $\mu\text{m}$ -long InP/InAs quantum-dash lasers operating at 1550 nm under dual-mode optical injection. These values are the highest reported for F-P lasers and comparable to ones reported for DFB-lasers and SOAs, more complex to process. We observe a larger conversion efficiency for 1490  $\mu\text{m}$ -long QDash devices in comparison to 1250  $\mu\text{m}$ -long QDot lasers, fabricated by the same growth and processing techniques. QDot devices with delta-function DOS show a four times lower third-order optical susceptibility, a 12 dB-lower normalized conversion efficiency

and 14.7 dB-lower optical signal-to-noise ratio. The analysis confirms that such a difference is not only due to the cavity length but also to additive contributions to the gain such as TPA, faster gain saturation, and enhanced modulation of carrier populations. The polarization of the master and probe external lasers were adjusted separately by means of polarization controllers to obtain high efficient FWM.

We investigated a highly efficient wavelength conversion in optically injected MBE-grown InAs/GaAs quantum-dot FP lasers with 1.5-mm cavity length. We have shown a maximum conversion of -12 dB and a conversion bandwidth as large as  $\sim 4$  THz. We have found that devices with the ridge width of 4  $\mu\text{m}$  demonstrate more efficient and symmetrical wavelength conversion as compared to 2  $\mu\text{m}$  lasers.

Our results unveil which structural approach must be followed in realization of lasers for efficient NDFWM based wavelength conversion.

## 5. Directly modulated InP/InAs nanostructure lasers for data transmission

The global Internet traffic has been growing exponentially since decades and will continue to grow as predicted in [113]. The enormous amount of IP-traffic is handled in optical networks thanks to their superb capacity therefore many research groups worldwide are making a huge effort to develop the characteristics of optical communication systems to meet the growing demands of data transmission market. Semiconductor lasers are key components for optical communication systems and the serious challenges here are the temperature stability, large optical gain, low threshold current and modulation bandwidth in addition to the selection of mass production oriented growth technology. Significant improvements of the semiconductor laser performance have been achieved in last decades, thanks to implementing zero-dimensional (quantum dot) structures into the active layer [6], [114]. These types of devices benefit of high differential gain due to delta function like density of states making them very attractive for direct modulation. Direct modulation is a way to convert an electrical data signal imposed on bias current into an optical data signal. This is possible because laser output power depends on the amount of injected carriers. Direct modulation is used e.g. in on/off keying (OOK) modulation format, which is cost-effective solution for applications with medium data rate demands, e.g. 100GbE 4x25G, OTU4 4x28G and SONET (synchronous optical network) networks.

The fastest MOCVD (Metalorganic Chemical Vapor Deposition) grown GaAs-based quantum-dot lasers operating at 1.31  $\mu\text{m}$  demonstrate -3-dB modulation bandwidth of 12 GHz [115]. Driving a GaAs-based laser on excited state may push the modulation speed up to 16.25 GHz [116]. By employing tunneling injection and p-doping for hot-carrier effect minimization, modulation bandwidth can be increased to 14.4 GHz as was demonstrated in MBE grown InP-based quantum-dot lasers operating at 1.55  $\mu\text{m}$  [53]. Quantum dash based gain media properties are similar to those of quantum dots, both exhibiting inhomogeneously broadened gain spectrum and complex carrier transport dynamics. However, quantum dash medium's energy band structure has a quantum-wire like nature in the contrast to delta-like of quantum dot material. This fact influences the carrier dynamics, because the ratio between the number of states in the carries reservoir and quantum dot/dash ensemble determines a carrier capture rate and state filling factor [19], thus affecting the differential gain, which defines the D-factor and modulation bandwidth. The increase of the differential gain does not necessarily lead to a higher modulation

bandwidth [117], as the latter is the result of an interplay between the differential gain and gain compression, given by their ratio. Other important factors affecting the modulation bandwidth inherent to quantum dot and quantum dash gain medium are homogeneous and inhomogeneous broadening. The impact of inhomogeneous broadening consists in non-equilibrium carrier distribution between lasing and non-lasing quantum dots. This results in carrier escape and re-capture from the non-lasing into lasing quantum dot, which can limit the modulation speed. Phenomenologically, homogeneous and inhomogeneous broadening affect the optical gain [118], and the latter impacts the laser's carrier dynamics and modulation bandwidth. Ground-state filling and off-resonance states filling are also found to decrease the differential gain of quantum-dot active material [18].

In this chapter in section 5.1 we will at first present theoretical background on small-signal operation of semiconductor laser based on rate equations. We will then present experimental results of short cavity quantum-dot lasers small-signal measurements and will look at their characteristics. Then we will experimentally investigate small-signal responses of short cavity quantum-dash lasers. Subsequently, we will describe and explain their features of small-signal operation. In the discussion section will give a consistent comparison of quantum-dot and quantum-dash lasers dynamics based on  $D$ - and  $K$ -factor, relaxation resonance frequency and -3 dB bandwidth.

Then in section 5.2 results of large-signal measurements with quantum-dot and quantum-dash lasers will be presented. OOK with non-return-to-zero (NRZ) pseudo-random binary sequence will be used for directly modulated devices.

In the last section 5.3 we will give a conclusion of the results demonstrated in this chapter.

## **5.1 Small-signal modulation**

In this sub-section, we investigate and determine the impact of the nanostructure dimensionality on the small-signal modulation response. The objective of this study is to reveal the characteristics of the modulation transfer function depending on the bias current and type of active material; also, the effects that limit small-signal performance will be discussed. The theoretical background of laser's small-signal operation is based on rate equations, taken with several simplifications [119]. The rate equations relate the photon density in a cavity  $P$  to the

density of carrier injection  $N$  taking in account carrier lifetime  $\tau_c$  and photon lifetime  $\tau_p$ , material gain  $g_m$  and spontaneous emission rate  $R_{sp}$ :

$$\frac{dN}{dt} = \frac{I}{e} - \frac{N}{\tau_c} - \Gamma v_g g_m \quad (5.1)$$

$$\frac{dP}{dt} = \Gamma v_g g_m P - \frac{P}{\tau_p} - R_{sp} \quad (5.2)$$

where  $I$  is the injection current,  $\Gamma$ – optical confinement factor,  $v_g$  is the group velocity.

Small-signal modulation implies a sinusoidal modulation  $\Delta I$  of bias current resulting in both the variation of injected carriers  $\Delta N$  and of photon density  $\Delta P$ :

$$I(t) = I_b + \Delta I(t) \quad (5.3)$$

$$N(t) = N_b + \Delta N(t) \quad (5.4)$$

$$P(t) = P_b + \Delta P(t) \quad (5.5)$$

Where  $\Delta I$ ,  $\Delta N$  and  $\Delta P$  can be expressed as:

$$\Delta I(t) = I_1 e^{i\omega t} \quad (5.6)$$

$$\Delta N(t) = N_1 e^{i\omega t} \quad (5.7)$$

$$\Delta N_p(t) = N_{p1} e^{i\omega t} \quad (5.8)$$

Taking differential of Eq.5.3 and re-arrangement using Eq.5.1-5.2, one can obtain after simplifications, solving for  $N_1$  and  $N_{p1}$ :

$$N_1 = \frac{\eta_i I_1 \gamma_{pp} + j\omega}{qV \omega_r^2} \cdot H(\omega) \quad (5.9)$$

$$N_{p1} = \frac{\eta_i I_1 \gamma_{pn}}{qV \omega_r^2} \cdot H(\omega) \quad (5.10)$$

Where  $H(\omega)$  is modulation transfer function:

$$H(\omega) = \frac{\omega_r^2}{\omega_r^2 - \omega^2 + \gamma j\omega} \quad (5.11)$$

Where  $\omega_r$  and  $\gamma$  are defined as resonance frequency and damping factor respectively. The resonance peak exists due to the relaxation oscillation process. As can be seen from Eq.5.11 the transfer function has a frequency response of a second-order low pass filter with a damped resonance and depends on the injection current dependent resonance oscillation frequency and damping factor ( $s^{-1}$ ):

$$f_r = D\sqrt{I - I_{thr}} \quad (5.12)$$

$$\gamma = Kf_r^2 + \gamma_0 \quad (5.13)$$

The damping factor  $\gamma$  shows the rate of the intracavity energy loss, resulting in the reduction of resonance peak intensity. It is proportional to the square value of the relaxation frequency linearly with the proportionality  $K$ -factor (s).  $\gamma_0$  is the damping offset, i.e. the damping at low modulation frequency. The  $D$ -factor ( $\text{GHz}/\text{mA}^{1/2}$ ) determines the dependence of the relaxation frequency on the injection current and shows the rate of relaxation oscillation frequency increase with current. Large  $D$ -factor is always favorable and implies that a laser exhibits a large relaxation oscillation frequency that can be reached at lower values of injection current. Consequently,  $D$ -factor indicates the ability for a larger modulation bandwidth at lower bias.

The  $K$ - and  $D$ -factor can be further respectively expanded as:

$$K = 4\pi^2 \left( \tau_p + \frac{\varepsilon}{v_g \frac{dg}{dN}} \right) \quad (5.14)$$

$$D = \frac{\omega_r}{2\pi} = \frac{1}{2\pi} \sqrt{\frac{\eta_i \Gamma v_g}{qV_a} \frac{dg}{dN}} \quad (5.15)$$

where  $dg/dN$  is the differential gain,  $\varepsilon$ -gain compression factor. -3-dB modulation bandwidth  $f_{-3dB}$  is defined as:

$$\left| \frac{H(f_{-3dB})}{H(0)} \right|^2 = 0.5 \quad (5.16)$$

Equations 12-15 define the intrinsic dynamical properties of a laser and reveal that large modulation bandwidth is a compromise between the photon lifetime and carrier capture/relaxation time [120]. However, such extrinsic properties as electrical parasitics and device heating can impose severe limitations on the dynamics, and therefore must be considered.

Consequently, a second term is introduced into Eq. (5.11), which represents a single-pole low-pass filter with a cut-off frequency  $f_p$ :

$$H(\omega) = H_i(\omega)H_p(\omega) = \frac{\omega_r^2}{\omega_r^2 - \omega^2 + \gamma j\omega} \cdot \frac{1}{1 + j\frac{\omega}{\omega_p}} \quad (5.17)$$

According to Eq. (5.17), the modulation response is a three-pole function, and defines dynamical properties of a laser in terms of damping factor, relaxation and parasitic cut-off frequency. Accordingly, increase of differential gain, reduction of heating effects and electrical parasitics will improve high-speed performance of a device. The differential gain in bulk active material implies any perturbation of carrier density directly transferred in the gain change. However, in quantum-dot and dash active media carriers are fed from a carrier reservoir. Therefore, a carrier density variation cannot directly affect the population of quantum dots and dashes but firstly the carrier reservoir population is perturbed. The latter has a finite number of populated energy states, which contribute partially into lasing, thus carrier density modulation is firstly redistributed among them and then transferred on the population alteration of nanostructures via capture and relaxation process [18]. Quantum dots size distribution results in inhomogeneously broadened gain spectrum, where lasing and non-lasing states are localized. The non-lasing quantum dots have slow response time negatively affecting the carrier scattering dynamics along with slow reservoir transport between lasing and non-lasing quantum dots (because the electron exchange between lasing and non-lasing dots occurs through the carrier reservoir) [121].

Measurements of small-signal modulation response  $S_{21}$  are conducted using a vector network analyzer (HP8722C) and fast photodetector with 40 GHz cut-off frequency under CW bias conditions. For  $S_{21}$  and frequency response function  $H(\omega)$  following relation holds:

$$S_{21} = 20 \log |H(\omega)| \quad (5.18)$$

The laser's frequency response is bias dependent, therefore small amplitude frequency swept signal was applied at various injection current. Usually at low bias currents, the relaxation oscillation peak is more pronounced, meaning that the damping is weak. With increased injection current relaxation oscillation frequency increases, as well as the damping. At high bias the regime of overdamped oscillations is reached, where resonance frequency starts to decrease, resulting in the saturation and reduction of the modulation bandwidth. Thus, trade-off exists

between the damping and the resonance frequency. S21-parameter was measured for identical in terms of the cavity length and ridge width quantum-dot and quantum-dash lasers.

### 5.1.1 Quantum-dot lasers small-signal analysis

S21-parameter parameter was measured as a function of bias current. The lasers were 440  $\mu\text{m}$  long and had a ridge width of 1.4  $\mu\text{m}$  and as cleaved facets. The laser bar was mounted on the copper block installed on temperature controlled contact plate. The static characteristics are derived from LIV-curve shown in Figure 5-1 measured at the room temperature. The threshold current is 12 mA, slope and external quantum efficiency are 0.21 and 26% respectively, the turn-on voltage is equal to 0.83 V. At two-times threshold current the differential diode resistance is  $\sim 8$  Ohm. The optical spectrum of this device is inhomogeneously broadened, 1510 nm is the peak wavelength at  $10I_{\text{thr}}$ . The wavelength red shift amounts to  $\sim 0.09$  nm/mA when bias is increased from 60 to 120 mA, that is two times larger than red shift measured at 16-40 mA, indicating moderate gain saturation.

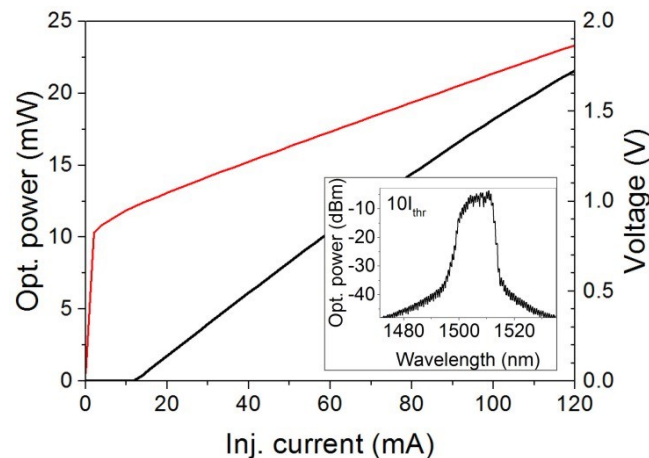


Figure 5-1 LIV-curve and optical spectrum (inset) of QDot laser

High-frequency needle probes were used for dynamical characterization of the lasers. Strongly damped and bias dependent small-signal modulation response are shown in Figure 5-2. Increased damping and shift of relaxation oscillation peak are observed at increased bias currents. A strong damping of relaxation oscillations results from several nonlinear processes: spectral hole burning, hot carriers effect, cavity standing wave effect, coupling of spontaneous emission into lasing mode [122]. The gain compression factor  $\epsilon$  introduced in Eq. 15 accounts for these effects.

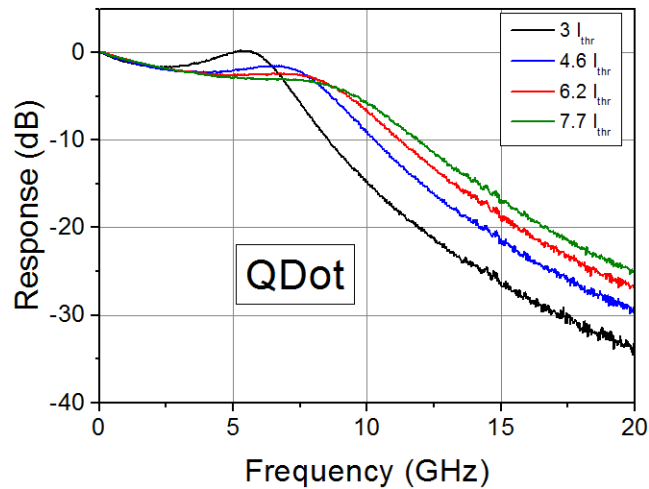
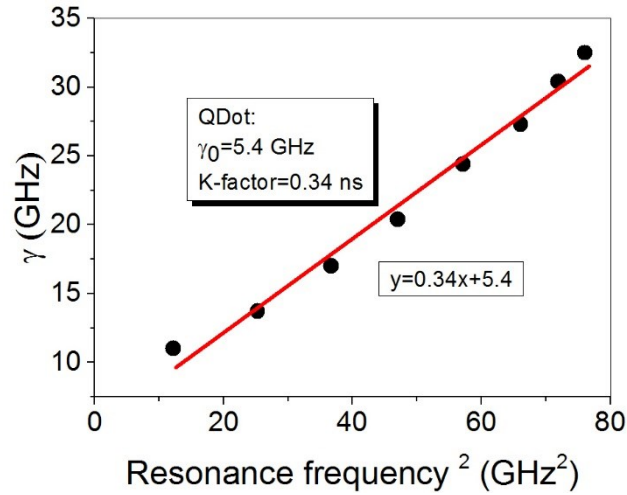


Figure 5-2 Small-signal modulation response S21 of QDot laser at various bias currents

The frequency response of QDot laser is limited by parasitic time constant (given by the resistance and capacity) and nonlinear gain compression factor. The low frequency roll-off has been reported before e.g. in [123], [124] and has been addressed to enhanced non-linear scattering and an injection bottleneck [19]. As outlined in [19] such a carrier transport delay is related to the increased carrier capture time from a carrier reservoir into the lasing states of the dots owing to the large energy separation between the reservoir and lasing states of the dots, so a direct transport of the carriers is unlikely. According to [117], owing to different effective mass, sub-band electron level separation is larger than that of the holes and phonon energy. For this reason holes thermalize quickly into ground states, whereas electrons experience mixed (electron-multiphonon, electron-hole) scattering scenario characterized by longer relaxation times. Consequently, carriers are captured into quantum dots with higher ground state levels and then relax inside inhomogeneously broadened spectrum into lasing states of the dots. Ground state filling and off-resonance states filling are also found to decrease the differential gain of quantum-dot active material [18]. The difference in the spectral density of quantum states between the carrier reservoir and the zero-dimensional quantum dot plays also a significant role, a large difference causes an entropy effect which leads to a strong temperature dependent dynamics and decreased modulation bandwidth [87].

The resonant frequency and damping factor were extracted from curves (Figure 5-2) using response function subtraction method proposed in [125]. The damping rate vs squared relaxation oscillation frequency along with the linear fitting are shown in Figure 5-3.



**Figure 5-3 Damping rate vs squared relaxation oscillation frequency**

The damping offset  $\gamma_0$  and  $K$ -factor are extracted from Figure 5-3, and amount to 5.4 GHz and 0.34 ns respectively. The  $K$ -factor can determine the maximum possible intrinsic modulation bandwidth:  $f_{\max} = 9/K$  ( $\sim 26$  GHz for this particular case), which is decreased in real devices due to parasitics and heating. However this approximation fails in the presence of carrier transport effects and thus can be used only as indicative parameter of a laser [126]. The damping offset  $\gamma_0$  corresponds to the recombination time of 0.16 ns, this value typical for similar laser structures based on the active material with reduced dimensionality [22]. The increase of the resonance frequency squared as a function of injection current is shown in Figure 5-4. The slope amounts to 1.1 GHz<sup>2</sup>/mA resulting in the modulation efficiency  $D$ -factor of 1.05 GHz<sup>1/2</sup>. The validity of S21-measurements is proven by the linear fit function, starting clearly from the coordinates' origin. The intrinsic resonance frequency reaches 8.1 GHz at 70 mA ( $\sim 5.5I_{\text{thr}}$ ). The inset of Figure 5-4 shows the -3-dB modulation bandwidth of quantum-dot laser versus injection current, the curve represents clearly the limitation of the modulation bandwidth and its saturation effect with increased bias. The maximum value of 8.1 GHz is achieved, being comparable even with InP/InAs quantum-dot lasers with direct-modulation optimized structures [124]. The bandwidth of the device is the result of an interplay between the differential gain and the gain compression [117]. As noticed before, these parameters depend on carrier capture time, state filling and electron transport through the carrier reservoir. In particular, the state filling manifests itself in a moderate gain saturation effect mentioned above (Figure 5-1). The gain saturation is also the reason for the modulation bandwidth limitation [115]. Further, we present the results of small-signal modulation measurements for quantum-dash lasers.

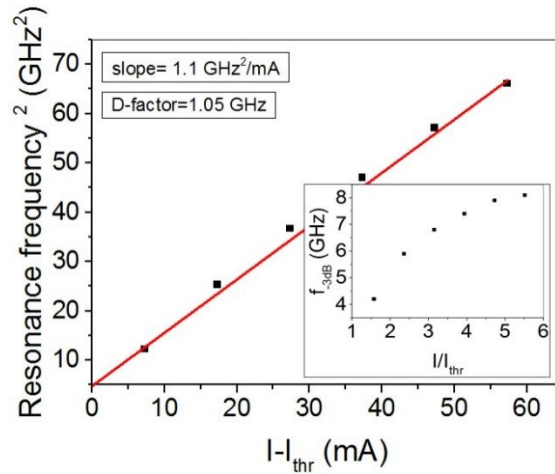


Figure 5-4 Square of resonance frequency (with -3-dB bandwidth in the inset) versus bias

### 5.1.2 Quantum-dash lasers small-signal analysis.

The static characteristics of 420  $\mu\text{m}$  long quantum-dash laser are described in Figure 5-5. The slope efficiency is 0.21 W/A and the differential external quantum efficiency is 26% assuming single facet emission. The threshold current is 10.6 mA, the turn on voltage equals to 0.81 V and the series resistance 7.7 Ohm. The spectral properties exhibit stable ground state emission similar to quantum-dot devices. The static characteristics of the device are very close to those of quantum-dot laser described above.

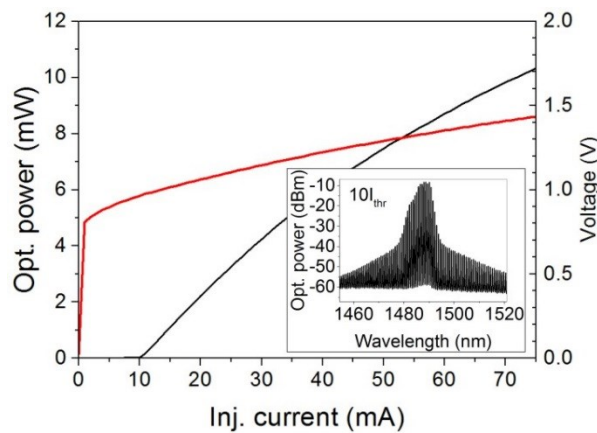
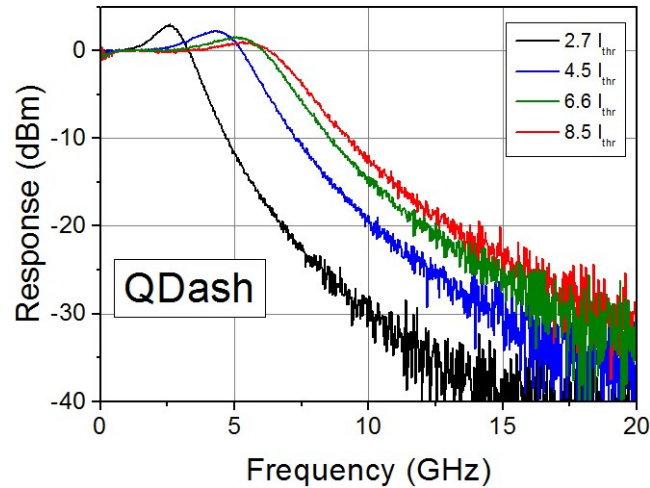


Figure 5-5 LIV-curve and optical spectrum (inset) of QDash laser

The damped bias dependent small-signal modulation responses are shown in Figure 5-6. The relaxation oscillation resonance peak increases with increased injection current. The peak damping also follows well-known increment behavior. It should be noted, however, that the peak damping is significantly lower also no low frequency roll-off is observed here in comparison to

the responses of quantum-dot lasers presented in Figure 5-2. Lower damping corresponds to lower gain compression, whereas the frequency roll-off implies carrier transport bottleneck. The detailed explanation of these discrepancies will be given in the discussion subsection.



**Figure 5-6 Small-signal modulation response S21 of QDash laser at various bias currents**

The damping rate vs squared relaxation oscillation frequency along with the linear fitting are shown in Figure 5-7. In general, the characteristic follows the linear trend and the damping rate increases with increasing relaxation frequency. However, the slope of the plot increases at 40-50 GHz<sup>2</sup>, which implies the increase of the  $K$ -factor (due to the heating at high bias levels, decrease of differential gain and increased gain compression) and shows a saturation effect for the values beyond 50 GHz<sup>2</sup>. The damping is low at small bias level, which corresponds to low relaxation frequency (Eq. 14). Extracted damping offset  $\gamma_0$  amounts to 8.2 GHz, which corresponds to carrier lifetime of 0.12 ns and the  $K$ -factor equals to 0.29 ns.

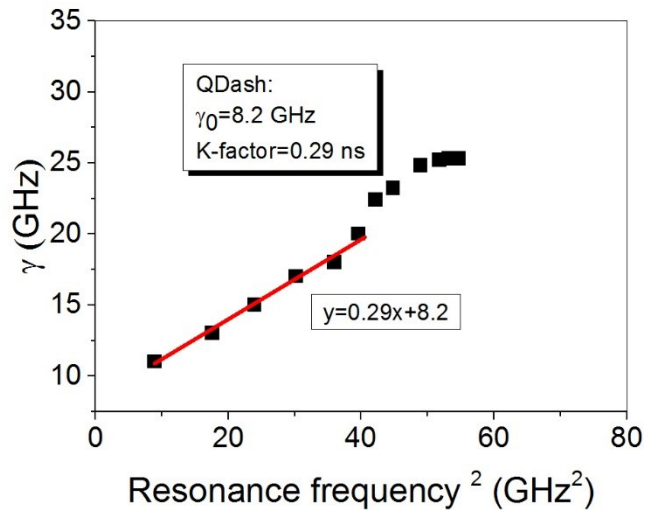


Figure 5-7 QDash laser damping rate vs squared relaxation oscillation frequency

The values of relaxation frequency square as a function of bias above threshold are shown in Figure 5-8. The saturation of relaxation frequency at high injection levels is probably due to the gain saturation as was pointed out in [115]. The linear fit considers only frequency values before the saturation resulting in extracted  $D$ -factor of  $0.75 \text{ GHz}^{1/2}$ . The inset of Figure 5-8 represents the modulation bandwidth versus bias level, the saturation is clearly observed. The breakdown of the linear behavior at high bias currents in Figure 5-7 complies with the saturation of squared RO frequency in Figure 5-8 and -3-dB bandwidth (inset of Figure 5-8). This phenomenon is suggested as being caused by enhanced carrier escape from upper energy states.

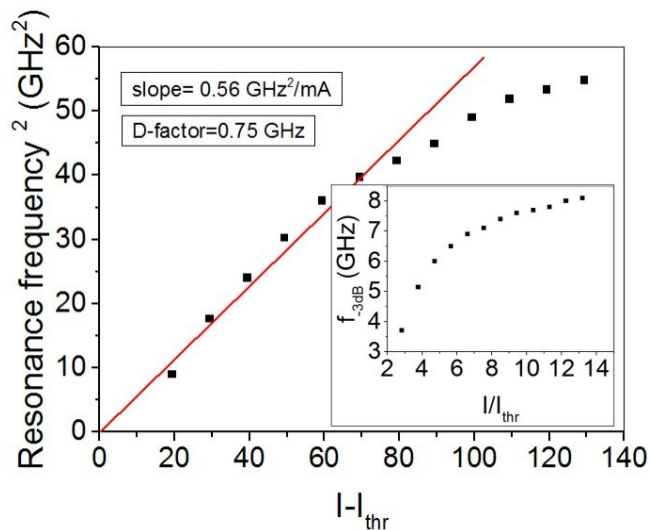


Figure 5-8 QDash laser's square of relaxation resonance frequency (with -3 dB bandwidth in the inset) versus bias

### 5.1.3 Discussion.

Figure 5-2 and Figure 5-6 reveal a qualitative difference in small-signal responses of QDot and QDash lasers. Firstly, the damping of resonance peak of QDot devices is much stronger. The origin of this phenomenon is the stronger gain compression in quantum-dot active material in comparison to quantum-dashes. This gain compression stems from the degeneracy degree of the lasing states in the devices. In quantum-dash gain material DOS function has quantum wire-like nature, resulting in higher degeneracy factor. Consequently, saturated gain (closely related to e.g. band filling effect) is also larger. In turn, larger saturation gain leads to lower gain compression factor. Secondly, we observe that the low frequency roll-off is completely inhibited in QDash lasers. This may result from the absence of the injection bottleneck due to the large and discontinuous energy separation between the carrier reservoir and lasing states in quantum-dash lasers. Another explanation is based on the model developed in [19]: in case of QDash devices DOS function shape equalizes the carrier capture time into specific quantum dash, thus carriers are captured into all energy states of all dashes at averaged time. On the contrary, a significant capture time distribution occurs in quantum dots, and the carriers are captured within a partial range of dots energies, followed by a relaxation into lasing states, thus increasing the nonlinear scattering. On the other hand, this partial capture process leads to scarcer filling of non-lasing dots resulting in larger resonance frequency at lower bias. Indeed, we have experimentally confirmed this theoretical prediction.

QDash lasers show slightly lower  $K$ - and lower  $D$ -factor in comparison to QDot counterparts. Lower  $D$ -factor results in slower increase of resonance frequency versus injected current. Consequently, at low and moderate bias levels, which is preferable in order to avoid heating imposed bandwidth limitations as well as differential gain decrease, QDash lasers demonstrate smaller relaxation resonance frequency and modulation bandwidth. Lower  $K$ -factor for QDash laser implies weaker damping of a resonance peak and may result from lower gain compression as a direct consequence of higher number of populated states. QDash lasers feature shorter carrier recombination time, this is probably related to continuous energy band structure of quantum dash gain material, which shortens carrier transportation time into lasing energy states and inhibits carrier bottleneck. Another discrepancy, which is important for practical applications of nanostructure lasers, is the limitation of modulation bandwidth. The saturated gain in QDash gain material is higher due to larger degeneracy factor of QDash states therefore modulation bandwidth of QDash devices saturates at higher bias levels in comparison to QDot lasers.

Therefore, lasers with quantum dot active material achieve larger values of modulation bandwidth and relaxation frequency at lower bias current than similar lasers based on quantum dash active medium.

## 5.2 Large-signal digital modulation

In the previous section we have presented the dynamics of QDot and QDash lasers under small-signal operation, which implies using of periodical modulation signal with a swing of -10 dBm. We will now investigate the large-signal digital modulation capability of the lasers, where modulation swings amount to 0.3 to 0.4  $V_{p-p}$ . The ability to transmit digital modulation signal is one of the key characteristics of the laser. Non-return-to-zero on/off keying (NRZ OOK) is the most widely known digital modulation format because of its simplicity and cost effectivity for applications with medium data rate demands (e.g. in access and metropolitan area networks). NRZ OOK scheme is realized by direct modulation of the bias current, which translates into the modulation of the laser intensity. In NRZ configuration the optical power stays the same during logical „1“ transmission, i.e. does not reduce to logical „0“ level inside the symbol time slot, the power drops to lower level only when logical „0“ is transmitted. On the contrary, in return-to-zero (RZ) scheme the optical power drops to logical „0“ energy level during every symbol, so that logical „1“ only partially occupies the symbol time-slot. Consequently, RZ scheme provides shorter pulse transmission, being advantageous in preventing intersymbol interference and flexibility in time-division multiplexing, but at the cost of higher demands to the turn-on characteristics of the laser or additional pulse-carving techniques (e.g. MZM (Mach-Zehnder Modulator)). Yet, NRZ is the lowest cost techniques, has narrower spectral density and with forward-error correction algorithm (FEC) is still capable of transmission rate up to 40 Gb/s p.42 [127]. Usually the laser is biased above threshold to avoid undesired turn-on delay mentioned in previous chapters, so the switching between „1“ and „0“ levels translates into the switching between higher and lower optical intensity levels.

The performance of the laser transmission system under large-signal digital modulation is usually evaluated via the eye-diagram and bit-error-rate (BER) measurements. The former is the representation of the received signal's waveform. Superimposing the waveforms in time domain leads to resultants intensity vs time graph, which resembles an eye. An eye-diagram gives information about the quality of the received signal: Q-factor, jitter, eye opening, extinction ratio, noise and intensity under- and overshoots. BER is the ratio of error bits to the total number

of transmitted bits during determined time period. The schematic set-up for back-to-back eye-diagram measurements is shown in Figure 5-9.

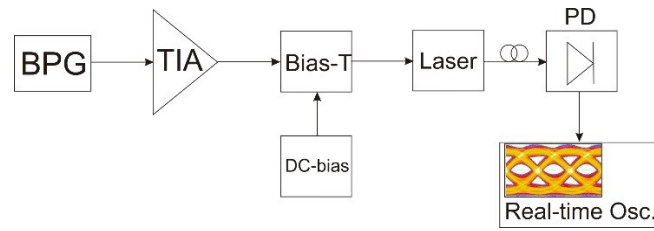


**Figure 5-9 Eye-diagram measurement set-up. BPG – bit-pattern generator, TIA – transimpedance electrical amplifier, PD – photodetector.**

The bit-pattern generator (BPG) produces pseudo-random bit sequence with pre-defined word length of  $2^7-1$  bits. Transimpedance electrical amplifier function is twofold: firstly, it amplifies output BPG-signal, secondly it protects the BPG from any back reflected high-frequency signal, since the laser's modulation input is not 50 Ohm matched. 80 GSa/s real-time oscilloscope and 50 GHz photodetector are used here on the receiver part without any optical amplification.

#### Digital modulation of quantum-dash laser

For large-signal direct modulation experiment, we have employed the same short-cavity QDash F-P laser, which we used in section 5.1.2 for small-signal measurements. QDash laser performance was tested in back-to-back configuration at different currents. In Figure 5-10 current dependent large-signal responses are presented. The eye-diagrams show the bit-rate of 10, 15, 17.5 and 20 Gbit/s. The maximum error-free ( $BER < 10^{-9}$ ) bit-rate was 17.5 Gbit/s as shown in Figure 5-10 (c)) with  $Q=4.9$  for the maximum received optical power. In Figure 5-10 (d)-(f) eye-diagrams are presented, demonstrating a possibility for 20 Gb/s transmission with QDash lasers owing to the eye openings and extinction ratio. We observed the reduction of Q-factor at increased injection current, probably due to the saturation of the optical gain.

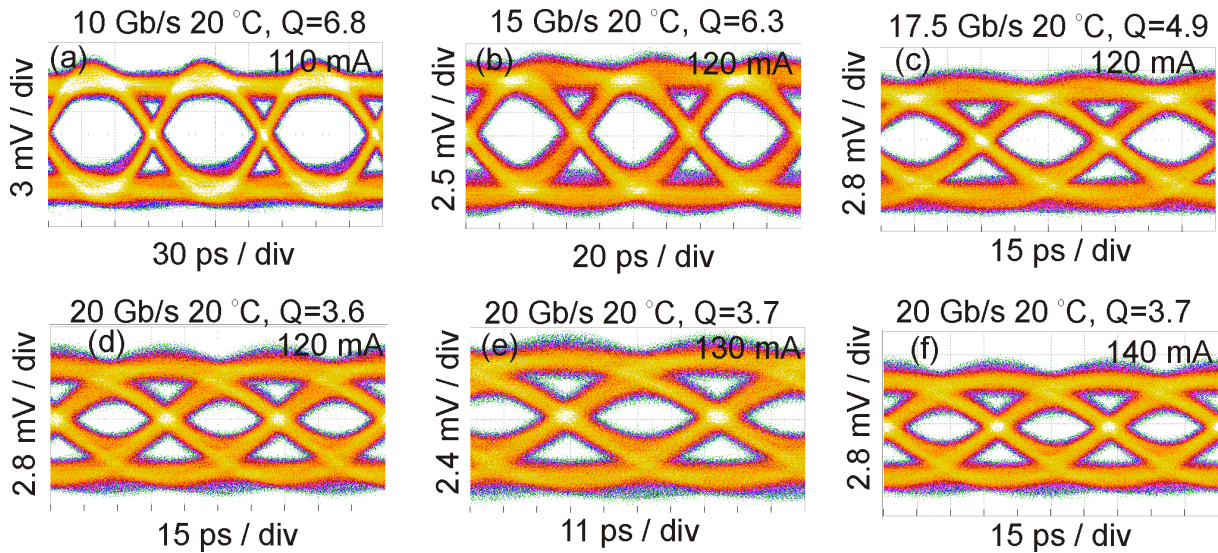


Figure 5-10 Eye-diagrams of QDash laser measured at different bias current

Digital modulation of quantum-dot laser

Eye-diagrams were measured with the same short-cavity QDot laser described in section 5.1.1. Several eye-patterns were collected at different bias currents and bit rates. The highest error-free bit-rate was achieved at 22.5 Gb/s with Q-factor of 3.5 at 110 mA of injection current, the corresponding eye-diagram is shown in Figure 5-11 for maximum received optical power.

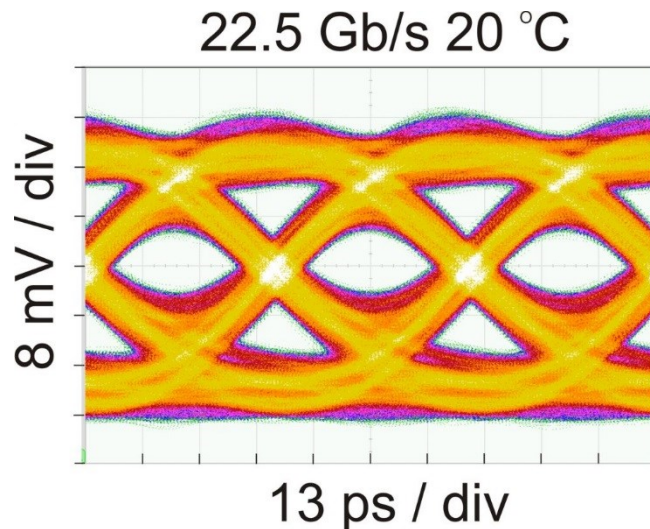


Figure 5-11 Eye-diagram of QDot laser in OOK scheme, back-to-back configuration

BER curves measured with QDot and QDash lasers at 22.5 and 17.5 Gb/s respectively are shown in Figure 5-12, showing BER well below  $10^{-9}$  (QDash) and  $10^{-12}$  (QDot laser).

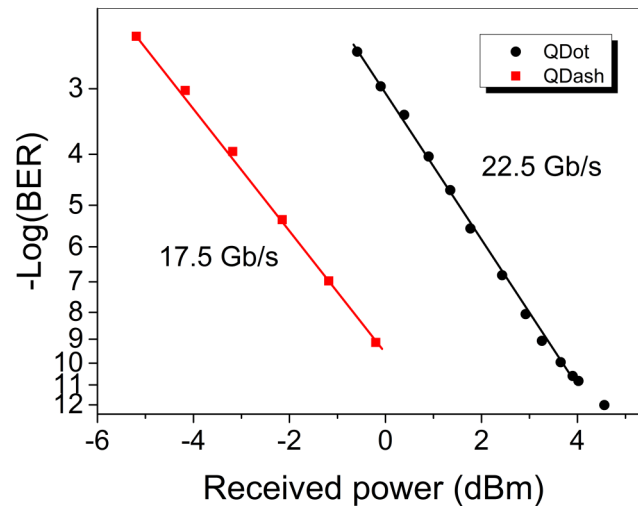


Figure 5-12 Bit-error ratios of QDot and QDash lasers

### 5.3 Conclusion

To summarize the previous sections, we have investigated the performance of the short cavity length quantum-dot and quantum-dash lasers under direct modulation. The measurements of S21 reveal a strong impact of the energy states structure, which is given by the type of active medium on such parameters of a small-signal operation as  $K$ - and  $D$ -factor, carrier lifetime, modulation bandwidth, relaxation resonance frequency and damping.

We show larger  $D$ -factor for QDot lasers, which implies larger resonance frequency at lower bias current. We have observed that in QDot lasers saturation of modulation bandwidth occurs at lower bias level, this feature can be useful in future concepts of energy efficient laser sources. However, we also point out on severe limitations of small-signal operation in QDot lasers related to carrier transport bottleneck, which limits the optical gain and seems to be inhibited in QDash lasers. This carrier transport issue should be addressed to overcome constrains in further system implementation of QDot lasers. Larger gain compression is the reason for overdamped RO peak in QDot lasers, whereas a moderate damping is observed in QDash devices. Further, several approaches to avoid this effect and to achieve a higher modulation rate before its saturation are outlined [17]. Reduced barrier width and the distance between quantum dot/dash layers: wide barriers hinder fast carrier transportation into the gain layers, quickly damping the modulation response. The barrier length reduction allows up to 20% higher modulation bandwidth as predicted in [17]. The distance between quantum dot/dash layers is given by the spacer thickness. The latter is important to ensure the flatness of the layers and to enhance the optical

confinement [17], [128]. Asymmetric positioning of layers would compensate the slower mobility of holes and their short diffusion length, but at the cost of slightly decreased optical confinement. Nonradiative recombination in the active region because of the thermal holes distribution, which reduces the gain. By introducing p-doping modulation the barriers are partly ionized and hence the electrons are rejected by Coulomb interaction and tend to localize in the QDs, which reduces carrier capture in the nonradiative centers [26]. Tunneling injection [21], [129] would suppress so called hot carrier effect – the escape of the carrier into numerous vacant carrier reservoir states and contrarily promote the phonon assisted cold electrons injection directly in the ground states.

It is also important to reduce parasitics and heating effects by means of optimized laser chip and mounting layouts. Finally, we have demonstrated 8.1 GHz modulation bandwidth for InP/InAs QDot lasers, which is the fastest rate achieved for any MOVPE-grown nanostructure lasers and comparable even with direct modulation optimized MBE/CBE quantum-dot and quantum dash counterparts. MOVPE-grown QDash lasers presented in this section show similar -3 dB modulation bandwidth, though achieved at higher injection currents. Employing large-signal modulation in NRZ OOK format we show the maximum bit-rate of 22.5 and 17.5 Gb/s for QDot and QDash laser respectively at  $BER < 10^{-9}$ . Yet, eye-diagrams measured at maximum received power show a potential for QDash laser to achieve 20 Gb/s, BER below  $10^{-12}$  and  $10^{-9}$  is presented for QDot and QDash laser respectively.

## 6. Summary

This thesis has reported on InAs/InP quantum-dot and quantum-dash based lasers emitting in the 1.55  $\mu\text{m}$  telecommunication window. Mode-locking (in single- and two-section lasers), non-linear and dynamical properties of these devices have been explored. Presented MOVPE growth, design and fabrication methods result in promising static and dynamical characteristics of demonstrated lasers.

The mode-locking characteristics of single- and two-section quantum-dot and quantum-dash lasers have been presented and analyzed. The mode-locking in two-section devices is driven by well-known dynamical interaction between absorber and gain sections. For the first time to our knowledge, we demonstrated ps range ex-facet pulse emission from MOVPE-grown InP/InAs QDot PMLL at high repetition frequency of  $\sim 33$  GHz with 300–400 MHz tuning possibility. Yet, the broad RF-linewidth ( $\sim$ MHz) witnessed high pulse jitter. Single-section quantum-dot and dash mode-locked lasers demonstrated nearly 10 times lower RF-linewidth and sub-ps pulse emission. These advantages came at the cost of  $\sim 10$  times lower repetition frequency tuning potential, also fiber based pulse compression was necessary. The mechanism of pulse generation in single-section lasers is not well understood. Thus proper device engineering as a solution to obtain direct ex-facet (i.e. without compression techniques) fs-pulse emission is not yet available, constraining further system implementation of such lasers. FROG-measurements revealed the non-linear pulse-chirp and sub-peaks on the leading edge of the pulse in both quantum-dot and quantum-dash lasers. Summarizing this part, we proposed that quantum-dot and quantum-dash single- and two-section mode-locked lasers demonstrate similar characteristics and subjected to similar drawbacks.

Another unique feature of nanostructure lasers is the strong optical nonlinearity; this makes them very attractive for applications based on four-wave mixing. The intracavity four-wave mixing in quantum-dot and dash based active material have been studied extensively, but so far there had been no comparative study of this phenomenon depending on the type of nanostructure (quantum-dots and dashes). A detailed study of four-wave mixing in quantum-dot and dash lasers under dual-mode external optical injection presented in Chapter 4. We have observed large normalized conversion efficiency of -18.6 dB, OSNR of 37 dB, and a conversion achievable for frequency detunings up to 3 THz in MOVPE-grown 1490  $\mu\text{m}$ -long InP/InAs quantum-dash lasers operating at 1550 nm under dual-mode optical injection. These values are the highest

reported for F-P lasers and comparable to ones reported for DFB-lasers and SOAs, more complex to process. We observe a larger conversion efficiency for 1490  $\mu\text{m}$ -long quantum-dash devices in comparison to 1250  $\mu\text{m}$ -long quantum-dot lasers, fabricated by the same growth and processing techniques. Quantum-dot devices with delta-function DOS (in contrast to quantum dashes whose energetic structure due to the larger volume of the dashes shows a larger density of close lying delta function states) show a four times lower third-order optical susceptibility, a 12 dB-lower normalized conversion efficiency and 14.7 dB-lower optical signal-to-noise ratio. The results allow to decide, which structural approach should be followed for applications in the future.

Finally, we have compared dynamic properties of short-cavity quantum-dot and quantum-dash lasers under small-and large-signal operation. We observed a larger  $D$ -factor for quantum-dot lasers, which implies a larger resonance frequency at lower bias current, and a saturation of the modulation bandwidth at lower bias levels. This feature can be useful in concepts for energy efficient laser sources. Larger gain compression is the reason for the overdamped resonance frequency peak in quantum-dot lasers, whereas moderate damping is observed in quantum-dash devices. We have shown 8.1 GHz modulation and error-free 22.5 Gbit/s large signal modulation for InP/InAs quantum-dot lasers. Quantum-dash show similar small signal modulation bandwidths, though at significantly higher injection currents and a bit rate of 17.5 Gbit/s with potential for 20 Gbit/s. Dissipated heat-to-bit rate ratios are as low as 8 and 11 pJ/bit for quantum-dot and quantum-dash lasers, respectively. It is important to note that parasitics and heating effects can be strongly reduced for the present devices in the future by means of optimized laser chip and mounting leading to further improved dynamic properties of the lasers.

## List of Acronyms

AS	Absorber section
ASE	Amplified spontaneous emission
BER	Bit-error-rate
BPG	Bit-pattern generator
CDP	Carrier density pulsation
CE	Conversion efficiency
CH	Carrier heating
CW	Continuous wave
DC	Direct current
DOS	Density of states
DUT	Device under test
ESA	Electrical spectrum analyzer
FEC	Forward-error correction
FP	Fabry-Perot
FR	Free running
FROG	Frequency-Resolved Optical Gating
FWHM	Full-width at half maximum
FWM	Four-wave mixing
GPON	Gigabit Passive Optical Network
GS	Gain switching

HML	Hybrid mode-locking
IL	Injection-locked
LAN	Local area networks
MBE	Molecular- and chemical beam epitaxy
ML	Mode-locking
MLL	Mode-locked laser
MOVPE	Metal-organic vapor phase epitaxy
MZM	Mach-Zehnder Modulator
NDFWM	Non-degenerate four-wave mixing
NRZ	Non-return-to-zero
OIL	Optical injection locking
OOK	On/off keying
OSNR	Optical signal-to-noise ratio
OTDM	Optical time-division multiplexing
PIC	Photonic integrated circuit
PML	Passive mode-locking
PMLL	Passive mode-locked lasers
QS	Q-switching
QW	Quantum well
RO	Relaxation oscillation
RZ	Return-to-zero

SHB	Spectral hole burning
SK	Stranski-Krastanov
SL	Slave lasers
SNR	Signal-to-noise ratio
SOA	Semiconductor optical amplifiers
SSMLL	Single-section mode-locked laser
TBP	Time-bandwidth product
TPA	Two-photon absorption
WDM	Wavelength-division multiplexing

## Bibliography

- [1] J. Hecht, “Great Leaps of Light,” *IEEE Spectr.*, vol. 53, no. 2, pp. 28–53, 2016.
- [2] Y. Tsunoda, T. Shibasaki, H. Oku, J. Matsui, T. Shiraishi, S. Ide, T. Mori, K. Yoichi, and H. Tamura, “24 to 34-Gb/s  $\times 4$  Multi-Rate VCSEL-Based Optical Transceiver with Referenceless CDR,” in *Optical Fiber Communication Conference*, 2016, p. Th4D.4.
- [3] L. Yu, H. Wang, D. Lu, S. Liang, C. Zhang, B. Pan, L. Zhang, and L. Zhao, “A Widely Tunable Directly Modulated DBR Laser With High Linearity,” *IEEE Photonics J.*, vol. 6, no. 4, 2014.
- [4] Q. Zhao, J. Q. Pan, J. Zhang, B. X. Li, F. Zhou, B. J. Wang, L. F. Wang, L. J. Zhao, G. T. Zhou, and W. Wang, “MQW electroabsorption modulator-integrated DFB laser modules for high-speed transmission,” *Semicond.Sci.Technol.*, vol. 21, pp. 734–739, 2006.
- [5] M. Theurer, Y. Wang, L. Zeng, U. Troppenz, G. Przyrembel, A. Sigmund, M. Moehrle, and M. Schell, “2 x 56 GB/s from a Double Side Electroabsorption Modulated DFB Laser,” in *Optical Fiber Communication Conference*, 2016, p. Tu3D.6.
- [6] D. Bimberg, “Quantum dot based nanophotonics and nanoelectronics,” *Electron. Lett.*, vol. 44, no. 3, pp. 168–171, Jan. 2008.
- [7] F. Lelarge, B. Rousseau, B. Dagens, F. Poingt, F. Pommereau, and A. Accard, “Room temperature continuous-wave operation of buried ridge stripe lasers using InAs-InP (100) quantum dots as active core,” *IEEE Photonics Technol. Lett.*, vol. 17, no. 7, pp. 1369–1371, Jul. 2005.
- [8] S. Anantathanasarn, R. Nötzel, P. Van Veldhoven, T. Eijkemans, and J. Wolter, “Wavelength-tunable (1.55- $\mu\text{m}$  region) InAs quantum dots in InGaAsP/InP (100) grown by metal-organic vapor-phase epitaxy,” *J. Appl. Phys.*, vol. 98, no. 1, 2005.
- [9] Y. Arakawa and H. Sakaki, “Multidimensional quantum well laser and temperature dependence of its threshold current,” *Appl. Phys. Lett.*, vol. 40, no. 11, pp. 939–941, Aug. 1982.

- [10] N. Kirstaedter, N. Ledentsov, M. Grundmann, D. Bimberg, V. Ustinov, S. Ruvimov, M. Maximov, P. Kop'ev, Z. Alferov, U. Richter, P. Werner, U. Gösele, and J. Heydenreich, "Low threshold, large To injection laser emission from (InGa)As quantum dots," *Electron. Lett.*, vol. 30, no. 17, p. 1416, 1994.
- [11] N. Kirstaedter, O. Schmidt, N. Ledentsov, D. Bimberg, V. Ustinov, A. Egorov, A. Zhukov, M. Maximov, P. Kop'ev, and Z. Alferov, "Gain and differential gain of single layer InAs/GaAs quantum dot injection lasers," *Appl. Phys. Lett.*, vol. 69, no. 9, p. 1226, 1996.
- [12] O. Schmidt, N. Kirstaedter, N. Ledentsov, M. Mao, D. Bimberg, V. Ustinov, A. Egorov, A. Zhukov, M. Maximov, P. Kop'ev, and Z. Alferov, "Prevention of gain saturation by multi-layer quantum dot lasers," *Electron. Lett.*, vol. 32, no. 14, p. 1302, 1996.
- [13] D. Bimberg, N. Kirstaedter, N. Ledentsov, Z. Alferov, P. Kop'ev, and V. Ustinov, "InGaAs-GaAs quantum-dot lasers," *IEEE J. Sel. Top. Quantum Electron.*, vol. 3, no. 2, pp. 196–205, 1997.
- [14] S. Fathpour, Z. Mi, P. Bhattacharya, A. R. Kovsh, S. S. Mikhlin, I. L. Krestnikov, A. V. Kozhukhov, and N. N. Ledentsov, "The role of Auger recombination in the temperature-dependent output characteristics ( $T_0 = \infty$ ) of p-doped 1.3  $\mu\text{m}$  quantum dot lasers," *Appl. Phys. Lett.*, vol. 85, no. 22, pp. 5164–5166, 2004.
- [15] R. Schwertberger, D. Gold, J. Reithmaier, and A. Forchel, "Long-wavelength InP-based quantum-dash lasers," *IEEE Photonics Technol. Lett.*, vol. 14, no. 6, pp. 735–737, 2002.
- [16] J. Reithmaier, G. Eisenstein, and A. Forchel, "InAs / InP Quantum-Dash Lasers and Amplifiers," *Proc. IEEE*, vol. 95, no. 9, pp. 1779–1790, 2007.
- [17] D. Gready and G. Eisenstein, "Carrier Dynamics and Modulation Capabilities of 1.55- $\mu\text{m}$  Quantum-Dot Lasers," *IEEE J. Sel. Top. Quantum Electron.*, vol. 19, no. 4, p. 1900307, 2013.
- [18] H. Dery and G. Eisenstein, "The impact of energy band diagram and inhomogeneous broadening on the optical differential gain in nanostructure lasers," *IEEE J. Quantum Electron.*, vol. 41, no. 1, pp. 26–35, 2005.

- [19] H. Dery and G. Eisenstein, “Self-consistent rate equations of self-assembly quantum wire lasers,” *IEEE J. Quantum Electron.*, vol. 40, no. 10, pp. 1398–1409, 2004.
- [20] R. Schwertberger, D. Gold, J. Reithmaier, and A. Forchel, “Epitaxial growth of 1.55  $\mu\text{m}$  emitting InAs quantum dashes on InP-based heterostructures by GS-MBE for long-wavelength laser applications,” *J. Cryst. Growth*, vol. 251, no. 1–4, pp. 248–252, 2003.
- [21] Z. Mi and P. Bhattacharya, “DC and Dynamic Characteristics of P-Doped and Tunnel Injection 1.65- $\mu\text{m}$  InAs Quantum-Dash Lasers Grown on InP (001),” *IEEE J. Quantum Electron.*, vol. 42, no. 12, pp. 1224–1232, 2006.
- [22] O. Mollet, A. Martinez, K. Merghem, S. Joshi, J.-G. Provost, F. Lelarge, and A. Ramdane, “Dynamic characteristics of undoped and p-doped Fabry-Perot InAs/InP quantum dash based ridge waveguide lasers for access/metro networks,” *Appl. Phys. Lett.*, vol. 105, no. 14, p. 141113, Oct. 2014.
- [23] M. Heck, E. Bente, B. Smalbrugge, Y. Oei, M. Smit, S. Anantathanasarn, and R. Nötzel, “Observation of Q-switching and mode-locking in two-section InAs/InP (100) quantum dot lasers around 1.55  $\mu\text{m}$ ,” *Opt. Express*, vol. 15, no. 25, pp. 16292–16301, 2007.
- [24] D. Franke, M. Moehrl, J. Boettcher, P. Harde, A. Sigmund, and H. Kuenzel, “Effect of metal organic vapor phase epitaxy growth conditions on emission wavelength stability of 1.55  $\mu\text{m}$  quantum dot lasers,” *Appl. Phys. Lett.*, vol. 91, no. 8, pp. 81117–1, 2007.
- [25] E. S. Semenova, I. V. Kulkova, S. Kadkhodazadeh, M. Schubert, and K. Yvind, “Metal organic vapor-phase epitaxy of InAs/InGaAsP quantum dots for laser applications at 1.5  $\mu\text{m}$ ,” *Appl. Phys. Lett.*, vol. 99, no. 10, p. 101106, Sep. 2011.
- [26] D. Arsenijević and D. Bimberg, “Quantum-dot lasers for 35 Gbit/s pulse-amplitude modulation and 160 Gbit/s differential quadrature phase-shift keying,” *Semicond. Lasers Laser Dyn. VII*, vol. 9892, pp. 1–10, 2016.
- [27] S. Banyoudeh, A. Abdollahinia, O. Eyal, F. Schnabel, V. Sichkovskyi, G. Eisenstein, and J. Reithmaier, “High-speed directly modulated 1.5- $\mu\text{m}$  quantum dot lasers,” *Proc. SPIE*, vol. 9767, p. 97670L, 2016.

- [28] M. Dontabactouny, R. Piron, K. Klaime, N. Chevalier, K. Tavernier, S. Loualiche, a. Le Corre, D. Larsson, C. Rosenberg, E. Semenova, and K. Yvind, “41 GHz and 10.6 GHz low threshold and low noise InAs/InP quantum dash two-section mode-locked lasers in L band,” *J. Appl. Phys.*, vol. 111, 2012.
- [29] Z. Lu, J. Liu, S. Raymond, P. Poole, P. Barrios, and D. Poitras, “312-fs pulse generation from a passive C-band InAs/InP quantum dot mode-locked laser,” *Opt. Express*, vol. 16, no. 14, pp. 10835–10840, 2008.
- [30] S. Heck, S. Healy, S. Osborne, E. O’Reilly, F. Lelarge, F. Poingt, A. Accard, F. Pommereau, O. Le Gouezigou, and B. Dagens, “An analysis of 1.55  $\mu\text{m}$  InAs/InP quantum dash lasers,” *Appl. Phys. Lett.*, vol. 92, no. 25, p. 251105, 2008.
- [31] M. Heck, A. Renault, E. A. Bente, Y.-S. Oei, M. K. Smit, K. S. E. Eikema, W. Ubachs, S. Anantathanasarn, and R. Notzel, “Passively Mode-Locked 4.6 and 10.5 GHz Quantum Dot Laser Diodes Around 1.55- $\mu\text{m}$  With Large Operating Regime,” *IEEE J. Sel. Top. Quantum Electron.*, vol. 15, no. 3, pp. 634–643, 2009.
- [32] F. Genz, A. Lenz, H. Eisele, L. Ivanova, R. Timm, U. W. Pohl, M. Dähne, D. Franke, and H. Künzel, “InAs nanostructures on InGaAsP/InP(001): Interaction of InAs quantum-dash formation with InGaAsP decomposition,” *J. Vac. Sci. Technol. B*, vol. 28, no. 4, p. C5E1-C5E7, Jul. 2010.
- [33] D. Franke, J. Kreissl, W. Rehbein, F. Wenning, H. Kuenzel, U. Pohl, and D. Bimberg, “Effect of the Shape of InAs Nanostructures on the Characteristics of InP-Based Buried Heterostructure Semiconductor Optical Amplifiers,” *Appl. Phys. Express*, vol. 4, no. 1, p. 14101, Jan. 2011.
- [34] F. Wenning, “Diploma thesis,” Fraunhofer-Institut für Nachrichtentechnik, Heinrich-Hertz-Institut, 2010.
- [35] O. Qasaimeh, W.-D. Zhou, J. Phillips, S. Krishna, P. Bhattacharya, and M. Dutta, “Bistability and self-pulsation in quantum-dot lasers with intracavity quantum-dot saturable absorbers,” *Appl. Phys. Lett.*, vol. 74, no. 12, pp. 1654–1656, 1999.
- [36] M. Tahvili, L. Du, M. Heck, R. Nötzel, M. Smit, and E. Bente, “Dual-wavelength passive

- and hybrid mode-locking of 3, 4.5 and 10 GHz InAs/InP(100) quantum dot lasers,” *Opt. Express*, vol. 20, no. 7, pp. 8117–8135, Mar. 2012.
- [37] J. Liu, Z. Lu, S. Raymond, P. Poole, P. Barrios, and D. Poitras, “Dual-wavelength 92.5 GHz self-mode-locked InP-based quantum dot laser,” *Opt. Lett.*, vol. 33, no. 15, pp. 1702–1704, 2008.
- [38] Z. Lu, J. Liu, P. Poole, S. Raymond, P. Barrios, D. Poitras, G. Pakulski, P. Grant, and D. Roy-Guay, “An L-band monolithic InAs/InP quantum dot mode-locked laser with femtosecond pulses,” *Opt. Express*, vol. 17, no. 16, pp. 13609–13614, 2009.
- [39] K. Merghem, A. Akrouf, A. Martinez, G. Aubin, A. Ramdane, F. Lelarge, and G.-H. Duan, “Pulse generation at 346 GHz using a passively mode locked quantum-dash-based laser at 1.55  $\mu\text{m}$ ,” *Appl. Phys. Lett.*, vol. 94, no. 2, p. 21107, Jan. 2009.
- [40] Y. K. Chen, M. C. Wu, T. Tanbun-Ek, R. A. Logan, and M. A. Chin, “Subpicosecond monolithic colliding-pulse mode-locked multiple quantum well lasers,” *Appl. Phys. Lett.*, vol. 58, no. 12, pp. 1253–1255, 1991.
- [41] L. Chusseau, P. Martin, C. Brasseur, C. Alibert, P. Hervé, P. Arguel, F. Lozes-Dupuy, and E. Rao, “Carrier-induced change due to doping in refractive index of InP: Measurements at 1.3 and 1.5  $\mu\text{m}$ ,” *Appl. Phys. Lett.*, vol. 69, no. 20, p. 3054, 1996.
- [42] R. Rosales, “InAs/InP quantum dash mode locked lasers for optical communications,” Ph.D. dissertation, Télécom Sudparis, Paris, France, 2012.
- [43] F. Kefelian, S. O’Donoghue, M. T. Todaro, J. G. McInerney, and G. Huyet, “RF Linewidth in Monolithic Passively Mode-Locked Semiconductor Laser,” *IEEE Photonics Technol. Lett.*, vol. 20, no. 16, pp. 1405–1407, 2008.
- [44] E. Sooudi, C. de Dios, J. G. McInerney, H. Huyet, F. Lelarge, K. Merghem, R. Rosales, A. Martinez, A. Ramdane, and S. Hegarty, “A Novel Scheme for Two-Level Stabilization of Semiconductor Mode-Locked Lasers Using Simultaneous Optical Injection and Optical Feedback,” *IEEE J. Sel. Top. Quantum Electron.*, vol. 19, no. 4, pp. 1101208–1101208, Jul. 2013.

- [45] T. Habruseva, D. Arsenijević, M. Kleinert, D. Bimberg, G. Huyet, and S. P. Hegarty, “Optimum phase noise reduction and repetition rate tuning in quantum-dot mode-locked lasers,” *Appl. Phys. Lett.*, vol. 104, no. 2, pp. 10–13, 2014.
- [46] D. Bimberg, D. Arsenijević, and M. Kleinert, “Jitter reduction by optical feedback of passively mode-locked quantum-dot lasers,” *2013 IEEE Photonics Conf. IPC 2013*, vol. 2, pp. 234–235, 2013.
- [47] K. Sato, “100 GHz optical pulse generation using Fabry-Perot laser under continuous wave operation,” *Electron. Lett.*, vol. 37, no. 12, pp. 763–764, 2001.
- [48] T. Piwonski, J. Pulka, G. Madden, G. Huyet, J. Houlihan, E. Viktorov, T. Erneux, and P. Mandel, “Intradot dynamics of InAs quantum dot based electroabsorbers,” *Appl. Phys. Lett.*, vol. 94, no. 12, p. , 2009.
- [49] L. Hou, M. Haji, J. Akbar, B. Qiu, and A. Bryce, “Low divergence angle and low jitter 40 GHz AlGaInAs/InP 1.55 $\mu$ m mode-locked lasers,” *Opt. Lett.*, vol. 36, no. 6, pp. 966–968, Jul. 2011.
- [50] D. R. Matthews, H. D. Summers, P. M. Snowton, and M. Hopkinson, “Experimental investigation of the effect of wetting-layer states on the gain–current characteristic of quantum-dot lasers,” *Appl. Phys. Lett.*, vol. 81, no. 26, p. 4904, 2002.
- [51] X. Huang, A. Stintz, H. Li, A. Rice, G. Liu, L. Lester, J. Cheng, and K. Malloy, “Bistable operation of a two-section 1.3- $\mu$ m InAs quantum dot laser - absorption saturation and the quantum confined Stark effect,” *IEEE J. Quantum Electron.*, vol. 37, no. 3, pp. 414–417, 2001.
- [52] F. Klopf, S. Deubert, J. Reithmaier, and A. Forchel, “Correlation between the gain profile and the temperature-induced shift in wavelength of quantum-dot lasers,” *Appl. Phys. Lett.*, vol. 81, no. 2, pp. 217–219, 2002.
- [53] S. Bhowmick, Z. Baten, T. Frost, B. Ooi, and P. Bhattacharya, “High Performance InAs/InGaAlAs/InP Quantum Dot 1.55  $\mu$ m Tunnel Injection Laser,” *IEEE J. Quantum Electron.*, vol. 50, no. 1, pp. 7–14, 2014.

- [54] V. Sichkovskiy, M. Waniczek, and J. Reithmaier, “High-gain wavelength-stabilized 1.55  $\mu\text{m}$  InAs/InP(100) based lasers with reduced number of quantum dot active layers,” *Appl. Phys. Lett.*, vol. 102, no. 22, pp. 1–5, 2013.
- [55] E. Viktorov, T. Erneux, P. Mandel, T. Piwonski, G. Madden, J. Pulka, G. Huyet, and J. Houlihan, “Recovery time scales in a reversed-biased quantum dot absorber,” *Appl. Phys. Lett.*, vol. 94, no. 26, p. 263502, Jun. 2009.
- [56] D. B. Malins, A. Gomez-Iglesias, S. J. White, W. Sibbett, A. Miller, and E. U. Rafailov, “Ultrafast electroabsorption dynamics in an InAs quantum dot saturable absorber at 1.3  $\mu\text{m}$ ,” *Appl. Phys. Lett.*, vol. 89, no. 17, p. 171111, Oct. 2006.
- [57] E. Sooudi, S. Sygletos, A. D. Ellis, G. Huyet, J. G. McInerney, F. Lelarge, K. Merghem, R. Rosales, A. Martinez, A. Ramdane, and S. P. Hegarty, “Optical Frequency Comb Generation Using Dual-Mode Injection-Locking of Quantum-Dash Mode-Locked Lasers: Properties and Applications,” *IEEE J. Quantum Electron.*, vol. 48, no. 10, pp. 1327–1338, 2012.
- [58] R. Rosales, K. Merghem, A. Martinez, A. Akrou, J.-P. Turrenc, A. Accard, F. Lelarge, and A. Ramdane, “InAs/InP Quantum-Dot Passively Mode-Locked Lasers for 1.55- $\mu\text{m}$  Applications,” *IEEE J. Sel. Top. Quantum Electron.*, vol. 17, no. 5, pp. 1292–1301, Sep. 2011.
- [59] M. Thompson, K. Tan, C. Marinelli, K. Williams, R. Penty, I. . White, M. Kuntz, D. Ouyang, D. Bimberg, V. Ustinov, A. Zhukov, A. Kovsh, N. Ledentsov, D. Kang, and M. Blamire, “Transform-limited optical pulses from 18 GHz monolithic modelocked quantum dot lasers operating at  $\sim 1.3 \mu\text{m}$ ,” *Electron. Lett.*, vol. 40, no. 5, pp. 346–347, Mar. 2004.
- [60] R. Kaiser, B. Huettl, W. Rehbein, H. Stolpe, H. Heidrich, S. Fidona, and R. Stenzel, “Repetition rate and wavelength tuning of monolithic 40 GHz mode-locked lasers based on InP,” pp. 255–258, 2003.
- [61] G. Fiol, D. Arsenijević, D. Bimberg, A. G. Vladimirov, M. Wolfrum, E. A. Viktorov, and P. Mandel, “Hybrid mode-locking in a 40 GHz monolithic quantum dot laser,” *Appl. Phys. Lett.*, vol. 96, no. 1, pp. 94–97, 2010.

- [62] A. H. Nayfeh and D. T. Mook, *Nonlinear Oscillations*. New York: Wiley-Interscience, 1979.
- [63] K. Sato, “Optical pulse generation using Fabry-Perot lasers under continuous-wave operation,” *IEEE J. Sel. Top. Quantum Electron.*, vol. 9, no. 5, pp. 1288–1293, Sep. 2003.
- [64] L. F. Tiemeijer, P. I. Kuindersma, P. J. A. Thijs, and G. L. J. Rikken, “Passive FM Locking in InGaAsP Semiconductor Lasers,” *IEEE J. Quantum Electron.*, vol. 25, no. 6, pp. 1385–1392, 1989.
- [65] K. Klaime, C. Calò, R. Piron, C. Paranthoen, D. Thiam, T. Batte, O. Dehaese, J. Le Pouliquen, S. Loualiche, A. Le Corre, K. Merghem, A. Martinez, and A. Ramdane, “23 and 39 GHz low phase noise monosection InAs/InP (113)B quantum dots mode-locked lasers,” *Opt. Express*, vol. 21, no. 23, pp. 29000–29005, 2013.
- [66] Y. Wang, Y. Mao, Y. Chen, X. Wang, and H. Su, “Random population model for self pulsation in single-section quantum-dot lasers,” *IEEE Photonics Technol. Lett.*, vol. 25, no. 4, pp. 389–392, 2013.
- [67] W. Yang and S. Member, “Picosecond dynamics of semiconductor Fabry–Perot lasers: a simplified model,” *Sel. Top. Quantum Electron. IEEE J.*, vol. 13, no. 5, pp. 1235–1241, 2007.
- [68] K. Kikuchi, M. Kakui, C. Zah, and T. Lee, “Observation of highly nondegenerate four-wave mixing in 1.5  $\mu\text{m}$  traveling-wave semiconductor optical amplifiers and estimation of nonlinear gain coefficient,” *IEEE J. Quantum Electron.*, vol. 28, no. 1, pp. 151–156, 1992.
- [69] C. Calò, “Quantum dot based mode locked lasers for optical frequency combs,” Ph.D. dissertation, Télécom Sudparis, Paris, France, 2015.
- [70] T. Sadeev, D. Arsenijević, D. Franke, J. Kreissl, H. Künzel, and D. Bimberg, “1.55- $\mu\text{m}$  mode-locked quantum-dot lasers with 300 MHz frequency tuning range,” *Appl. Phys. Lett.*, vol. 106, p. 31114, Jan. 2015.
- [71] R. Rosales, S. Murdoch, R. Watts, K. Merghem, A. Martinez, F. Lelarge, A. Accard, L. Barry, and A. Ramdane, “High performance mode locking characteristics of single section

- quantum dash lasers,” *Opt. Express*, vol. 20, no. 8, pp. 8649–8657, 2012.
- [72] M. Osinski and J. Buus, “Linewidth broadening factor in semiconductor lasers—An overview,” *IEEE J. Quantum Electron.*, vol. 23, no. 1, pp. 9–29, 1987.
- [73] S. Schneider, P. Borri, W. Langbein, U. Woggon, R. L. Sellin, D. Ouyang, and D. Bimberg, “Linewidth enhancement factor in InGaAs quantum-dot amplifiers,” *IEEE J. Quantum Electron.*, vol. 40, no. 10, pp. 1423–1429, 2004.
- [74] H. Schmeckeber, G. Fiol, C. Meuer, D. Arsenijević, and D. Bimberg, “Complete pulse characterization of quantum dot mode-locked lasers suitable for optical communication up to 160 Gbit/s,” *Opt. Express*, vol. 18, no. 4, pp. 3415–3425, 2010.
- [75] C. Calò, H. Schmeckeber, K. Merghem, R. Rosales, F. Lelarge, A. Martinez, D. Bimberg, and A. Ramdane, “Frequency resolved optical gating characterization of sub-ps pulses from single-section InAs/InP quantum dash based mode-locked lasers,” *Opt. Express*, vol. 22, no. 2, pp. 1742–1748, Oct. 2014.
- [76] B. Lanz, B. Ryvkin, E. Avrutin, and J. Kostamovaara, “Performance improvement by a saturable absorber in gain-switched asymmetric-waveguide laser diodes,” *Opt. Express*, vol. 21, no. 24, p. 29780, 2013.
- [77] S. Vainshtein and J. Kostamovaara, “Spectral filtering for time isolation of intensive picosecond optical pulses from a Q-switched laser diode,” *J. Appl. Phys.*, vol. 84, no. 4, p. 1843, 1998.
- [78] K. Petermann, *Laser Diode Modulation and Noise*. Dordrecht: Springer Netherlands, 1988.
- [79] K. Lüdge and E. Schöll, “Quantum-dot lasers Desynchronized nonlinear dynamics of electrons and holes,” *IEEE J. Quantum Electron.*, vol. 45, no. 11, pp. 1396–1403, 2009.
- [80] K. Lüdge, R. Aust, G. Fiol, M. Stubenrauch, and D. Arsenijević, “Large-Signal Response of Semiconductor Quantum-Dot Lasers,” vol. 46, no. 12, pp. 1755–1762, 2010.
- [81] K. Lüdge, M. Bormann, E. Malić, P. Hövel, M. Kuntz, D. Bimberg, A. Knorr, and E. Schöll, “Turn-on dynamics and modulation response in semiconductor quantum dot

- lasers,” *Phys. Rev. B*, vol. 78, no. 3, pp. 1–11, 2008.
- [82] R. A. Fisher, *Optical Phase Conjugation*. Academic Press, 1983.
- [83] *The Handbook of Photonics, Second Edition*. CRC Press, 2006.
- [84] T. Chattopadhyay, “Submillimeter Wave Generation Through Optical four-wave mixing using injection-locked semiconductor lasers,” *Lightwave*, vol. 20, no. 3, pp. 502–506, 2002.
- [85] D. Geraghty, R. Lee, M. Verdiell, M. Ziari, A. Mathur, and K. Vahala, “Wavelength conversion for WDM communication systems using four-wave mixing in semiconductor optical amplifiers,” *IEEE J. Sel. Top. Quantum Electron.*, vol. 3, no. 5, pp. 1146–1155, 1997.
- [86] R. Kibria and M. Austin, “All Optical Signal-Processing Techniques Utilizing Four Wave Mixing,” *Photonics*, vol. 2, pp. 200–213, 2015.
- [87] D. Deppe and D. Huffaker, “Quantum dimensionality, entropy, and the modulation response of quantum dot lasers,” *Appl. Phys. Lett.*, vol. 77, no. 21, pp. 3325–3327, 2000.
- [88] G. Agrawal, “Population pulsations and nondegenerate four-wave mixing in semiconductor lasers and amplifiers,” *J. Opt. Soc. Am. B*, vol. 5, no. 1, p. 147, 1988.
- [89] G. Agrawal, “Four-wave mixing and phase conjugation in semiconductor laser media,” *Opt. Lett.*, vol. 12, no. 4, pp. 260–262, 1987.
- [90] R. Nietzke, P. Panknin, W. Elsaesser, and E. O. Goebel, “Four-wave mixing in GaAs/AlGaAs semiconductor lasers,” *IEEE J. Quantum Electron.*, vol. 25, no. 6, pp. 1399–1406, 1989.
- [91] J. W. D. J. Zhou N. Park and K. J. Vahala, “Terahertz four-wave mixing spectroscopy for study of ultrafast dynamics in a semiconductor optical amplifier,” *Appl. Phys. Lett.*, vol. 63, no. August, pp. 1179–1181, 1993.
- [92] T. Akiyama, H. Kuwatsuka, N. Hatori, Y. Nakata, H. Ebe, and M. Sugawara, “Symmetric highly efficient ( $\sim 0$  dB) wavelength conversion based on four-wave mixing in quantum

- dot optical amplifiers,” *IEEE Photonics Technol. Lett.*, vol. 14, no. 8, pp. 1139–1141, 2002.
- [93] A. Mecozzi, “Analytical theory of four-wave mixing in semiconductor amplifiers,” *Opt. Lett.*, vol. 19, no. 12, pp. 892–894, 1994.
- [94] A. D’Ottavi, F. Girardin, L. Graziani, F. Martelli, P. Spano, A. Mecozzi, S. Scotti, R. Dall’Ara, J. Eckner, and G. Guekos, “Four-wave mixing in semiconductor optical amplifiers: a practical tool for wavelength conversion,” *IEEE J. Sel. Top. Quantum Electron.*, vol. 3, no. 2, pp. 522–528, 1997.
- [95] J. T. Hsieh, P. M. Gong, S. L. Lee, and J. Wu, “Improved dynamic characteristics on four-wave mixing wavelength conversion in light-holding SOAs,” *IEEE J. Sel. Top. Quantum Electron.*, vol. 10, no. 5, pp. 1187–1196, 2004.
- [96] H. Su and L. Lester, “Dynamic properties of quantum dot distributed feedback lasers: high speed, linewidth and chirp,” *J. Phys. D. Appl. Phys.*, vol. 38, pp. 2112–2118, 2005.
- [97] J. Liu and T. Simpson, “Four-wave mixing and optical modulation in a semiconductor laser,” *IEEE J. Quantum Electron.*, vol. 30, no. 4, pp. 957–965, 1994.
- [98] S. Jiang and M. Dagenais, “Nearly degenerate four-wave mixing in Fabry-Perot semiconductor lasers,” *Opt. Lett.*, vol. 18, no. 16, p. 1337, 1993.
- [99] C. Wang, F. Grillot, V. Kovanis, and J. Even, “Rate equation analysis of injection-locked quantum cascade lasers,” *J. Appl. Phys.*, vol. 113, no. 6, p. 63104, 2013.
- [100] B. Lingnau, K. Lüdge, W. Chow, and E. Schöll, “Failure of the  $\alpha$  factor in describing dynamical instabilities and chaos in quantum-dot lasers,” *Phys. Rev. E*, vol. 86, no. 6, Dec. 2012.
- [101] B. Lingnau, *Nonlinear and Nonequilibrium Dynamics of Quantum-Dot Optoelectronic Devices*. Springer International Publishing, 2015.
- [102] Y. Yamamoto and T. Kimura, “Coherent optical fiber transmission systems,” *IEEE J. Quantum Electron.*, vol. 17, no. 6, pp. 919–935, 1981.

- [103] N. Hoghooghi, I. Ozdur, S. Bhooplapur, and P. J. Delfyett, "Direct demodulation and channel filtering of phase-modulated signals using an injection-locked VCSEL," *IEEE Photonics Technol. Lett.*, vol. 22, no. 20, pp. 1509–1511, 2010.
- [104] Z. Lu, J. Liu, S. Raymond, P. Poole, P. Barrios, D. Poitras, F. Sun, G. Pakulski, P. Bock, and T. Hall, "Highly efficient non-degenerate four-wave mixing process in InAs/InGaAsP quantum dots," *Electron. Lett.*, vol. 42, no. 19, pp. 1112–1114, 2006.
- [105] H. Huang, K. Schires, P. Poole, and F. Grillot, "Non-degenerate four-wave mixing in an optically injection-locked InAs/InP quantum dot Fabry–Perot laser," *Appl. Phys. Lett.*, vol. 106, no. 14, p. 143501, 2015.
- [106] C. Wang, F. Grillot, F.-Y. Lin, I. Aldaya, T. Batte, C. Gosset, E. Decerle, and J. Even, "Nondegenerate Four-Wave Mixing in a Dual-Mode Injection-Locked InAs/InP(100) Nanostructure Laser," *IEEE Photonics J.*, vol. 6, no. 1, pp. 1–8, 2014.
- [107] A. Bilenca, R. Alizon, V. Mikhelashvili, D. Dahan, G. Eisenstein, R. Schwertberger, D. Gold, J. Reithmaier, and A. Forchel, "Broad-band wavelength conversion based on cross-gain modulation and four-wave mixing in InAs-InP quantum-dash semiconductor optical amplifiers operating at 1550 nm," *IEEE Photonics Technol. Lett.*, vol. 15, no. 4, pp. 563–565, Apr. 2003.
- [108] O. Karni, A. Capua, G. Eisenstein, D. Franke, J. Kreissl, H. Kuenzel, D. Arsenijević, H. Schmeckeber, M. Stubenrauch, M. Kleinert, D. Bimberg, C. Gilfert, and J. Reithmaier, "Nonlinear pulse propagation in a quantum dot laser," *Opt. Express*, vol. 21, no. 5, pp. 5715–36, 2013.
- [109] A. Capua, G. Eisenstein, and J. Reithmaier, "A nearly instantaneous gain response in quantum dash based optical amplifiers," *Appl. Phys. Lett.*, vol. 97, no. 13, p. 131108, Sep. 2010.
- [110] H. Dery, E. Benisty, A. Epstein, R. Alizon, V. Mikhelashvili, G. Eisenstein, R. Schwertberger, D. Gold, J. Reithmaier, and A. Forchel, "On the nature of quantum dash structures," *J. Appl. Phys.*, vol. 95, no. 11, pp. 6103–6111, Jun. 2004.
- [111] H. Su, H. Li, L. Zhang, Z. Zou, A. L. Gray, R. Wang, P. M. Varangis, and L. Lester,

- “Nondegenerate four-wave mixing in quantum dot distributed feedback lasers,” *IEEE Photonics Technol. Lett.*, vol. 17, no. 8, pp. 1686–1688, Aug. 2005.
- [112] H. Huang, K. Schires, R. Raghunathan, D. Erasme, D. Arsenijević, T. Sadeev, and D. Bimberg, “Highly Efficient Wavelength Conversion in InAs / GaAs Quantum Dot Lasers,” *2015 IEEE Photonics Conf.*, vol. 2, pp. 543–544, 2015.
- [113] “Cisco Visual Networking Index : Global Mobile Data Traffic Forecast Update , 2010 – 2015,” *Growth Lakel.*, vol. 2011, no. 4, pp. 2010–2015, 2011.
- [114] C. Gilfert, V. Ivanov, N. Oehl, M. Yacob, and J. Reithmaier, “High gain 1.55  $\mu\text{m}$  diode lasers based on InAs quantum dot like active regions,” *Appl. Phys. Lett.*, vol. 98, no. 20, p. 201102, 2011.
- [115] S. M. Kim, Y. Wang, M. Keever, and J. S. Harris, “High-frequency modulation characteristics of 1.3 $\mu\text{m}$  InGaAs quantum dot lasers,” *IEEE Photonics Technol. Lett.*, vol. 16, no. 2, pp. 377–379, 2004.
- [116] D. Arsenijević, A. Schliwa, H. Schmeckeber, M. Stubenrauch, M. Spiegelberg, D. Bimberg, V. Mikhelashvili, and G. Eisenstein, “Comparison of dynamic properties of ground- and excited-state emission in p-doped InAs/GaAs quantum-dot lasers,” *Appl. Phys. Lett.*, vol. 104, no. 18, Oct. 2014.
- [117] P. Bhattacharya, “In(Ga)As/GaAs self-organized quantum dot lasers: DC and small-signal modulation properties,” *IEEE Trans. Electron Devices*, vol. 46, no. 5, pp. 871–883, 1999.
- [118] M. Sugawara, K. Mukai, Y. Nakata, H. Ishikawa, and A. Sakamoto, “Effect of homogeneous broadening of optical gain on lasing spectra in self-assembled In<sub>x</sub>Ga(1-x)As/GaAs quantum dot lasers,” *Phys. Rev. B*, vol. 61, no. 11, pp. 7595–7603, 2000.
- [119] L. Coldren and Scott Corzine, *Diode Lasers and Photonic Integrated Circuits*. Wiley, 2012.
- [120] A. Fiore and A. Markus, “Differential Gain and Gain Compression in Quantum-Dot Lasers,” *IEEE J. Quantum Electron.*, vol. 43, no. 4, pp. 287–294, 2007.
- [121] D. Deppe, S. Freisem, H. Huang, and S. Lipson, “Electron transport due to

inhomogeneous broadening and its potential impact on modulation speed in p-doped quantum dot lasers,” *J. Phys. D. Appl. Phys.*, vol. 38, no. 13, pp. 2119–2125, 2005.

- [122] K. Uomi, T. Tsuchiya, M. Aoki, and N. Chinone, “Oscillation wavelength and laser structure dependence of nonlinear damping effect in semiconductor lasers,” *Appl. Phys. Lett.*, vol. 58, no. 7, pp. 675–677, Feb. 1991.
- [123] D. Gready, G. Eisenstein, C. Gilfert, V. Ivanov, and J. Reithmaier, “High-Speed Low-Noise InAs/InAlGaAs/InP 1.55- $\mu\text{m}$  Quantum-Dot Lasers,” *IEEE Photonics Technol. Lett.*, vol. 24, no. 10, pp. 809–811, 2012.
- [124] D. Gready, G. Eisenstein, V. Ivanov, C. Gilfert, F. Schnabel, A. Rippien, J. Reithmaier, and C. Bornholdt, “High Speed 1.55  $\mu\text{m}$  InAs/InGaAlAs/InP Quantum Dot Lasers,” *IEEE Photonics Technol. Lett.*, vol. 26, no. 1, pp. 11–13, 2014.
- [125] P. A. Morton, T. Tanbun-Ek, R. A. Logan, A. M. Sergent, P. F. Sciortino, and D. L. Coblenz, “Frequency response subtraction for simple measurement of intrinsic laser dynamic properties,” *IEEE Photonics Technol. Lett.*, vol. 4, no. 2, pp. 133–136, 1992.
- [126] R. Nagarajan, M. Ishikawa, T. Fukushima, R. Geels, and J. Bowers, “High speed quantum-well lasers and carrier transport effects,” *IEEE J. Quantum Electron.*, vol. 28, no. 10, pp. 1990–2008, 1992.
- [127] I. P. Kaminow, T. Li, and A. E. Willner, *Optical Fiber Telecommunications V B Systems and Networks*. Boston: Academic Press, 2008.
- [128] D. Franke, M. Moehrle, A. Sigmund, H. Kuenzel, U. Pohl, and D. Bimberg, “Improved threshold of buried heterostructure InAs/GaInAsP quantum dot lasers,” *J. Appl. Phys.*, vol. 109, no. 8, pp. 53–57, 2011.
- [129] S. Fathpour, Z. Mi, and P. Bhattacharya, “High-speed quantum dot lasers,” *J. Phys. D. Appl. Phys.*, vol. 38, no. 13, pp. 2103–2111, 2005.

## Acknowledgement

First, I would like to thank Prof. Dr. Dieter Bimberg for his support and opportunity to be a part of his group. I also thank all the members of AG Bimberg for their enormous support, guidance and friendly working atmosphere. Working with Dr. H. Schmeckeber, D. Arsenijević, M. Stubenrauch, Dr. R. Rosales, and J. Miah has been a great pleasure and I am particularly thankful to Holger and Dejan for all trainings and support they provided. I am very grateful to Prof. Dr. A. Ramdane from LPN CNRS for hosting me in his group; I gained a lot from Dr. C. Calo and K. Merghem during my stay. I would like to thank Dr. F. Grillot from Telecom Paris Tech and his group members H. Huang and Dr. K. Schires for fruitful collaboration and friendly working environment. I am thankful to Prof. G. Eisenstein from Technion for countless discussions and helpful suggestions. I express my gratitude to Dr. D. Franke, Dr. J. Kreissl from Heinrich-Hertz Institute for providing the laser devices used within this thesis.

I would like to acknowledge the EU 7-th Framework Program and PROPHET project, Collaborative Research Centre 787 (SFB 787) of Deutsche Forschungsgemeinschaft and the School of Nanophotonics (SoN) for funding my research and training activities.

I thank Mrs. R. Koskinas, Mrs. H. Farell from AG Bimberg secretary for their assistance, which allowed me to stay focused on the research.

I am deeply thankful to my family for unconditional support and encouragement.